Dissertation

Modelling and Simulation of Plastic Deformation in Aluminium Alloys

carried out for the purpose of obtaining the degree of Doctor technicae (Dr. techn.), submitted at TU Wien, Faculty of Mechanical and Industrial Engineering, by

Dipl.-Ing. Bernhard Viernstein

Mat.Nr.: 1125308

under the supervision of

Univ.Prof. Dipl.-Ing. Dr. Ernst Kozeschnik
Institute of Material Science and Technology

reviewed by

Prof. Matthias Schmidtchen
TU Bergakademie Freiberg

Prof. Stefan Pogatscher
Montanuniversität Leoben

Declaration

I declare in lieu of oath, that I wrote this thesis and performed the associated research myself, using only literature cited in this volume. If text passages from sources are used literally, they are marked as such.
I confirm that this work is original and has not been submitted elsewhere for any examination, nor is it currently under consideration for a thesis elsewhere.

Vienna,

Acknowledgment

First, my gratitude goes to Prof. Ernst Kozeschnik, for supporting me and my academic work on numerous levels. He never hesitated to share his experience and expertise in uncountable discussions. Thank you for supervising both, by Master's and PhD theses.

Furthermore, I would like to highlight Kurt, Tomasz, Christian, Edith, Heinz and Laszlo for standing by my side when conducting experiments. Their patience and expert knowledge enabled me to overcome various difficulties and experimental challenges.

Special thanks also go to Bernhard, Philipp and Daniela and to all the other colleagues of our work group who are not mentioned here, for your company throughout our years at TU Wien and beyond.

Finally, I would like to thank my family and my wife for supporting me during my time as PhD student.

Abstract

In this work, mechanical properties of aluminium alloys are described based on the current microstructure. Physically based models are combined with semi-empirical creep models to describe the plastic material behavior over an extended temperature and strain rate range. To integrate these models into a commercial FEA-Software, they are suitably simplified to ensure acceptable computational times for the description of complex components. These models are denoted in the work as ´Simple MicroStructure Evolution (sMSE) model´ and can be used as an underlying material model in, e.g., Abaqus and Ansys to calculate residual stresses in Al-cast alloys, for example.

Another focus of this work is the investigation of the deformation characteristics of binary Al-Mn, Al-Cu and Al-Zn alloys. The influence of the dissolved atoms on the yield stress and on the plastic deformation behavior is investigated. An advanced 3-Internal-Variables-Model (3IVM) is used to model the evolution of dislocation densities in the cell interior and cell wall. The model calibration is based on experimentally determined flow curves.

Kurzfassung

In dieser Arbeit werden mechanische Eigenschaften von Aluminiumlegierungen mit den vorliegenden Mikrostrukturzuständen verknüpft. Physikalisch basierte Modelle werden mit teils empirischen Kriechmodellen kombiniert, um plastisches Materialverhalten in einem erweiterten Temperatur- und Dehnratenbereich beschreiben zu können. Um diese Modelle in eine kommerzielle FEA-Software integrieren zu können, werden sie geeignet vereinfacht, um eine akzeptable Rechenzeiten für die Beschreibung komplexer Bauteile gewährleisten zu können. Diese Modelle werden in der Arbeit als ´Simple MicroStructure Evolution (sMSE) model´ zusammengefasst und dieses kann als zugrundeliegendes Materialmodell in Abaqus verwendet werden, um beispielsweise Eigenspannungen in Al-Gusslegierungen berechnen zu können.

Ein weiterer Schwerpunkt dieser Arbeit ist die Untersuchung der mechanischen Eigenschaften von binären Al-Mn, Al-Cu und Al-Zn Legierungen. Dabei wird der Einfluss der gelösten Atome auf die Streckgrenze und auf die plastische Verformung untersucht. Ein erweitertes 3-Internal-Variables-Model (3IVM) wird verwendet, um die Entwicklung der Versetzungsstrukturen im Zellinneren und in der Zellwand zu modellieren. Die Materialkalibrierung erfolgt durch experimentell ermittelte Fließkurven.

List of Publications

Journal Papers

2020	Viernstein, B., Kozeschnik, E., Integrated physical-constitutive computational framework for plastic deformation modeling, Metals, 10(7), pp. 1–13, 869.
2022	Viernstein, B., Tomasz W., Kozeschnik, E., State Parameter-Based Yield Strength Model for Integration in Finite Element User-Material Routines, Metals, 12(7), pp 1-16, 1207.
2024	Viernstein, B., Solyom, L., Kozeschnik, E., Strain Hardening in Dilute Binary Al-Cu, Al-Zn, and Al-Mn Alloys: Experiment and Modeling, Metall Mater Trans A, 55(11), pp 3627-3639

Conference Proceedings (presenting author)

Sep. 2019	EUROMAT conference, Stockholm. Viernstein, B., Kozeschnik, E., State parameter-based yield strength model for integration in Finite Element user-material routines
Feb. 2020	TMS conference, San Diego. Viernstein, B., Kozeschnik, E., State Parameter-Based Simulation of Temperature- and Strain Rate Dependent Flow Curves of Al-Alloys", in Light Metals 2020. The Minerals, Metals & Materials Series, pp. 267–271
Mar. 2021	MEFORM conference, Freiberg Viernstein, B., Kozeschnik, E., Computational analysis of deformation maps, The Metal Forming Conference MEFORM 2020, pp. 34–36.
Sep. 2021	EUROMAT conference, Graz. Viernstein, B., Kozeschnik, E., Integrated Physical-Constitutive Computational Framework for Plastic Deformation Modeling

Table of contents

1 Introduction 1
2 Objectives 2
3 State of the Art 3
3.1 Macroscopic deformation behavior 3
3.2 Stages of deformation 4
3.3 Deformation mechanisms 5
3.4 Constitutive stress-strain relations 6
3.5 Thermal stress contribution 7
3.5.1 Solid solution strengthening 9
3.5.2 Precipitation strengthening 10
3.5.3 Cross core diffusion effect 13
3.6 Athermal stress contribution 14
3.6.1 The Kocks Mecking model 14
3.6.2 The Kreyca model 15
3.6.3 The 3-Internal-Variables-Model (3IVM) 16
3.6.4 Microstructural influence on the athermal stress contribution 17
3.7 Creep mechanisms 19
3.7.1 Power law creep 19
3.7.2 Power law breakdown 20
3.7.3 Nabarro – Herring creep 20
3.7.4 Coble creep 21
3.7.5 Harper Dorn creep 21
3.7.6 Grain boundary sliding 22
4 Integrated model for plastic deformation 23
4.1 Physical-constitutive computational framework 23
4.2 Simple MicroStructure Evolution (sMSE) 24
4.3 Impact of solutes on plasticity 26
5 Experimental 27
5.1 Simple MicroStructure Evolution (sMSE) 27
5.2 Impact of solutes on plasticity 29
6 Simulation 32
6.1 Physical-constitutive computational framework 32

6.1.1 Stress relaxation 34
6.1.2 Deformation maps 35
6.2 Simple MicroStructure Evolution (sMSE) 36
6.2.1 Precipitation evolution 36
6.2.2 Deformation tests 38
6.3 Impact of solutes on plasticity 38
6.3.1 Dislocation density evolution 39
6.3.2 Flow curve simulations 41
7 Summary and conclusion 43
8 References 44
9 Appendix 50
Journal Paper 1 50
Journal Paper 2 71
Journal Paper 3 95
Conference Paper 118

1 Introduction

Socio-political and economic reasons motivate leading industrial companies to develop their products further to tap into new markets. Advanced material properties are constantly in demand to meet the increased requirements, such as CO_2 savings. The understanding of the underlying microscopic effects on material behavior is essential to specifically adapt material production routes or downstream processing steps. However, before well-established processes are changed, in general, laboratory experiments and computational simulations are performed to minimize the risk of failure. Due to the complexity of such process routes, sophisticated material models are mandatory. In the last decades, a variety of well-established microstructure models have been published and implemented in thermo-kinetic software packages, such as MatCalc, and underlay constant development and improvement. This thesis models the mechanical properties of various aluminium alloys, where stress-strain relations are investigated in a wide temperature- and strain-rate range. Thermal stress contributions, such as solid solution strengthening or precipitation strengthening, are taken into consideration, as well as the athermal stress contribution based on the dislocation density evolution. A suitable mathematical framework has been developed, experimentally validated, and integrated in the MatCalc software package. This work addresses both, academic issues, such as the influence of solutes in dilute binary aluminium alloys, and industry-related issues, such as the simulation of residual stresses of complex components in low calculation times.

2 Objectives

This thesis consists of three main sections, which can be considered separately, but are subordinate to a common topic – the simulation of plastic deformation in aluminium alloys. In the first part after the theoretical background (section 4.1), a new framework for the combination of physically based modelling of stress strain curves with empirical creep mechanisms is introduced. The necessity of this implementation in the MatCalc framework stems from an industrial project, where the aim was to calculate residual stresses in a temperature- and strain rate range, where creep becomes the dominant deformation mechanism. Since suitable material models were not available as input parameters for the FEM analysis, a condensed form of microstructure evolution models was developed and used in the Abaqus simulations, which is described in the second section of this thesis (section 4.2). The last part is mainly of academic interest and discusses the impact of solutes on both, the thermal stress contribution, which determines the yield stress, and the athermal stress contribution, which originates from the dislocation density evolution (section 4.3). The first chapters provide an overview of the underlying models whereas detailed derivations and descriptions are given in the journal papers in the Appendix.

3 State of the art

Uniaxial loading tests are usually performed to describe macroscopic material properties. The mechanical properties are determined by the microstructure and are strongly dependent on the test conditions. First, stress and strain are defined, followed by the description of the different stages of deformation. Moreover, the underlying models for the flow curve simulation are reviewed, including the athermal and the thermal stress contribution. In addition, the different creep mechanisms are introduced and its stress- and strain rate relation are illustrated in so-called deformation mechanism maps. This chapter should not be seen as a complete overview of all available models in literature, but as an introduction to the models which are used in this work.

3.1 Macroscopic deformation behavior

In this work, true stress σ and true strain φ are used for analyzing deformation tests and as simulation input parameters. The true stress is defined by

$$\sigma = \frac{F}{A}, \tag{1}$$

where F is the measured force and A is the actual cross section, which is defined by $A = A_0 l_0 / l$. l_0 is the initial length of the specimen, while l defines the measured length during the deformation process. The true strain φ is defined by

$$\varphi = \ln\left(\frac{l}{l_0}\right). \tag{2}$$

The Taylor factor M was first derived by Taylor [1] and relates the true stress with the resolved shear stress τ, acting on the glide planes of polycrystalline materials with

$$\sigma = M \cdot \tau. \tag{3}$$

According to Kocks [2], M = 3.06 for fcc materials. The relation between polycrystal deformation and single crystal deformation is also discussed in [3] and [4]. The macroscopic strain φ is related to the resolved strain γ by

$$\varphi = \gamma / M. \tag{4}$$

A scheme of a typical flow curve is shown in Figure 1 (a), starting from the yield stress σ_0. With increasing strain, the plastic stress σ_p increases, until a saturation stress σ_sat is reached, if only Stage III hardening is considered (see section 3.2). Figure 1 (b) shows a Kocks-Mecking plot, which relates the hardening rate $\theta = \frac{d\sigma}{d\varepsilon}$ with the stress σ, where θ_0 is the initial hardening rate at the yield stress σ_0. θ linearly decreases until the saturation stress is reached.

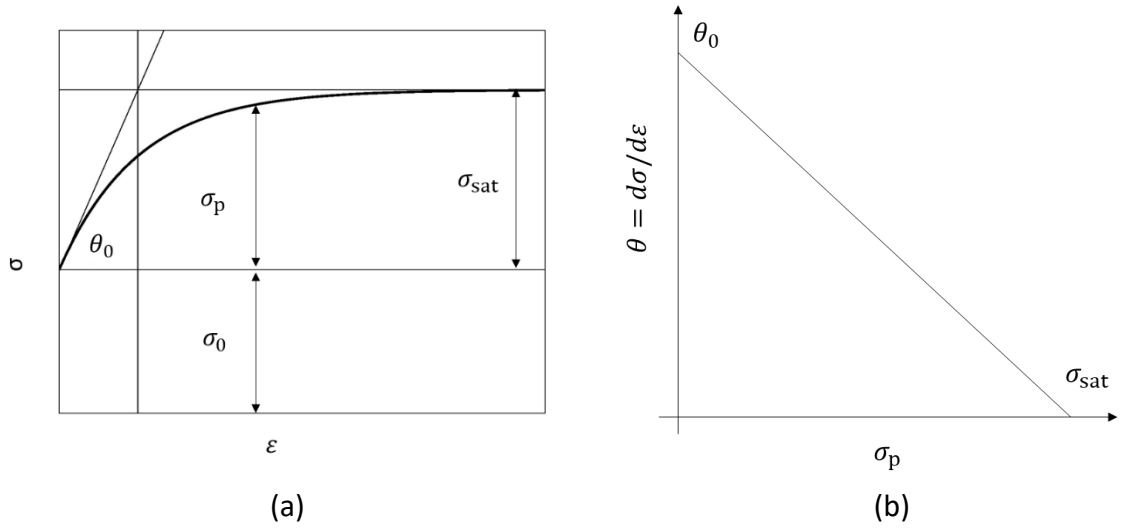

Figure 1. Scheme of (a) a flow curve and (b) a Kocks-Mecking plot for Stage III hardening.

3.2 Stages of deformation

Common stress-strain curves, as shown schematically in Figure 2 (a), can be divided into five stages, as suggested by [5] and [6]. For the transition of each deformation state, a Kocks-Mecking plot is often used, as described in the previous subchapter. In Stage I, which is also called Easy Glide, only one slip system is active and appears only in single crystals and is characterized by a very low hardening rate. At higher strains, secondary slip systems are activated, and the hardening rate rapidly increases in Stage II due to pile up of dislocations. The initial strengthening rate θ_0 is about G/20 [7], which is about 1200-1500 MPa at room temperature for pure Al. Solutes within the Al matrix can affect θ_0, as analyzed in this work. In Stage III, the hardening rate linearly decreases as shown in Figure 2 (b). The stress increases due to strengthening effects, but at the same time, recovery by cross slip of screw dislocations and climbing of edge dislocations take place until these effects compensate each other and a saturation stress is reached. The slope of the Kocks-Mecking plot represents the rate of dynamic recovery and is, therefore, strongly microstructure-, temperature- and strain rate-dependent. Stage IV can be interpreted as a formation of a substructure, where wall

dislocations are generated, which increase the misorientation of two cells. Some authors describe a subsequent stage V, where the stress saturates [8].

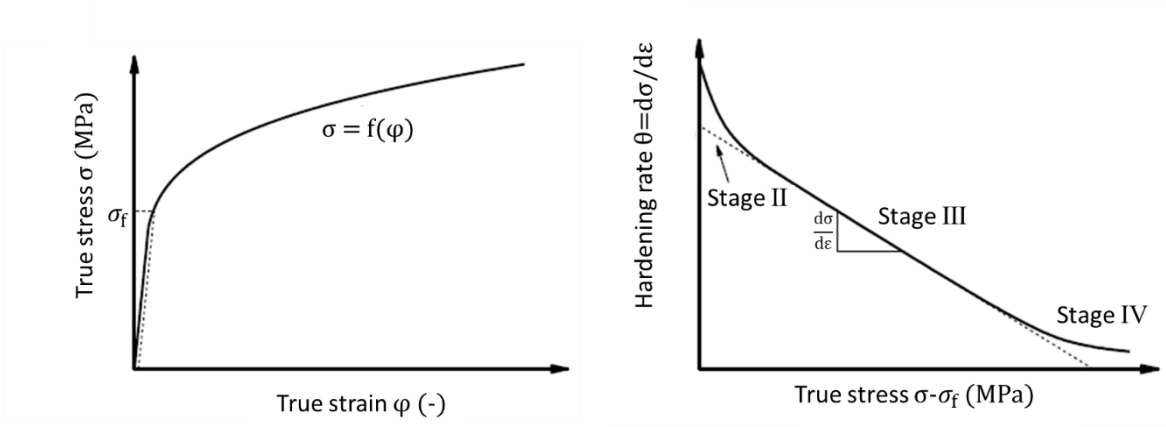

(a) (b)

Figure 2. Schemes of (a) a true stress strain curve and (b) a Kocks-Mecking plot.

3.3 Deformation mechanisms

When a material is plastically deformed, many deformation mechanisms take place simultaneously. However, one mechanism dominates and determines the mechanical properties. Deformation maps, as described by Frost and Ashby [9], provide an overview of the active mechanisms for specific combinations of stress, strain rate and temperature, as shown exemplarily in Figure 3 for pure Al and a grain diameter of 10 µm. Dislocation glide is generally dominant at low temperatures, while power law creep and diffusional flow, which are diffusion-controlled mechanisms, become dominant at higher temperatures. In this region, edge dislocations start to climb due to the motion of vacancies and is therefore time dependent. Consequently, these regions are characterized by a high strain rate dependency. The creep mechanisms, such as power law creep, diffusional flow and the power law breakdown are described in chapter 3.7.

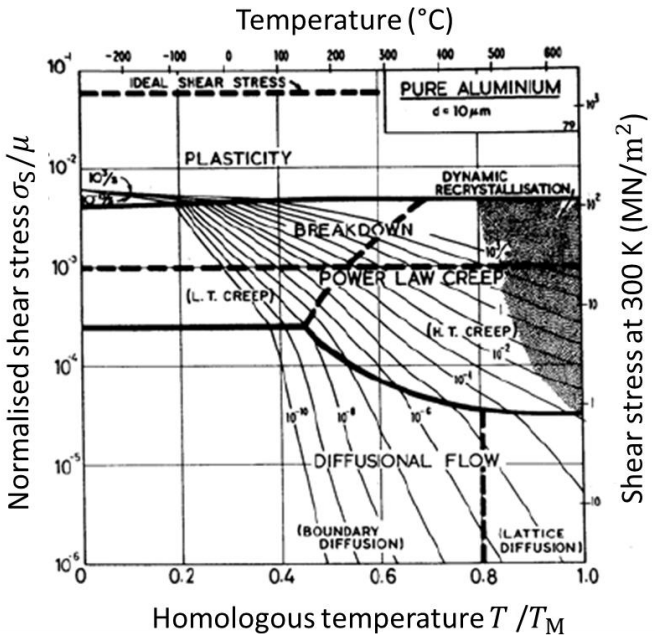

Figure 3. Deformation mechanism map for pure Al, including the dislocation glide range, the power law creep range, the power law breakdown area, and the diffusional flow area. (Reproduced from Frost and Ashby [9])

3.4 Constitutive stress-strain relations

Constitutive models can be used to reproduce temperature- and strain rate-dependent stress-strain relations, but in general without taking the microstructure development into account. Examples for constitutive models are the Ludwik approach [10], the Voce type approach [11], the Johnson-Cook model [12], the Zerilli–Armstrong model [13], or the model of Khan and Huang [14]. The advantage of using constitutive models, especially when included in Finite Element Analyses (FEA) tools, is the low calculation time. Furthermore, if the number of different experimental setups is limited, one set of calibration parameters leads to a good reproduction of stress strain curves. In general, many constitutive models are based on the product form of the temperature- and strain rate-dependent function *f(T, $\dot{\varepsilon}$)* and the strain dependent reference stress $\sigma_{\mathrm{ref}}(\varepsilon)$

$$\sigma(T, \dot{\varepsilon}, \varepsilon) = f(T, \dot{\varepsilon}) \cdot \sigma_{\mathrm{ref}}(\varepsilon). \tag{5}$$

Examples of this product form are given in [15]. If the microstructure changes during the thermo-mechanical treatment, constitutive models are not suitable anymore and state parameter-based yield strength models are used, like [16–32]. Examples for state parameters

are the dislocation density, the solute content within the matrix, the radius, and the phase fraction of the precipitates. In the following, the model of Kreyca is used [33] as a starting point and extended by the creep relations. The thermal and the athermal stress contributions are distinguished, as described in the following subchapters.

3.5 Thermal stress contribution

Since mobile dislocations ρ_{m} carry plastic strain, the interaction of these dislocations with obstacles within the glide plane determine the rate of flow. The strain rate $\dot{\varepsilon}$ is given by the Orowan equation [34]

$$\dot{\varepsilon} = \rho_{\mathrm{m}} \cdot b \cdot v, \tag{6}$$

where *b* is the Burger's vector, and *v* is the velocity of the dislocation, which is given by the Arrhenius Ansatz

$$v = c \cdot \left(\exp\left(\frac{-\Delta G}{k_{\mathrm{B}} T}\right)\right). \tag{7}$$

c is the speed of sound, ΔG is the Gibbs energy, k_{B} is the Boltzmann constant and *T* is the temperature. The Gibbs energy depends on the distribution and the strength of the obstacles and is often assumed to be

$$\Delta G = \Delta F \left(\left(1 - \left(\frac{\sigma}{\hat{\sigma}}\right)^{p} \right) \right)^{q}, \tag{8}$$

where ΔF is the activation energy. The mechanical threshold $\hat{\sigma}$ is the stress, which is needed to overcome the energy barrier at 0 K. The exponents *q* and *p* characterize the shape of the energy barrier. In this work, a regular array of box-shaped obstacles is assumed, leading to *p* = *q* = 1. Combining Equations (6),(7) and (8) leads with $\Delta F = \alpha G b^2$ [9] to

$$\sigma = \hat{\sigma} \left(1 - \left(\frac{k_{\mathrm{B}} T}{\Delta F} \ln\left(\frac{\dot{\varepsilon}_0}{\dot{\varepsilon}}\right) \right)^{\frac{1}{q}} \right)^{\frac{1}{p}}. \tag{9}$$

α is the strengthening coefficient and $\dot{\varepsilon}_0 = \rho_{\mathrm{m}} \cdot b \cdot c$, which can be treated as a constant in a first approximation, if ρ_{m} is substituted by the equilibrium dislocation density ρ_{eq}. This can be justified for the present high activation energy ΔF and is in the same range of magnitude

compared to values from literature [9]. The physical meaning of Equation (9) is limited, because the stress σ becomes zero at a critical temperature. Kreyca suggests following equation instead, whereas the subscript 'lt' emphasizes the validity at low temperatures, when dislocation motion is characterized by glide processes

$$\sigma_{\mathrm{lt}} = \hat{\sigma} \cdot \exp\left(\frac{-k_{\mathrm{B}} \cdot T}{\Delta F_{\sigma_0}^{\mathrm{lt}}} \cdot \ln\left(\frac{\dot{\varepsilon}_0}{\dot{\varepsilon}}\right)\right). \tag{10}$$

The subscript 'σ_0' refers to the initial yield stress. The mechanical threshold $\hat{\sigma}$ is defined by the sum of a basic stress, solid solution hardening (see section 3.5.1), precipitation hardening (3.5.2), cross core diffusion hardening (3.5.3), grain size hardening and sub-grain size hardening in the absence of thermal activation. Figure 4 shows the thermal activation factor $\sigma/\hat{\sigma}$ for different values of p and q of Equation (9) as well as the low temperature approximation of Equation (10) as a function of the homologous temperature T/T_{m}.

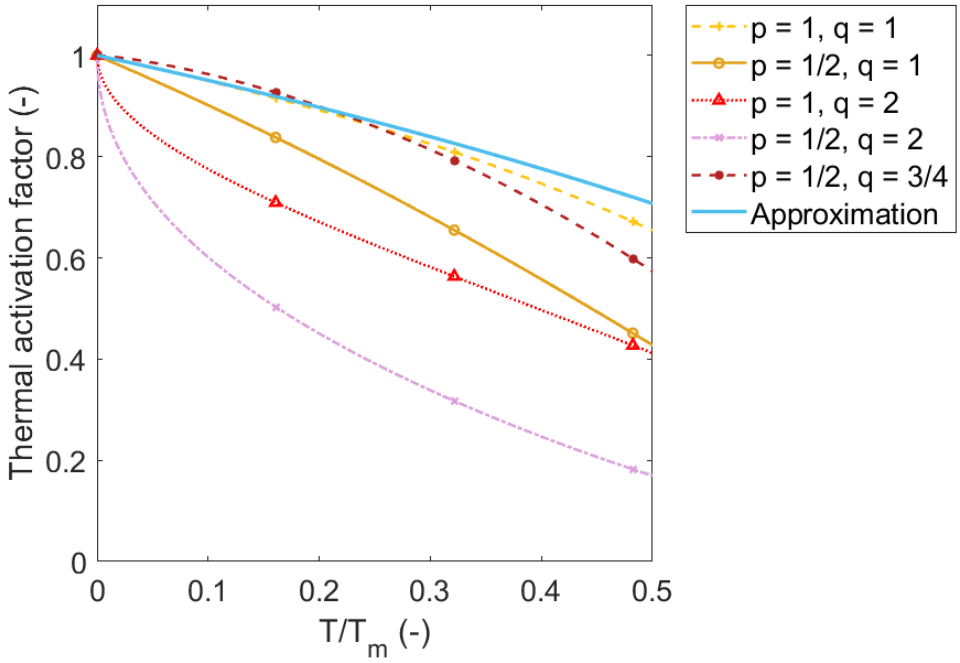

Figure 4. Thermal activation factor $\sigma/\hat{\sigma}$ as a function of the homologous temperature T/T_m for different combinations of p and q of Equation (9). The approximation represents σ_{lt} of Equation (10).

At high temperatures, dislocation climb becomes dominant and the following stress contribution can be used [33]

$$\sigma_{\mathrm{ht}} = \left(\hat{\sigma} \cdot \frac{\dot{\varepsilon}^* \cdot k_{\mathrm{B}} \cdot T \cdot (\alpha \cdot b \cdot G)^2}{2bc\Delta F_{\sigma_0}^{\mathrm{ht}} \cdot exp\left(-\frac{\Delta F_{\sigma_0}^{\mathrm{ht}}}{k_{\mathrm{B}} T}\right)} \right)^{\frac{1}{n}}. \tag{11}$$

G is the shear modulus, and the exponent *n* of the power law equation varies between 3 and 10 [9]. For appropriate stress-strain simulations, the strain rate dependency is modified by $\dot{\varepsilon}^* = \dot{\varepsilon}^{n_{\dot{\varepsilon}}}$ in the present framework. The activation energies $\Delta F_{\sigma_0}^{\mathrm{lt}}$ and $\Delta F_{\sigma_0}^{\mathrm{ht}}$ depend on the effective solute concentrations in the matrix and are, therefore, strongly microstructure-dependent. The total thermal stress σ_0 is given by the summation rule

$$\sigma_0 = \left(\left(\frac{1}{\sigma_{\mathrm{lt}}} \right)^{n_c} + \left(\frac{1}{\sigma_{\mathrm{ht}}} \right)^{n_c} \right)^{\frac{1}{n_c}}, \tag{12}$$

where n_{c} is a coupling coefficient. In the following subchapters, the contributions of solid solution strengthening, precipitation strengthening, and the cross-core diffusion effect are discussed.

3.5.1 Solid solution strengthening

The addition of solute atoms strengthens pure Al and increases the yield stress. Solid solution strengthening is caused by parelastic-, dielastic- and chemical interaction forces of the solutes and dislocations [35]. Parelastic interaction is caused by the interaction of stress fields of dislocations with the elastic distortion of the matrix, caused by solute additions [36]. Dielastic interaction is caused by a different shear modulus in the vicinity of a solute, which leads to a change in the dislocation line energy. Solutes can lower the stacking fault energy leading to an increased necessary stress for a dislocation to break free from a solute atmosphere (chemical interaction) [35,36].

In general, strong-pinning models (Friedel [37], Fleischer [38]) and weak-pinning models (Mott [39], Labusch [40]) can be distinguished. In the Friedel model, each solute is considered as an independent obstacle that pins the dislocation. The critical stress τ_c is a function of the spacing of solutes, defined by the Friedel length [35], with

$$\tau_c^F = F_{\max}^{3/2} \frac{c^{1/2}}{b(2E_{\mathrm{L}})^{1/2}}. \tag{13}$$

The maximum interaction force is defined by [41]

$$F_{\max} = \frac{\sqrt{3}}{2} \cdot \frac{(1+\nu)}{(1-\nu)} \cdot G \cdot b^2 |\varepsilon_{\mathrm{m}}|. \quad (14)$$

ν is the Poisson's ratio, ε_{m} is the misfit strain between solute and matrix atoms and the dislocation line tension $E_{\mathrm{L}} = \frac{1}{2} \cdot G \cdot b^2$ [42].

Labusch considers the interaction of many solutes around a dislocation and uses a distribution function, describing the number of interactions of a specific strength with the unit length of a dislocation at a given stress [35]. The critical stress is [43]

$$\tau_{\mathrm{c}}^{\mathrm{L}} = \left(\frac{c^2 U_{\max}^4}{w b^9 E_{\mathrm{L}}} \right)^{1/3}. \quad (15)$$

$w = 5b$ and $U_{\max}$ is the maximum solute-dislocation interaction energy.

As Leyson demonstrated in [44], the Labusch model controls the strengthening for concentrations greater than 10^{-4} and temperatures above 78 K for Al alloys. Therefore, the Labusch model is used for the simulation of solid solution strengthening in this work.

3.5.2 Precipitation strengthening

For the calculation of the precipitation strengthening contribution, knowledge of the number density, the radius, and the phase fraction of the existing precipitates is mandatory. The precipitation evolution models have been developed by Svoboda, Fischer, Fratzl and Kozeschnik (SFFK), and are described in detail in [45–47]. The basic equations are summarized in the following. The steady-state nucleation rate is defined as the number of newly formed precipitate nuclei per unit volume and unit time as [48,49]

$$J = N_0 \cdot Z \cdot \beta^* \cdot e^{\frac{-G^*}{k_{\mathrm{B}} T}}. \quad (16)$$

N_0 is the number of available nucleation sites, Z is the Zeldovich factor, β^* is the atomic attachment rate, and G^* is the critical nucleation energy. The Zeldovich factor is expressed as [48,50]

$$Z = \left(\frac{b^6}{64\pi^2 k_{\mathrm{B}} T} \frac{\left(\frac{d_{\mathrm{m}}}{\nu^\alpha}\right)^4}{\gamma^3} \right)^{\frac{1}{2}}. \quad (17)$$

ν^α represents the molar volume of the precipitate and γ is the specific interfacial energy. The critical nucleation energy is given by

$$G^* = \frac{16\pi}{3}\frac{\gamma^3}{\left(\frac{d_\mathrm{m}}{\nu^\alpha}\right)^2}. \tag{18}$$

d_m is the driving force, which exists if the total Gibbs energy of the system can be lowered by the formation of a new phase. For the calculation of the driving force, thermodynamic databases are necessary, which are included in MatCalc (www.matcalc.at), a software package which is used for the simulations in this work. The atomic attachment rate reads

$$\beta^* = \frac{4\pi {r_\mathrm{crit}}^2}{b^4} D_\mathrm{eff}, \tag{19}$$

with the critical radius

$$r_\mathrm{crit} = \frac{2\gamma}{\frac{d_\mathrm{m}}{\nu^\alpha}}. \tag{20}$$

Since the nucleation and the growth of precipitates are diffusion-controlled processes, the effective matrix diffusion coefficient D_eff plays a key role in the microstructure evolution. The effective diffusion coefficient includes trapping of vacancies at solute atoms [51], excess vacancies [52] and dislocation pipe diffusion enhancement [53,54]. The excess vacancies are included with

$$D_\mathrm{eff} = D_0 \cdot \exp\left(\frac{-Q}{R \cdot T}\right) \cdot \left(\frac{X_\mathrm{Va}}{X_\mathrm{Va,eq}}\right). \tag{21}$$

X_Va is the current vacancy concentration and $X_\mathrm{Va,eq}$ is the equilibrium vacancy contribution. A comprehensive discussion of all precipitation strengthening mechanisms, which are included in this work, is given by Ahmadi [55]. In the following, a summary of these models is given, excluding detailed mathematical expressions. Precipitation strengthening is based on the interaction of moving dislocations with precipitates within the matrix. In general, small coherent precipitates are sheared by moving dislocations, while dislocation loops, which are called Orowan loops, are formed around bigger, incoherent precipitates.

When a dislocation bows out at spherical precipitates because of an external force, the equilibrium between the acting shear stress, the dislocation line tension *T*, the dislocation bending angle (outer cut-off angle) ψ and the precipitate resistance force *F* delivers

$$\tau b L = 2T \cdot \cos\left(\frac{\psi}{2}\right) = F. \tag{22}$$

L is the distance between two particles, as shown in Figure 5. If the critical angle ψ_c is between $120° \leq \psi_c \leq 180°$, the precipitate is denoted as weak, whereas the particle is considered as strong when ψ_c is between $0° \leq \psi_c \leq 120°$.

For weak and shearable precipitates, Equation (22) becomes

$$\tau = \frac{2T}{bL_{\text{eff}}} \cdot \cos\left(\frac{\psi_c}{2}\right), \tag{23}$$

when the effective distance L_{eff} is used. L_{eff} is visualized in the scheme in Figure 5. $L_{\text{eff}} \geq L$ for weak precipitates because a dislocation cuts a precipitate when the angle ψ_c is between 120° and 180° and is released from the particle earlier.

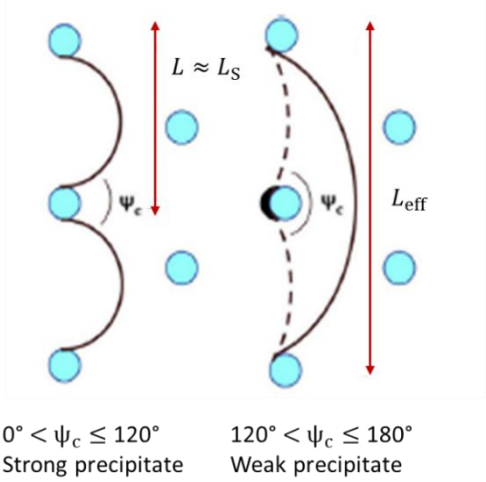

Figure 5. Distance between two precipitates for strong and weak shearable precipitates, adapted from Ahmadi [55].

The relation between L_S and L_{eff} reads [55]

$$L_s = L_{\text{eff}} \cdot \left[\cos\left(\frac{\psi_c}{2}\right)\right]^{\frac{1}{2}}. \tag{24}$$

For weak particles, the combination of Equations (22),(23) and (24) leads to

$$\tau = \frac{2T}{bL_S} \cdot \left(\frac{F_m}{2T}\right)^{\frac{3}{2}}, \tag{25}$$

where F_m is the maximum interaction force between the precipitates and the dislocation with $F_m = 2T\cos\left(\frac{\psi_c}{2}\right)$. For strong particles the shear stress τ is derived by

$$\tau = J\frac{F_{\mathrm{m}}}{bL_{\mathrm{S}}}, \tag{26}$$

where J is a correction parameter for a random arrangement of particles. F_{m} is strongly dependent on the prevailing interaction mechanisms, which are discussed in detail in [55].

3.5.3 Cross-core diffusion effect

Material strengthening due to the cross-core diffusion effect is based on the interaction of diffusing solutes with the stress fields of dislocations, leading to dynamic strain aging (DSA). Possible negative strain rate sensitivity can lead to plastic material instabilities due to local material softening [56]. The Portevin-LeChatelier effect is a well-known example for DSA leading to serrated stress-strain behavior. The cross-core diffusion effect is included to the present framework as developed by Curtin et al. [56]. It is based on single atomic jumps of solutes from the compression side to the tension side in the core of a dislocation, as

$$\Delta\tau_{\mathrm{s}}(\dot{\varepsilon}) = \alpha\left(\frac{2c_0\overline{\Delta W}}{\sqrt{3}b^3}\right)\tanh\left(\frac{\overline{\Delta W}}{2k_{\mathrm{B}}T}\right)\left[1 - e^{-6\cosh\left(\frac{\overline{\Delta W}}{2k_{\mathrm{B}}T}\right)\mathrm{r}_c\frac{\Omega}{\dot{\varepsilon}}}\right]. \tag{27}$$

$\alpha = 0.56$, c_0 is the bulk solute concentration, $\overline{\Delta W}$ is the average binding energy difference between the core compression and tension sites, Ω is a constant in this framework, $\mathrm{r_c}$ is the reference core transition rate with

$$\mathrm{r}_c = \nu_0 e^{\frac{-\Delta H_{\mathrm{c}}}{k_{\mathrm{B}}T}}, \tag{28}$$

where ν_0 is the attempt frequency and ΔH_{c} is the average activation enthalpy for transitions from tension to compression and vice versa. Since the cross-core diffusion effect is a diffusion-driven process, higher temperatures and smaller strain rates facilitate cross-core diffusion strengthening. For the calculation of solid solution strengthening and the activation energies ΔF (see section 3.5), the effective concentration of solutes on the tension side of a dislocation core is relevant, given by [56]

$$c_{\mathrm{eff}} = c_0 + c_0\tanh\left(\frac{\overline{\Delta W}}{2k_{\mathrm{B}}T}\right)\left[1 - e^{-6\cosh\left(\frac{\overline{\Delta W}}{2k_{\mathrm{B}}T}\right)\mathrm{r_c}\frac{\Omega}{\dot{\varepsilon}}}\right]. \tag{29}$$

The strengthening contribution $\Delta\tau_{\mathrm{s}}$ is added to the mechanical threshold $\hat{\sigma}$.

3.6 Athermal stress contribution

The athermal stress contribution describes the hardening effect, which is directly related to the total dislocation density ρ_{tot} and is given by the Taylor equation

$$\sigma_{\mathrm{p}} = g_1 \cdot \sqrt{\rho}, \tag{30}$$

with $g_1 = \alpha \cdot M \cdot b \cdot G$. The following subchapters describe different ways to model dislocation generation and annihilation. Please note that this selection is not exhaustive but is an important basis of the models used in this work. Starting with the Kocks-Mecking approach [16], an average dislocation density is considered, where a dislocation generation term and dynamic recovery are considered.. The Kreyca model also includes static recovery, based on climbing processes. The 3IVM, which was first developed by Roters et al. [20], distinguishes between mobile dislocations and immobile dislocations in the cell interior and cell walls.

3.6.1 The Kocks Mecking model

The average dislocation density evolution due to plastic deformation can generally be described as

$$\frac{d\rho}{d\varepsilon} = \frac{d\rho^{+}}{d\varepsilon} + \frac{d\rho^{-}}{d\varepsilon}, \tag{31}$$

where $\frac{\mathrm{d}\rho^{+}}{\mathrm{d}\varepsilon}$ accounts for the dislocation generation, while $\frac{\mathrm{d}\rho^{-}}{\mathrm{d}\varepsilon}$ represents dislocation annihilation by dynamic recovery. The generation term is related to the mean free path *L*, as

$$\frac{d\rho^{+}}{d\varepsilon} = \frac{M}{bL}. \tag{32}$$

L is inversely proportional to the square root of the dislocation density as

$$L = \frac{A}{\sqrt{\rho}}, \tag{33}$$

where *A* is a proportional constant. Equation (31) becomes with Equation (32)

$$\frac{d\rho}{d\varepsilon} = k_1\sqrt{\rho} - k_2\rho, \tag{34}$$

with k_1=*M/bA.* With Equation (30), Equation (34) can be alternatively written as

$$\frac{d\sigma}{d\varepsilon} = \frac{k_1 g_1}{2} - \frac{k_2}{2}\sigma, \tag{35}$$

which is equivalent to the Voce form [57].

3.6.2 The Kreyca model

Kreyca and Kozeschnik [33] used the following extended one-parameter model of Kocks and Mecking to calculate the temperature- and strain rate-dependent dislocation density evolution, as

$$\frac{\mathrm{d}\rho}{\mathrm{d}\varepsilon} = \frac{\mathrm{d}\rho^{+}}{\mathrm{d}\varepsilon} + \frac{\mathrm{d}\rho^{-}}{\mathrm{d}\varepsilon} + \frac{\mathrm{d}\rho_{\mathrm{s}}^{-}}{\mathrm{d}\varepsilon} = \frac{M}{bA}\sqrt{\rho} - 2BM\frac{d_{\mathrm{crit}}}{b}\rho - 2CD_{\mathrm{d}}\frac{Gb^3}{\dot{\varepsilon}kT}\left(\rho^2 - \rho_{\mathrm{eq}}^2\right). \tag{36}$$

A, *B* and *C* are material-specific coefficients, ρ_{eq} is the equilibrium dislocation density and d_{crit} is the critical annihilation distance between two dislocations [58] with

$$d_{\mathrm{crit}} = \frac{Gb^4}{2\pi(1-\nu)Q_{\mathrm{vac}}}. \tag{37}$$

Q_{vac} is the vacancy formation energy. In addition to the annihilation of dislocations due to cross-slip processes at low and intermediate temperatures, vacancy-assisted climb $\frac{\mathrm{d}\rho_s^{-}}{\mathrm{d}\varepsilon}$ occurs at high temperatures. The latter annihilation process represents static recovery, which is marked by the index 's'. According to Kreyca [33], $A(\dot{\varepsilon}, T)$, $B(\dot{\varepsilon}, T)$ and $C(\dot{\varepsilon}, T)$ can be related to the initial slope θ_0 and the saturation stress σ_{sat} of a stress-strain curve by

$$A = \frac{g_1 M}{2b\theta_0}, \tag{38}$$

$$B = \frac{b\theta_0}{\sigma_{\mathrm{sat}}^{\mathrm{lt}} d_{\mathrm{crit}} M}, \tag{39}$$

$$C = \frac{g_1^2}{\left(\sigma_{\mathrm{sat}}^{\mathrm{ht}}\right)^3}\frac{\theta_0 \dot{\varepsilon} kT}{D_{\mathrm{d}} Gb^3}, \tag{40}$$

Like σ_0^{lt} and σ_0^{ht} in Equations (10) and (11), the saturation stress can be distinguished in $\sigma_{\mathrm{sat}}^{\mathrm{lt}}$ and $\sigma_{\mathrm{sat}}^{\mathrm{ht}}$ for two temperature regimes to consider both, thermally activated glide at low temperature as well as vacancy-assisted climb at high temperature. Since θ_0 and σ_{sat} are temperature- and strain rate-dependent in the model of Kreyca, the parameters *A*, *B* and *C*

are no longer constants anymore in contrast to the Kocks-Mecking approach. For detailed explanation of θ_0, $\sigma_\infty^{\mathrm{lt}}$ and $\sigma_\infty^{\mathrm{ht}}$, see [33].

3.6.3 The 3-Internal-Variables-Model (3IVM)

The 3IVM, which was originally developed by Roters et al. [59], distinguishes between the mobile dislocations, the immobile dislocations in the cell interior and the immobile dislocations within the cell walls. Internal dislocations ρ_{int} are defined as the sum of mobile dislocations ρ_{m} and immobile dislocations ρ_{im} in the cell interior. Mobile dislocations are produced at dislocation sources and move through the cell interiors and cell walls until they get locked or annihilated. The generation of mobile dislocations ($\dot{\rho}_{\mathrm{m}}^{+}$) is inversely dependent on the effective mean free path, where the interaction with other internal dislocations as well as wall dislocations, the grain diameter and precipitates are taken into consideration. Mobile dislocations are reduced by annihilation due to dislocation glide ($\dot{\rho}_{\mathrm{m,ann}}^{-}$), the formation of dipoles ($\dot{\rho}_{\mathrm{m,dip}}^{-}$) and locks ($\dot{\rho}_{\mathrm{m,lock}}^{-}$). Dipoles form, if two antiparallel mobile dislocations interact, but are too far away to annihilate. Dislocation dipoles are swept into the cell walls and do not contribute to the plastic deformation anymore. Dislocation locks can form, when two dislocations come closer to each other than a critical distance and move on different slip planes. At higher temperatures, mobile dislocations annihilate due to climbing processes ($\dot{\rho}_{\mathrm{m,climb}}^{-}$). Since all experiments are conducted at room temperature in this framework, climbing processes can be neglected. The overall evolution equation of the mobile dislocation density is

$$\dot{\rho}_{\mathrm{m}} = \dot{\rho}_{\mathrm{m}}^{+} - \dot{\rho}_{\mathrm{m,ann}}^{-} - \dot{\rho}_{\mathrm{m,dip}}^{-} - \dot{\rho}_{\mathrm{m,lock}}^{-} - \dot{\rho}_{\mathrm{m,climb}}^{-}. \tag{41}$$

The production rate of immobile dislocations ρ_{im} in the cell interior is equal to the formation rate of dislocation locks. These immobile dislocations can annihilate by climbing.

Dipoles form inside the cells and are swept into the cell walls (ρ_{w}), as originally proposed in [60]. In the present framework, only diffusion-controlled climbing reduces the wall dislocation density. The overall wall dislocation density is given by the weighted sum of the internal dislocation density, $\dot{\rho}_{\mathrm{w,dip}}^{+}$ and $\dot{\rho}_{\mathrm{dip}}^{-}$. The total dislocation density is then

$$\rho_{\mathrm{tot}} = f_{\mathrm{ci}} \cdot \rho_{\mathrm{int}}(t) + f_{\mathrm{cw}} \cdot \rho_{\mathrm{w}}(t), \tag{42}$$

where f_{ci} and f_{cw} are the volume fractions of cell interiors and cell walls.

3.6.4 Microstructural influence on the athermal stress contribution

The mechanical properties of a material are determined by the microstructure, including solutes, precipitates, or the grain size. The mechanical threshold concept is considered for calculating the yield stress, as described in section 3.5. Plastic deformation behavior is based on the motion of dislocations, where the formation of new dislocations is also dependent on microstructural features. A descriptive way to illustrate the influence of the microstructure on the athermal stress contribution is by using the KM plot.

A decreasing slope of the KM plot due to solute additions can be interpreted as a decrease in the stacking fault energy and the attendant drop in the cross-slip probability of dislocations [61]. Since double cross slip results in a new Frank-Read source, as described in detail in [62], a decreased stacking fault energy facilitates the dynamic recovery of dislocations. A shift of the KM plot on the stress axis can also be explained by the influence of the critical annihilation distance for dynamic recovery, due to local solute concentration in the dislocation core [63].

Besides influencing the yield stress by the Hall-Petch relation, the grain size has an impact on the strain hardening behavior. In the 3IVM, the grain size influences the effective slip length L_{eff} and therefore the generation term of the mobile dislocations. Since dislocation locks are formed by the immobilization of mobile dislocations, also ρ_{im} increases with decreasing grain size. In contrast to the 3IVM, Ashby proposed in [64] to calculate immobile, geometrically necessary dislocations (GNDs) to ensure compatibility at grain boundaries, as

$$\rho_{\mathrm{grain}}^{\mathrm{G}} \cong \frac{\bar{\varepsilon}}{4bd}, \tag{43}$$

where $\bar{\varepsilon}$ is the overall macroscopic strain of a polycrystalline material and *d* is the grain size. The additional stress contribution is calculated by the Taylor Equation (18). Goerdeler compared the 3IVM with the Ashby model for grain sizes between 1 μm and 1000 μm in [35], showing that the behavior of the stress-strain curves is in principle similar, but at low strains, the effect of grain size is less for the Ashby Ansatz, but increases more strongly with increasing strain.

Precipitates affect the stress-strain behavior by influencing the mechanical threshold, as described in section 3.5, as well as by the influence of the athermal stress. Kreyca et al. [65] show for a 6061 Al alloy that the yield stress increases with increasing annealing time until

peak aging, but at the same time the strain hardening rate decreases. The analyzed temperatures in their work are between 25 °C and 400 °C, where the strongest effect occurs at a temperature of 200 °C. At 400 °C, the β'' precipitates are already dissolved, leading to identical microstructures at the start of the deformation, independently of the aging time.

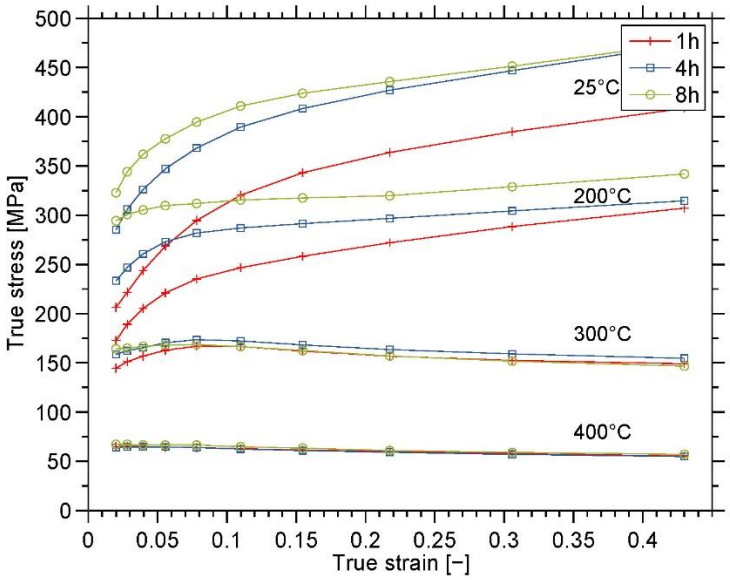

Figure 6. Stress strain relations of a 6061 Al alloy for different annealing times and deformation temperatures, reproduced from [65].

The phenomenon of decreasing strain hardening rate with increasing precipitation strengthening until peak aging is also observed in [66–68]. Local softening of shearable precipitates is described by Hornbogen et al., [69,70]. The transition from shearable to non-shearable precipitates can be seen in a change in the macroscopic work hardening behavior, characterized by an increase of the initial hardening rate as well as a steeper slope of the σ-θ plot, as shown in [71] and [72]. Different models exist, describing the impact of the precipitates on strain hardening, but only a few are reviewed here. In the 3IVM, non-shearable precipitates influence the effective slip length and have a direct influence on the mobile dislocation storage rate. Shearable precipitates are assumed to have negligible contribution to the dislocation storage process, which is also reported in [67,73]. Marthinsen et al. [74] take geometrically necessary dislocations into account and calculate L_{eff} for the presence of non-deformable particles with

$$L_{\mathrm{eff}} = \frac{c}{\sqrt{\rho + \left(\frac{c}{L_{\mathrm{G}}}\right)^2}}, \tag{44}$$

where *C* is a constant and L_{G} is the geometrical slip distance with

$$\left(\frac{1}{L_{\mathrm{G}}}\right)^2 = \kappa_2^2 \left(\left(\frac{1}{d}\right)^2 + \left(\frac{2f_{\mathrm{r}}}{r}\right)^2\right). \tag{45}$$

$\kappa_2 \sim 1$, *d* is the grain size, *r* is the particle radius and f_{r} is the volume fraction.

In the present work, the impact of precipitates is restricted to the mechanical threshold concept to keep the model simple. This is justified in this setup, since the part of the work where precipitates can form focuses on the calculation of the yield stress.

3.7 Creep mechanisms

For the simulation of internal stresses within complex structures, creep mechanisms need to be included to the framework which become dominant at high temperatures and low strain rates. An overview of the dominant creep mechanisms that are considered in this modelling, such as Coble creep, Nabarro Herring creep or Harper Dorn creep, is given in [75] and in the following subchapters. All creep mechanisms are diffusion-controlled, either by lattice diffusion, pipe diffusion or grain boundary diffusion.

3.7.1 Power law creep

The following phenomenological correlation between the strain rate $\dot{\varepsilon}$ and the applied shear stress σ_{s} is often successfully applied in literature [33,76,77]. It is also included within this framework as

$$\dot{\varepsilon} = \frac{A \cdot D_{\mathrm{tr}} \cdot G \cdot b}{k_{\mathrm{B}} \cdot T} \cdot \left(\frac{\sigma_{\mathrm{s}}}{G}\right)^n. \tag{46}$$

A is a material dependent coefficient, D_{tr} is the tracer diffusion coefficient of the matrix-forming element. Frost and Ashby [78] included dislocation core diffusion in addition to the bulk matrix diffusion due to missing explanations for the observed values of *n* and a huge variation in *A* of many orders of magnitude. Based on these two kinds of diffusion mechanisms, two rate equations are obtained. Dislocation core diffusion is dominant at low temperatures or high stresses, while lattice diffusion is the dominant mechanism at high temperatures and low stresses. Low-temperature creep, LT creep, and high-temperature creep, HT creep, are distinguished in Equations (47) and (48). The strain rate, $\dot{\varepsilon}_{\mathrm{HT}}$, for HT creep reads

$$\dot{\varepsilon}_{\mathrm{HT}} = \frac{A_{\mathrm{HT}} \cdot G \cdot b \cdot D_{\mathrm{eff}}}{k_{\mathrm{B}} \cdot T} \cdot \left(\frac{\sigma_{\mathrm{S}}}{G}\right)^{n_{\mathrm{HT}}}, \tag{47}$$

where n_{HT} is a constant and A_{HT} is microstructure-dependent within the present framework (see section 4.1). The effective diffusion coefficient D_{eff} is dominated by the migration of vacancies, which are created and annihilated at grain boundaries, dislocation jogs or Frank loops. A detailed description of the FSAK model is given in [52]. Based on the pipe diffusion effect, the effective diffusion coefficient is dependent on the dislocation density and therefore increases during the deformation. The strain rate $\dot{\varepsilon}_{\mathrm{LT}}$ for the LT creep contribution is given by

$$\dot{\varepsilon}_{\mathrm{LT}} = \frac{A_{\mathrm{LT}} \cdot G \cdot b \cdot D_{\mathrm{c}}}{k_{\mathrm{B}} \cdot T} \cdot \left(\frac{\sigma_{\mathrm{S}}}{G}\right)^{n_{\mathrm{LT}}}. \tag{48}$$

A_{LT} is a microstructure-dependent parameter, n_{LT} is a constant and D_{c} is the dislocation core diffusion coefficient. For Al-based alloys, D_{c} is given by [79]

$$D_{\mathrm{c}} = 0.11 \cdot \exp\left(\frac{Q_{\mathrm{tr}} - Q_{\mathrm{c}}}{R \cdot T}\right) \cdot D_{\mathrm{tr}}, \tag{49}$$

Q_{tr} and Q_{c} are the activation energies for bulk diffusion and dislocation core diffusion and *R* is the universal gas constant.

3.7.2 Power law breakdown

The stress-strain relation typically changes at high stresses (above $10^{-3}G$), which is referred as power law breakdown (PLB). This regime is intensively discussed in [80,81] and only the empirical equation within the present framework is given here as

$$\dot{\varepsilon}_i = \frac{A_i \cdot G \cdot b \cdot D_i}{k_{\mathrm{B}} \cdot T} \cdot \left[\sinh\left(\alpha' \cdot \frac{\sigma_{\mathrm{S}}}{G}\right)\right]^{n_i}. \tag{50}$$

The index 'i' refers to the prevailing deformation mechanisms and α' defines the stress level at which the power law breakdown starts.

3.7.3 Nabarro – Herring creep

Diffusional flow, such as Nabarro-Herring creep and Coble creep, become the dominant deformation process at low applied stresses ($\sigma/G < 10^{-5}$) and small grain sizes. The strain is caused by the diffusion of vacancies instead of the motion of dislocations. Nabarro-Herring

creep was first described, and therefore named by Nabarro and Herring [82]. The corresponding creep rate $\dot{\varepsilon}_{\mathrm{NH}}$, is given by [9]

$$\dot{\varepsilon}_{\mathrm{NH}} = \frac{42 \cdot b^3 \cdot D_{\mathrm{eff}}}{k_{\mathrm{B}} \cdot T \cdot d^2} \cdot \sigma_{\mathrm{S}}. \tag{51}$$

d is the grain size. The effective matrix diffusion coefficient, D_{eff}, is utilized because lattice diffusion is the acting diffusion mechanism.

3.7.4 Coble creep

Coble creep is characterized by vacancy diffusion along grain boundaries instead of lattice diffusion [83]. The strain rate, $\dot{\varepsilon}_{\mathrm{C}}$, is given as

$$\dot{\varepsilon}_{\mathrm{C}} = \frac{42 \cdot b^3 \cdot \pi \cdot \delta \cdot D_{\mathrm{gb}}}{k_{\mathrm{B}} \cdot T \cdot d^3} \cdot \sigma_{\mathrm{S}}, \tag{52}$$

where δ is the effective boundary thickness and D_{gb} is the grain boundary diffusion coefficient, which is given as [84]

$$D_{\mathrm{gb}} = 1.4 \cdot \exp\left(\frac{Q_{\mathrm{tr}} - Q_{\mathrm{gb}}}{R \cdot T}\right) \cdot D_{\mathrm{tr}}. \tag{53}$$

Q_{gb} is the activation energy for grain boundary diffusion.

3.7.5 Harper Dorn creep

Harper et al. reported another deformation mechanism at low stresses and large grain sizes, in 1957 [85]. The Harper–Dorn regime has been identified and discussed in many studies [85–89]. The analysis of the deformation mechanism is beyond the scope of this work, but a phenomenological relation between the creep rate, $\dot{\varepsilon}_{\mathrm{HD}}$, and the applied stress, σ_{s}, is given as

$$\dot{\varepsilon}_{\mathrm{HD}} = \frac{A_{\mathrm{HD}} \cdot D_{\mathrm{eff}} \cdot G \cdot b}{k_{\mathrm{B}} \cdot T} \cdot \left(\frac{\sigma_{\mathrm{s}}}{G}\right), \tag{54}$$

where A_{HD} is a coefficient. $\dot{\varepsilon}_{\mathrm{HD}}$ increases linearly with the applied stress, σ_{s}, (Newtonian nature) and the effective diffusion coefficient D_{eff} indicates that self-diffusion is the dominant diffusion process.

3.7.6 Grain boundary sliding

For small grains, grain boundary sliding (GBS) becomes the dominant deformation mechanism. In [90–94], an inverse dependency of the strain rate, $\dot{\varepsilon}_{\mathrm{GBS}}$, on squared or cubed grain size is assumed. A corresponding phenomenological equation of the creep rate is given as [90]

$$\dot{\varepsilon}_{\mathrm{GBS-GB}} = \frac{A_{\mathrm{GBS-GB}} \cdot D_{\mathrm{gb}} \cdot G \cdot b^4}{k_{\mathrm{B}} \cdot T \cdot d^3} \cdot \left(\frac{\sigma}{G}\right)^2. \tag{55}$$

If the effective lattice diffusion coefficient D_{eff} instead of grain boundary diffusion is the rate-controlling mechanism, the following equation is used [90]

$$\dot{\varepsilon}_{\mathrm{GBS-L}} = \frac{A_{\mathrm{GBS-L}} \cdot D_{\mathrm{eff}} \cdot G \cdot b^3}{k_{\mathrm{B}} \cdot T \cdot d^2} \cdot \left(\frac{\sigma}{G}\right)^2, \tag{56}$$

$A_{\mathrm{GBS-GB}}$ and $A_{\mathrm{GBS-L}}$ are constants. If grain boundary sliding becomes the dominant deformation process, Coble creep and Nabarro-Herring creep can be reduced or even suppressed, as described by Lüthy et al. [90] for Ni. In Al, Coble creep and Nabarro Herring creep are overtaken at all temperatures at an applied normalized stress of $\sigma/G = 10^{-4}$.

4 Integrated model for plastic deformation

4.1 Physical-constitutive computational framework

In the previous subchapters, classical creep relations are reviewed. The correlation between the stress and the strain rate is determined by creep tests, where a constant stress is applied, and the resulting creep rates are measured. At the same time, the creep relations can be used to calculate the stresses at an applied constant true strain rate, as utilized in typical deformation tests. The LT creep, the HT creep, and the Harper–Dorn creep can be rewritten as

$$\sigma_i = \left(\frac{k_\mathrm{B}\cdot T\cdot \dot{\varepsilon}}{A_i\cdot D_i\cdot G\cdot b}\right)^{\frac{1}{n_i}}\cdot G. \tag{57}$$

The indices 'i' express the associated pre-factors, *A*, the diffusion coefficients, *D*, and the exponents *n*. The stress response, resulting from the power law breakdown is

$$\sigma_i = \sinh^{-1}\left(\frac{k_\mathrm{B}\cdot T\cdot \dot{\varepsilon}}{A_i\cdot D_i\cdot G\cdot b}\right)^{\frac{1}{n_i}}\cdot \frac{G}{\alpha'}. \tag{58}$$

By the reformulation of the Equations (51) and (52), Nabarro–Herring creep, σ_NH, and Coble creep, σ_C, are calculated, whereas stresses by D_gb- and D_l-controlled GBS are calculated by Equations (55) and (56). Kreyca [15] shows that the coefficient A_HT is proportional to

$$A_\mathrm{HT} \propto \frac{\Delta F}{D_\mathrm{eff}\cdot\hat{\sigma}}\cdot\exp\left(\frac{-\Delta F}{R\cdot T}\right), \tag{59}$$

Therefore, the creep behavior becomes dependent on the microstructure through the mechanical threshold, $\hat{\sigma}$, and the effective diffusion coefficient D_eff. For a constant applied strain rate, the deformation mechanism which has the lowest deformation resistance determines the overall creep behavior. This behavior is achieved by the summation rule

$$\left(\frac{1}{\sigma_\mathrm{th}}\right)^{n_\mathrm{c}} = \left(\frac{1}{\sigma_\mathrm{G}}\right)^{n_\mathrm{c}} + \left(\frac{1}{\sigma_\mathrm{LT}}\right)^{n_\mathrm{c}} + \left(\frac{1}{\sigma_\mathrm{HT}}\right)^{n_\mathrm{c}} + \left(\frac{1}{\sigma_\mathrm{NH}}\right)^{n_\mathrm{c}} + \left(\frac{1}{\sigma_\mathrm{C}}\right)^{n_\mathrm{c}} + \left(\frac{1}{\sigma_{\mathrm{GBS-GB}}}\right)^{n_\mathrm{c}} + \left(\frac{1}{\sigma_{\mathrm{GBS-L}}}\right)^{n_\mathrm{c}} + \left(\frac{1}{\sigma_\mathrm{HD}}\right)^{n_\mathrm{c}}. \tag{60}$$

n_c is the coupling coefficient. The total stress contribution is given by the sum of the thermal stress contribution σ_th of Equation (60), and the athermal stress contribution, σ_p, of Equation (10).

4.2 Simple MicroStructure Evolution (sMSE)

The objective for the development of the simple MicroStructure Evolution (sMSE) model is to develop models that can be coupled with FE simulations and take microstructure evolution into account. Therefore, minimal calculation times and memory resources are required and microstructure evolution equations, which are described in section 3.5.2, need to be simplified. Complex structures are condensed into a simple system, which contains only two alloying elements (Mg, Si) and one specific precipitation phase, e.g., clusters or the β" phase, but the extension to a multi-phase system is straightforward. No multi-component thermodynamic databases are necessary in the sMSE framework, in contrast to classical precipitation calculations based on, e.g., the CALPHAD method. Besides all the simplifications, the strengthening mechanisms, such as, solute solution strengthening, precipitation strengthening, and work hardening are included. The sMSE framework is successfully included in Abaqus, a standard FEA framework. A typical FEA solution procedure is shown in a flow chart in Figure 7, where T, $\dot{\varepsilon}$ and Δt are the input parameters. Since the temperature gradient, $\dot{T}$, is not provided by all FEA softwares, it is written in brackets.

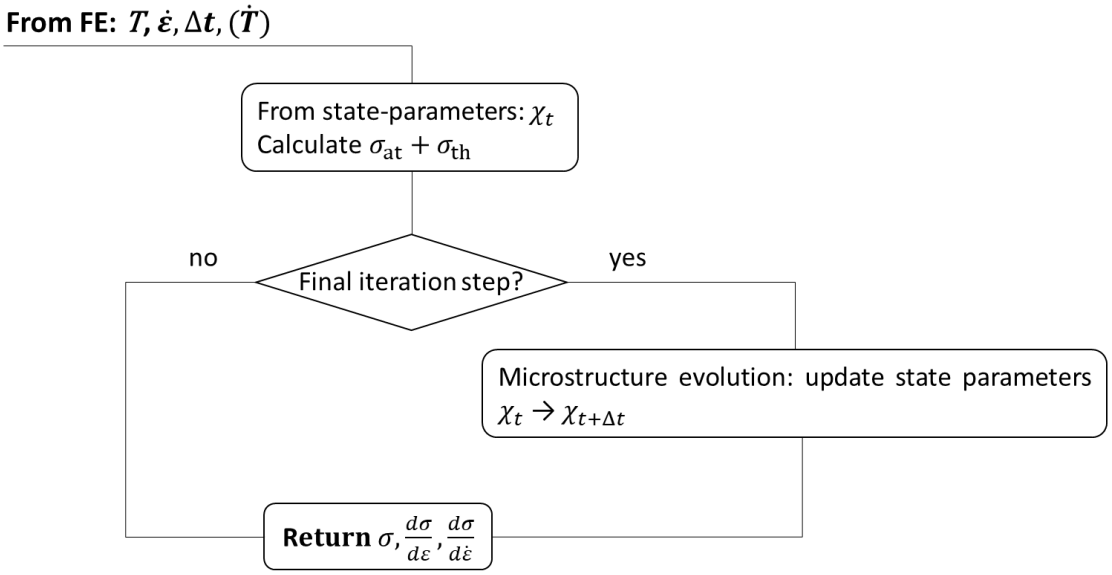

Figure 7. Flow chart of an FEA procedure, indicating the update of the state parameters after the final iteration step *d*t.

A specific microstructure is defined by its state-parameters χ_t, which is directly coupled to the initial athermal stress σ_{ath} and the thermal stress σ_{th}, when a plastic deformation starts. After the final iteration step Δt, the state parameters are updated. The final stress σ and the

derivatives $\frac{d\sigma}{d\varepsilon}$ and $\frac{d\sigma}{d\dot{\varepsilon}}$ are returned every time the materials subroutine is called by the FEA program. A list of all state-dependent variables used in this work is given in Table 1 and assigns all variables to either thermal or athermal stress.

Table 1. Assignment of all state variables to thermally activated σ_{th} and athermal σ_{ath}.

Name	$\boldsymbol{\sigma_{\mathrm{th}}}$	$\boldsymbol{\sigma_{\mathrm{ath}}}$
Mg concentration within the fcc Al matrix $X_{\mathrm{Mg}}^{\mathrm{fcc}}$	x	
Si concentration within the fcc Al matrix $X_{\mathrm{Si}}^{\mathrm{fcc}}$	x	
Current vacancy concentration X_{Va}	x	
Number density of precipitates *N*	x	
Radius of precipitates *r*	x	
Dislocation density ρ		x

To include the precipitate structure in the sMSE framework, the driving force for precipitate nucleation must be determined, as described in section 3.5.2. A driving force exists if the current solute concentration of the alloying elements, such as Mg and Si, exceeds the equilibrium concentration within the Al matrix. The equilibrium concentration is determined by the nominal Mg and Si mole fractions in the system, the stoichiometry of the precipitates and the equilibrium phase fraction of the precipitate, which is calculated by solving the solubility product by numerical methods. The nucleation of new precipitates can be evaluated based on the steady-state nucleation rate, which is given in Equation (16). The calculation of the mean radius, the precipitate growth and the coarsening process is described in detail in [95].

The basic idea of the precipitation hardening model within the sMSE framework is to simplify the most powerful strengthening contribution of the shearing mechanism, which is in general the coherency effect for 6xxx Al alloys, and the Orowan mechanism for non-shearable precipitates. For each state of microstructure, both contributions are calculated separately for all phases, and the mechanism which delivers the least contribution to the total stress, is assumed to be the operative one. To keep the model simple, no distinction between weak and strong precipitates is included. The implemented equations are given in [95].

4.3 Impact of solutes on plasticity

The impact of solutes on the material's properties is manifold. Both, the thermal and the athermal stress contributions, are affected by solutes. Solid solution strengthening, which is based on the Labusch approach in this setup, is included in the mechanical threshold concept, as introduced in section 3.5. Additionally, the energy of the thermal activation ΔF^{lt} of Equation (10) is dependent on the effective concentration, c_{eff}, of the alloying elements, and is given by [96]

$$\Delta F^{\mathrm{lt}} = (k_1 + k_2 \cdot c_{\mathrm{eff}}^{n}) \cdot G b^3. \tag{61}$$

k_1 and k_2 are constants and *n* is a fitting exponent. The effective concentration c_{eff}.is used due to the cross-core diffusion effect, as introduced in 3.5.3.

Since the generation of new mobile dislocations is inversely proportional to the mean free travel distance in the advanced 3IVM, solutes affect the dislocation structure as potential obstacles for moving dislocations. Consequently, also ρ_{im} is influenced by solutes, because dislocation locks are formed by the immobilization of mobile dislocations. As the cross-slip probability can be reduced due to solute additions, the dislocation recovery is affected by solutes as well. This is clearly shown in the experiments and considered in the model calibration.

5 Experimental

In the following subchapters, the experimental setups and selected results are summarized. All results are thoroughly discussed in section 9. Please note that a few parts of this chapter have been taken from the author's journal publications [95] and [97].

5.1 Simple MicroStructure Evolution (sMSE)

For modelling the microstructure evolution of the Al cast alloy of the industrial partner, a huge variety of experiments were conducted to find the optimum set of calibration parameters. However, this thesis focuses on the experiments which were made independently of the mentioned project to demonstrate the general validity and the potential of the state parameter-based sMSE framework. A detailed description of the experiments and the chemical composition of the analyzed commercial AA6082 aluminium alloy is given in [95] and in the Appendix.

For a complete description of the microstructure evolution during various thermo-mechanical treatments, two main aspects need to be addressed: (i) the nucleation and growth kinetics of precipitates during artificial aging, and (ii) the work hardening behavior during deformation tests. Therefore, after a solution heat treatment, the specimens are artificially aged up to 8 h for the first experimental setup (i), and the present precipitates are characterized using a transmission electron microscope (TEM). The evolution of the precipitate microstructure is shown in the bright-field TEM images in Figure 8 for annealing times between 0.5 h and 8 h. A maximum length of approximately 30 nm is measured in the main growth direction after peak aging.

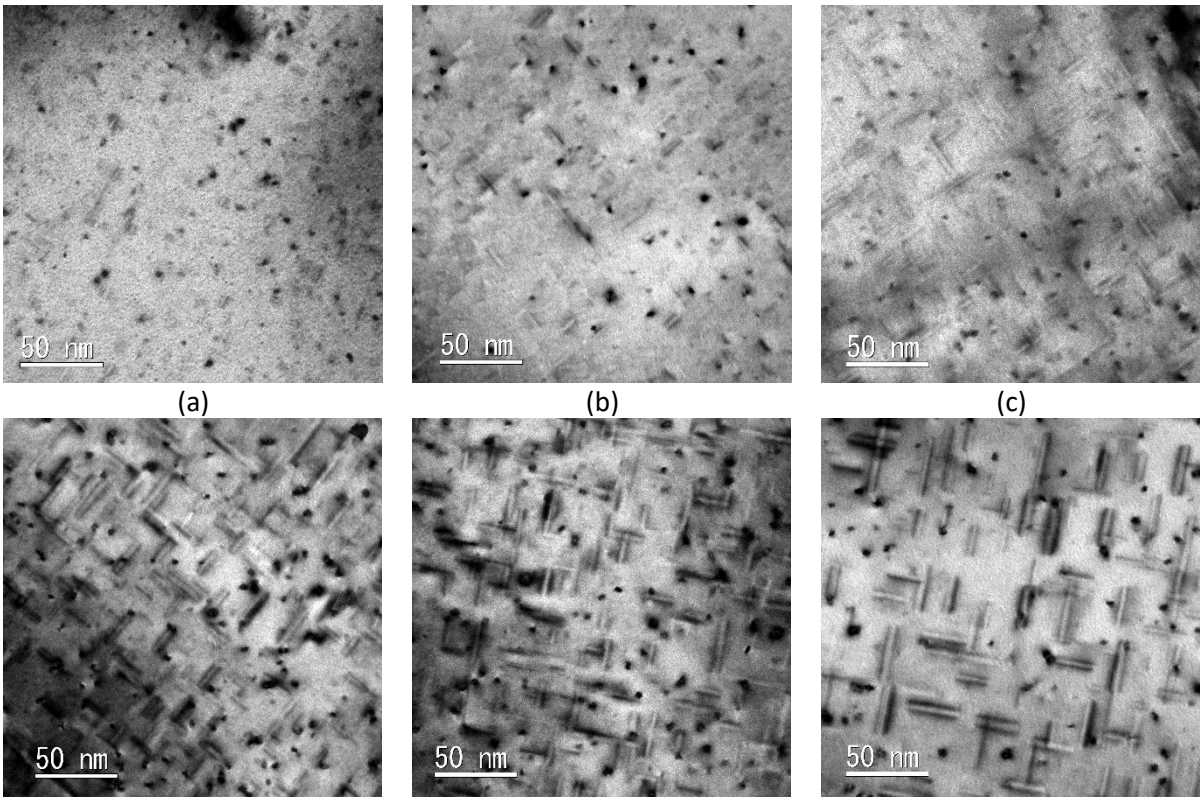

Figure 8. TEM images after annealing at 180 °C for (a) 0.5 h; (b) 1 h; (c) 2 h; (d) 3 h; (e) 4 h and (f) 8 h.

The work hardening behavior is evaluated by compression tests in a high-speed quenching and deformation dilatometer DIL 805 A/D in the second experimental setup (ii). The material is solution heat treated at 530 °C for 5 min and helium-cooled with a cooling rate of 50 K/s to the deformation temperatures (25, 100, 200, 300, 400 and 500 °C). The specimens are held at this temperature for 10 s to achieve sufficient thermal equilibration. Each deformation test is repeated at least twice with applied true strain rates of 0.1 s^{-1} and 1 s^{-1}. A detailed discussion of the flow curves of the compression tests are given in [95], where both, the experimental results as well as the sMSE simulations are shown.

An EMCO-Test M1C 010 unit is used for the Brinell hardness measurements (HBW 1/10), where at least eight measurements are performed for each aging time. Figure 9 shows the Brinell hardness values of the 6081 Al alloy after annealing times between 0.5 h and 336 h at 180 °C. After approximately 8 h, a peak value is reached, before the hardness decreases due to overaging (coarsening) of β'' precipitates and a transformation of β'', which is assumed to be the main hardening phase in the 6xxx series alloys [98] into β'.

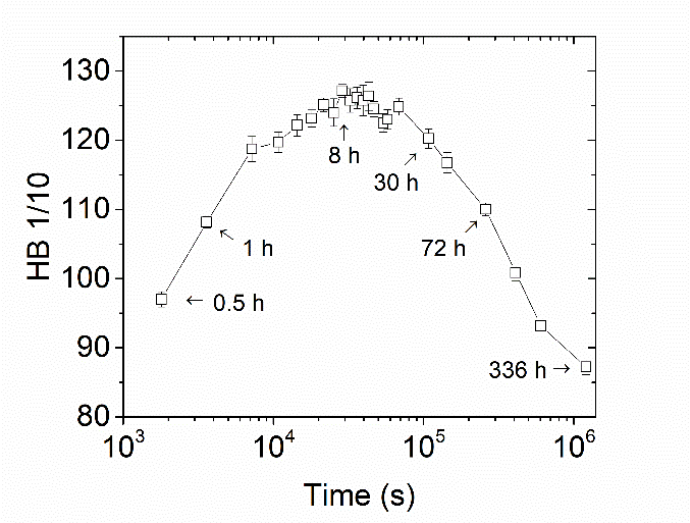

Figure 9. Brinell hardness as a function of aging time at 180 °C.

5.2 Impact of solutes on plasticity

All binary Al-X alloys are cast in an inductive melting furnace using high purity Al 99.999 wt%, Cu 99.99 wt%, Zn 99.99 wt% and Mn 99.99 wt%. The ingots with the highest alloying concentrations are used as master alloys for preparing the more dilute alloys. The following Table 2, Table 3, and Table 4 describe the designation of the alloys and the measured concentrations in weight percent by a wet-chemical analysis.

Table 2. Al-Cu alloys designation and measured concentration in wt%.

	Cu 0.1 %	Cu 0.4 %	Cu 0.8 %	Cu 1.6 %
Cu (%)	0.13	0.44	0.86	1.56

Table 3. Al-Zn alloys designation and measured concentration in wt%.

	Zn 0.4 %	Zn 0.8 %	Zn 2 %	Zn 4 %
Zn (%)	0.46	0.94	2.17	4.81

Table 4. Al-Mn alloys designation and measured concentration in wt%.

	Mn 0.1 %	Mn 0.2 %	Mn 0.4 %	Mn 0.8 %
Mn (%)	0.11	0.23	0.43	0.82

The processing of the cylindrical specimens for the deformation tests follows the same procedure for all binary alloys: casting, homogenization, extrusion, additional heat treatment, and mechanical sample preparation. All heat treatments are carried out in a circulating air furnace (Carbolite Type 3508). The ingots are homogenized in the following way: Al-Cu – 480 °C for 6 h; Al-Zn - 530 °C for 5 h; Al-Mn - 630 °C for 5 h. The homogenization temperatures are chosen to ensure a solid solution of the alloying elements within the Al matrix. The ingots are quenched in water to prevent the nucleation of precipitates. These quenching rates are high enough to avoid the formation of precipitates at these low alloying concentrations, as reported in [61,97,98]. To get rid of the casting microstructure, the ingots are extruded to a final diameter of 10 mm before additional heat treatment (Al-Cu - 530 °C for 1 h; Al-Zn - 530 °C for 1 h; Al-Mn - 630 °C for 1 h), ensuring homogeneous and large grain sizes. Since this work focuses on the influence of solutes on both, the yield stress and the work hardening behavior, hardening due to fine grains is thus excluded. Finally, cylindrical specimens with a diameter of 5 mm and a length of 10 mm are fabricated.

The compression tests to obtain the flow curves are performed on a dilatometer DIL 805 A/D. Prior to the deformation step, the specimens are solution heat treated at 530 °C for 5 min and helium-cooled with a cooling rate of 50 K/s to room temperature. Each deformation test is repeated at least twice with applied true strain rates of 0.001 s^{-1}, 0.01 s^{-1}, 0.1 s^{-1} and 1 s^{-1}.

To analyze the influence of solutes on the plastic deformation behavior, the yield stress $Rp_{0.2}$ and the initial hardening rate θ_0, which is the slope of the stress-strain curve at the yield point, are utilized. For a schematic illustration of θ_0, see, e.g., Kreyca and Kozeschnik [33]. Attention should be drawn to the fact that the evaluation of θ_0 is very sensitive to the applied data evaluation criteria and to the nature of the data in general. Still, this analysis delivers a trend, which can provide valuable insight into the dislocation evolution behavior.

In the following, the results of the Al-Cu experiments are shown exemplarily, whereas all the other results are given in [97] and in section 9, where the MatCalc simulations are also included. Figure 10 (a) and (b) show the initial hardening rates θ_0 and the yield stresses as a function of the solute content and the strain rates. The results for pure Al are included to provide a baseline for better illustrating the influence of alloying elements on mechanical properties.

The higher the amount of dissolved Cu within the Al matrix, the higher is the initial hardening rate θ_0, as indicated in Figure 10 (a). However, θ_0 slightly decreases with an increasing strain

rate, as shown in Figure 10 (b), which is different from the effects of Mn and the dependency in pure Al.

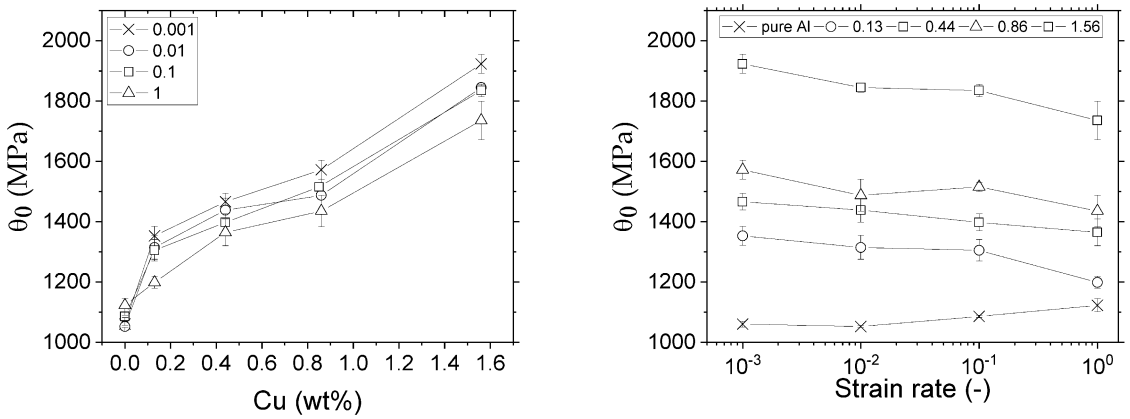

(a) (b)

Figure 10. Initial hardening rate θ_0 as a function of (a) the concentration of Cu and (b) the true strain rate.

The yield stress increases with an increasing amount of Cu, whereas no clear trend is observed as a function of the strain rate, as shown in Figure 11.

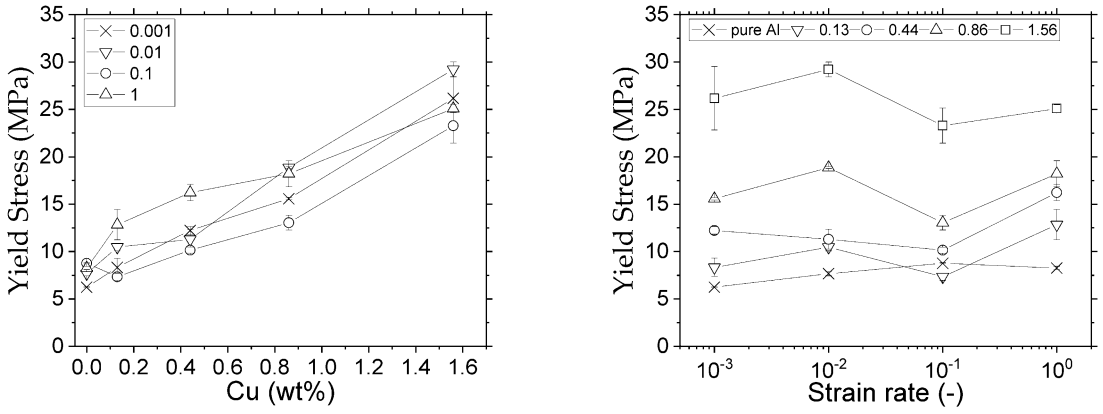

(a) (b)

Figure 11. Yield stress as a function of (a) the concentration of Cu and (b) the true strain rate.

6 Simulation

In the following subchapters, the simulations are summarized. All results are thoroughly discussed in section 9. Please note that a few parts of this chapter have been taken from the author's journal publications [75,95,97].

6.1 Physical-constitutive computational framework

In this chapter, the models presented are verified by creep relations from literature, microstructure analyses and mechanical tests.

All simulation input parameters of the stress-strain relations of the Harper–Dorn creep (HD), the power law creep (PL) and the power law breakdown (PLB) regime at higher stresses are listed in [75], where additional simulations are published and interpreted by the author. Exemplary stress strain relations in Figure 12 illustrate a linear relation in a double-logarithmic plot for each creep regime, until the power law breakdown is reached at high stresses. Each line represents a specific deformation mechanism, whereas the bold red line, which is labeled 'DYN', is the total stress response on an applied strain rate according to Equation (60). The initial grain size is assumed to be 5 µm and the temperatures vary between 100 °C to 500 °C. Figure 12 indicates that the lowest resulting stress at a constant strain rate is decisive for the deformation mechanism. The slopes of the creep regimes are determined by the exponent n_i in Equation (57), until the PLB becomes dominant. For all simulated temperatures, Coble creep is the dominant mechanism at small stresses and strain rates. At 100 °C, 200 °C and 300 °C, grain boundary diffusion-controlled GBS is dominant at intermediate stress values, and lattice diffusion-controlled GBS takes over at 400 °C and 500 °C. Therefore, GBS separates the diffusional flow and the power law creep range, which is in good agreement with literature [101]. At high stresses, dislocation glide (at 100 °C) or high temperature creep (T> 100 °C) takes over. The exponent n_c in Equation (60) defines how distinct the transition of the deformation mechanisms is – the higher the exponent, the closer is the resulting stress, σ_{ges}, to the prevailing mechanism. The mechanical threshold is treated as a constant since no precipitation processes occur in this setup.

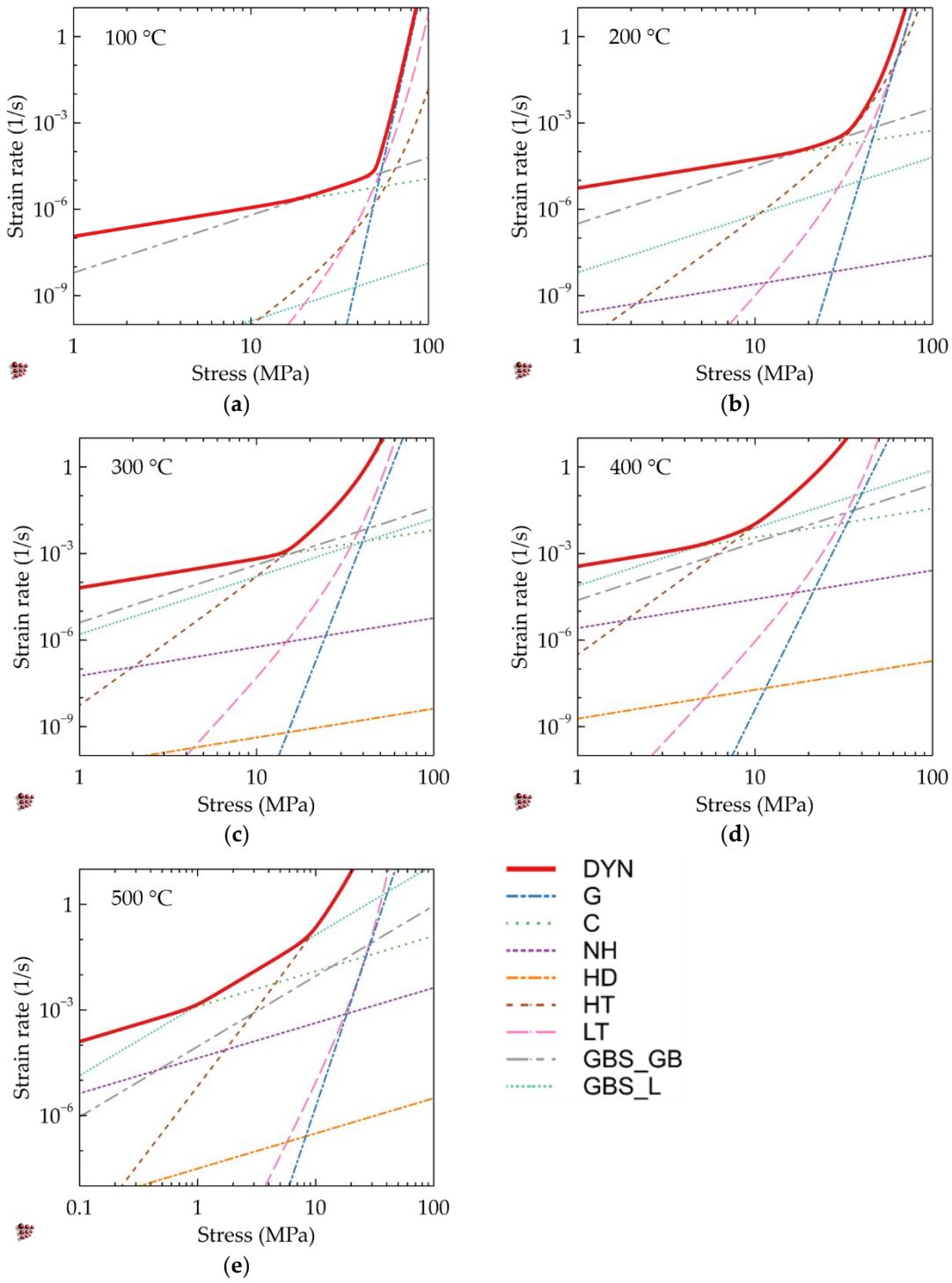

Figure 12. Dislocation glide (G), LT creep (LT), HT creep (HT), Nabarro–Herring creep (NH), Coble creep (C), Harper–Dorn creep (HD), and D_{gb}- and D_l-controlled GBS (GBS_GB and GBS_L) at different constant strain rates at (a) 100 °C; (b) 200 °C; (c) 300 °C; (d) 400 °C and (e) 500 °C. The resulting stress, σ_{ges}, of Equation (60) is displayed as bold line (DYN). Reproduced from [75].

6.1.1 Stress relaxation

Besides calculating stresses at an applied constant strain rate, the framework allows to calculate time-dependent stress relaxation. The stress strain relations are then used in an inverse methodology as derived in [75].

To validate this framework, experimental relaxation tests are used from Falkinger and Simon [102]. In their work, cylindrical specimens of an AlMg4.5Mn alloy were first compressed with a constant strain rate of 0.01 (1/s) at different temperatures (350 °C, 400 °C, 450 °C, 500 °C) and then immediately stress relaxed, as shown in Figure 13 (a). Figure 13 (b) shows the time-dependent reduction of the strain rate, starting from 0.01 (1/s). Lower strain rates at higher temperatures are based on the lower initial stress level at the start of the relaxation step. Figure 13 (c) and Figure 13 (d) show the stress relaxation of the HT creep (HT), the LT creep (LT), the Coble creep, lattice diffusion controlled GBS as well as grain boundary diffusion-controlled GBS at 350 °C and 500 °C. ”DYN” represents the total thermal stress contribution, σ_{ges}. The athermal stress contribution can be neglected at high temperatures. The calibration settings are summarized in [75]. At the start of stress relaxation, HT creep is the dominant mechanism, whereas lattice diffusion-controlled GBS takes over after the strain rate rapidly decreases. At very low strain rates, Coble creep takes over at 500 °C.

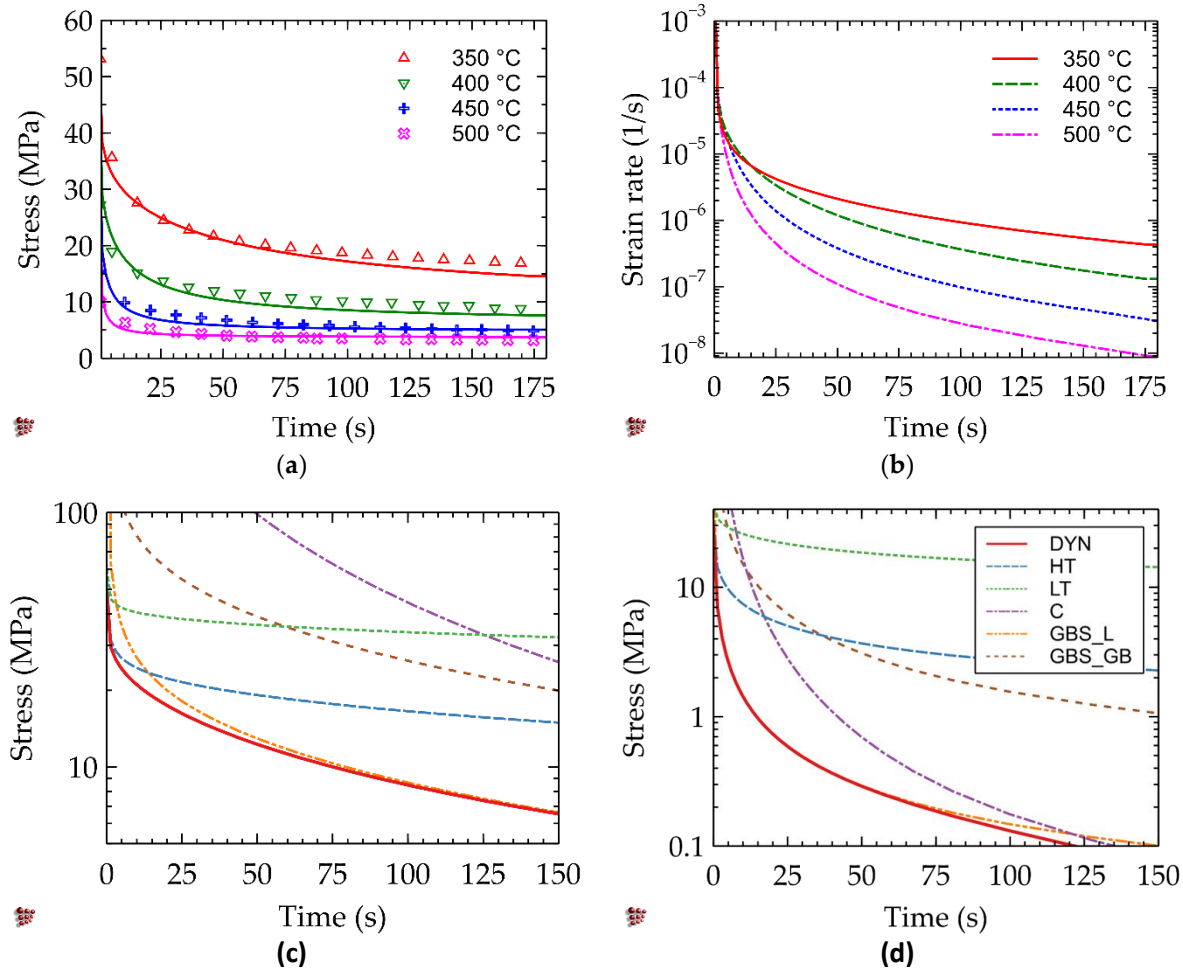

Figure 13. (a) Relaxation tests of an AlMg4.5Mn aluminium alloy at different temperatures. The solid lines are the simulations, whereas the symbols indicate the experimental results from [102]; (b) logarithmic strain rate reduction; logarithmic stress calculations of HT creep (HT), LT creep (LT), Coble creep, D_{gb}- and D_l-controlled GBS and the total thermal stress contribution (DYN) (c) at 350 °C and (d) at 500 °C.

6.1.2 Deformation maps

This framework allows the construction of deformation maps, as shown exemplarily in Figure 14 for a grain size of (a) 5 µm and (b) 50 µm. Although these figures are generated without explicit calibration, a qualitative analysis is valid. Each number corresponds to a specific deformation mechanism, while the bold black line indicates the transitions between them.

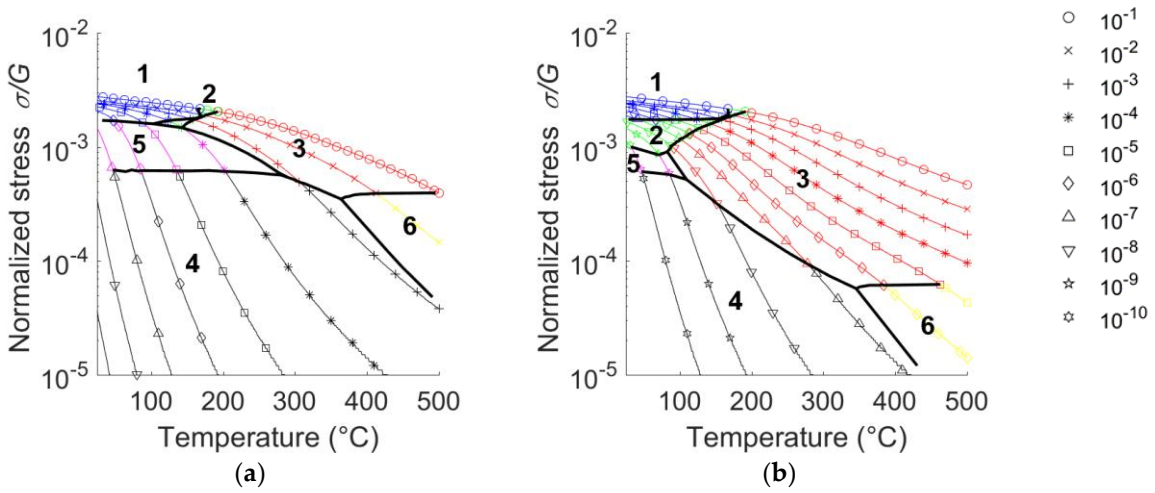

Figure 14. Exemplary deformation maps for pure Al. Normalized stress [-] for different temperatures and strain rates for (a) 5 µm and (b) 50 µm. The black, bold lines indicate transitions between the deformation regimes. The numbers indicate the dominant deformation mechanisms: dislocation glide (1); LT creep (2); HT creep (3); Coble creep (4); D_{gb}-controlled GBS (5) and D_l-controlled GBS (6).

A detailed discussion of these deformation maps is reported in [75].

6.2 Simple MicroStructure Evolution (sMSE)

The simple MicroStructure Evolution (sMSE) model has been developed to couple rather complex microstructure evolution models in a condensed form with FE-simulations. Although these models are strongly simplified, the following subchapters highlight that the simulations agree well with the experimental results for both, the evolution of precipitates and the mechanical properties.

6.2.1 Precipitation evolution

The analysis of the nucleation and growth kinetics of precipitates play a crucial role in evaluating the microstructure evolution of 6xxx series alloys. Experimental tests were carried out to calibrate the sMSE framework on the one hand, and to test the reliability of the model on the other hand. The heat treatment of the specimens is shown in Figure 15 (a), where the starting point of the annealing step is illustrated by the dotted, vertical lines in Figure 15 (a-d). The symbols indicate the experimental results of the number density (Figure 15b), the length (Figure 15c) and the phase fraction of the precipitates (Figure 15d), whereas the number density *N* is calculated from [98]. While the experimentally evaluated number density

starts to increase after two hours, an almost constant precipitation microstructure immediately appears in the sMSE simulation, when the annealing temperature is reached at 180 °C. To compare the radius of the spherical precipitation of the sMSE model to the measured length of the needle-shaped β'', the following conversion is used

$$l = \sqrt[3]{\frac{16}{3} r^3 h^2}, \tag{62}$$

where *h* is the shape parameter [95]. Although simplified precipitation kinetic models are used in the sMSE framework, the simulated phase fractions and the lengths of the precipitates are in good agreement with the measured values, as shown in Figure 15 (c) and Figure 15 (d). All simulations have been carried out with one set of parameters, as described in [95].

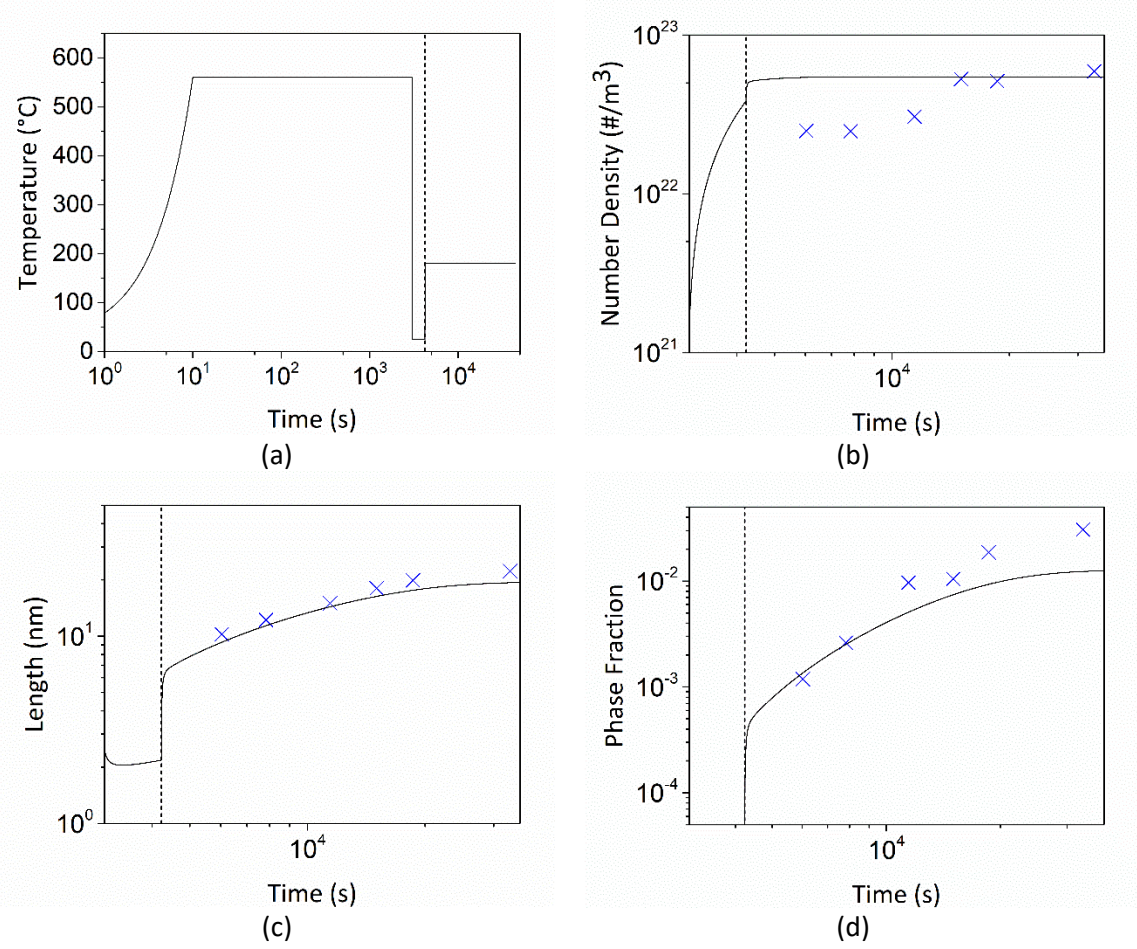

Figure 15. (a) The applied heat treatment; (b) number density; (c) length and (d) phase fraction. Solid lines represent simulation results, while symbols indicate experimental results.

6.2.2 Deformation tests

As the motivation for developing the sMSE framework was to calculate internal stresses using the FEM mesh, an accurate simulation of the yield strength is required. It should be highlighted here that even with a condensed form of the strengthening mechanisms within the sMSE framework, a very good agreement between the simulations and the experiments can be achieved. This applies for the athermal stress contribution, as well as for the thermal stress contribution, which determines the yield strength. A comparison of the experimental results of the yield stress and the results of the simulation for strain rates of 0.1 s^{-1} and 1 s^{-1} and six different temperatures is visualized in Figure 16.

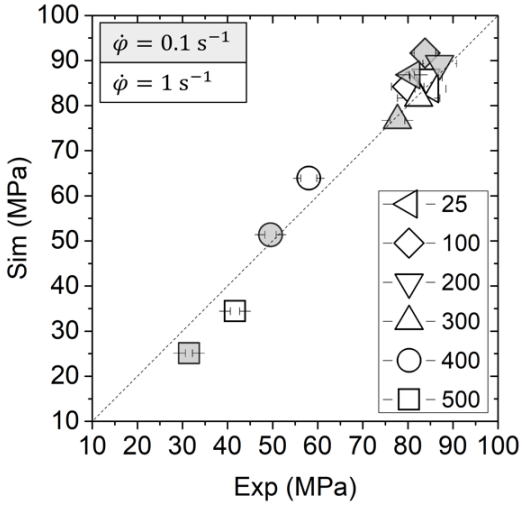

Figure 16. Comparison of simulated and experimentally obtained flow stresses at strain of 0.1 s^{-1} and 1 s^{-1} and six different temperatures.

6.3 Impact of solutes on plasticity

The calibration parameters for the strengthening models are listed in Table 5, for pure Al as well as the Al-X (X = Mn, Cu, Zn) alloys. The input parameters used for simulating the thermal stress contribution are marked with 'Th.', whereas the input parameters for the athermal stress contribution are marked with 'Ath.'. Although not all parameters are defined here, but in [97], this table illustrates that the respective parameters for the thermal stress contribution are all constants, since the strain rate and concentration dependence are already taken into account by the physically-based models themselves.

Table 5. Input parameters for the strengthening models as described in *[97]*. The input parameters used for simulating the thermal stress contribution are marked with 'Th.', whereas the input parameters for the athermal stress contribution are marked with 'Ath.'.

		Pure Al	**Mn**	**Cu**	**Zn**
σ_{basic}	Th.	18 MPa			
k_1		0.1			
k_2		0	0.55	0.8	0.3
n		1/3			
n_{ss}		1.8			
ε_{m}		0	0.042	0.0194	0.0038
A_{m}	Ath.	$-0.22\cdot \ln(\dot{\varepsilon}) + 33.75$			
β_{ss}		0	$202.17\cdot c^{1.80}$	$2.62\cdot \dot{\varepsilon}^{-0.064} c$	$0.0046\cdot c^{0.11}$
β_{w}		750			
β_{G}		0.08			
A_{w}		$-0.07\cdot \ln(\dot{\varepsilon}) + 0.68$			
A_{im}		$-(1.3\cdot 10^{-4})\cdot \ln(\dot{\varepsilon}) + 0.85$			
B_{m}		$-0.564\cdot \ln(\dot{\varepsilon}) + 8.94$	$B_{\mathrm{m,Al}}$	$B_{\mathrm{m,Al}} - 27.2\cdot \dot{\varepsilon}^{-0.14} c^{0.52}$	$B_{\mathrm{m,Al}} - 0.78\cdot \dot{\varepsilon}^{-0.3} \cdot c^{0.24}$
B_{im}		$0.03\cdot \ln(\dot{\varepsilon}) + 0.9$	$B_{\mathrm{im,Al}}$	$B_{\mathrm{im,Al}}$	$B_{\mathrm{im,Al}}$
C_{m}		0.2			
C_{im}		0.2			
C_{w}		0.2			

6.3.1 Dislocation density evolution

For calibrating the dislocation density evolution, the so-called Kocks-Mecking (KM) plot, which links the strain hardening rate with the stress, gives a good indication of the dislocation recovery behavior. Stronger dynamic recovery effects typically cause a steeper slope of the KM-plot and, therefore, affect the parameter B_{m} in Table 5. The higher the Cu concentration for instance, the lower is the dynamic recovery effect and B_{m} is reduced. In contrast, similar slopes of Figure 17 suggest similar recovery conditions independent of the Mn concentrations, although they start from different θ_0 values.

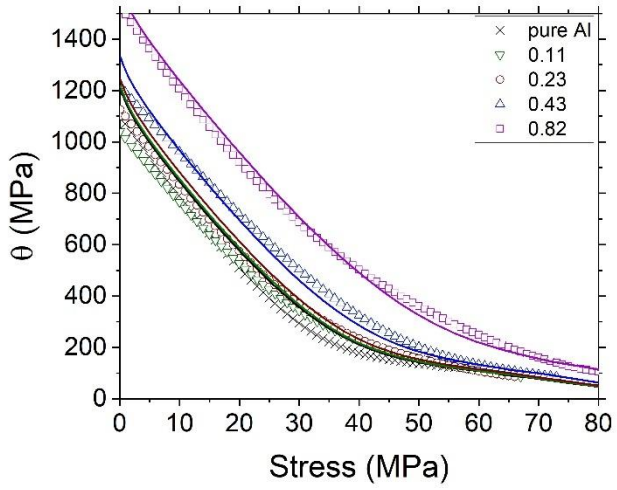

Figure 17. Kocks-Mecking plot of various binary Al-Mn alloys at a strain rate of 0.1 s^{-1}. Solid lines represent the simulations while symbols indicate the experimental results.

The parameters C_{m}, C_{im} and C_{w} take climbing of mobile, immobile and wall dislocations into account and can be treated as constant for the deformation tests at room temperature. It should be noted that this approach does not claim to be a comprehensive representation of all occurring physical mechanisms, but it represents a consistent way to describe the dislocation density evolution and successfully simulate a variety of flow curves with a single set of parameters.

Figure 18 shows the calculated evolution of the mobile dislocation density, ρ_{m}, the wall dislocation density, ρ_{w}, the immobile dislocation density, ρ_{im} and a weighted sum, ρ_{tot}, during deformation at RT with a true strain rate of 0.001 s^{-1} for (a) pure Al and (b) binary Al-Cu (1.6 wt%). The simulated dislocation density ρ_{tot} agrees reasonably with the obtained dislocation densities from [103], which are also included in Figure 18 (a). In the early stages of deformation, the total dislocation density is mainly controlled by the generation of mobile dislocations. With increasing mobile dislocation density, the transformation into locks and dipoles gains relevance and, in addition to the mobile dislocation annihilation process, leads to a saturation of the mobile dislocation density. Only the formation and the annihilation of the mobile dislocations are directly affected by the alloying elements, as defined by β_{ss} and B_{m} in Table 5. With an increasing amount of Cu, more mobile dislocations are generated, leading to a higher saturation level, as demonstrated in Figure 18 (b). Since immobile and wall

dislocations arise from mobile dislocations, these dislocation densities are indirectly concentration-dependent as well.

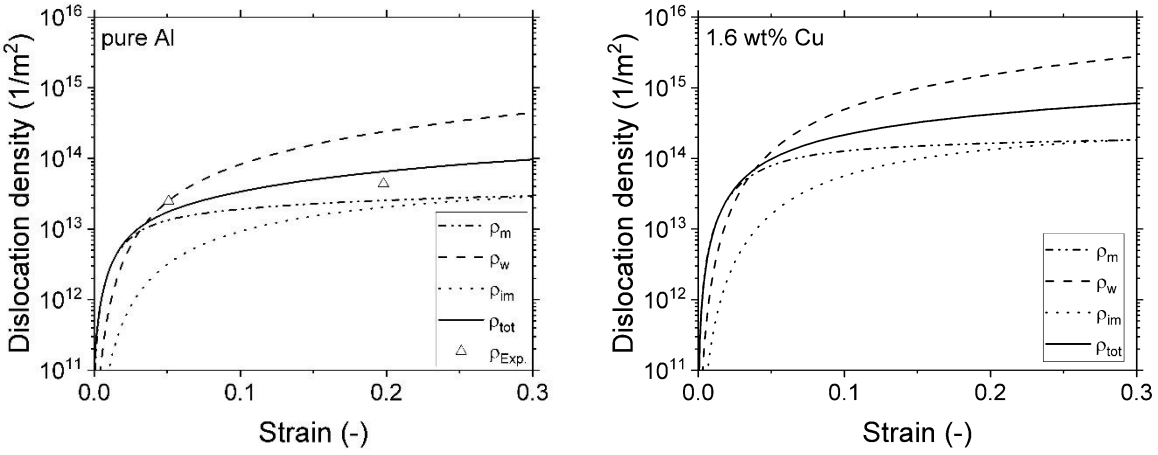

Figure 18. Calculated dislocation density evolution at RT and a strain rate of 0.001 s^{-1} for (a) pure Al and (b) Al-Cu (1.6 wt%). Experimental points from *[104]*.

It should be mentioned that no direct experimental evidence has been provided to confirm the development of the different dislocation structures as shown in Figure 18. However, the evolution of the total dislocation density ρ_{tot}, which is linked to the athermal stress contribution by the Taylor equation, provides valuable information of the material's work hardening behavior.

6.3.2 **Flow curve simulations**

The input parameters for all flow curve simulations are listed in [97]. The solid lines in Figure ***19*Figure *19.*** Flow curves of binary Al-Cu at strain rates of (a) 0.001, (b) 1 s-1. represent the simulations and the symbols indicate the experimental results. The plastic deformation behavior is given by the sum of the thermal and athermal stress contribution, as discussed in section 3. The thermal part determines the initial yield stress of each flow curve and is calculated by the superposition of the basic stress and solid solution strengthening. Due to thermal activation, the measured yield stress can be lower than the basic stress, as expressed in Equation (10). Especially for high strain rates ($\dot{\varphi}$ = 0.1 and $\dot{\varphi}$ = 1 s^{-1}) and high concentrations, a trend of increasing hardening rate θ can be observed in the experimental data.

Figure 19 shows the flow curves of the binary Al-Cu alloys for strain rates of 0.001 s^{-1} and 1 s^{-1}. The concentration-dependency of the work hardening rate is determined by the influence of the dissolved atoms on the internal and wall dislocation density. An increasing Cu amount lowers the effective mean free travel distance of mobile dislocations and decreases B_{m}, as indicated by the calibrations in Table 5. Consequently, more mobile dislocations are formed, and less annihilation occurs at the same time, leading to a higher athermal stress contribution. The model calibration of β_{ss} and A_{m} suggest a negative strain rate sensitivity of the initial strengthening rate θ_0, as observed in the experiments. A slightly increasing dynamic recovery effect with increasing strain rate is given by the strain rate dependency of B_{m}. This can be observed if Figure 19 (a) and (b) are compared at 1.56 wt% Cu. Although, the flow curve has a higher initial yield stress at a strain rate of 1 s^{-1}, the evaluated stress at a strain of 0.3 is less compared to the curve at a strain rate of 0.001 s^{-1}.

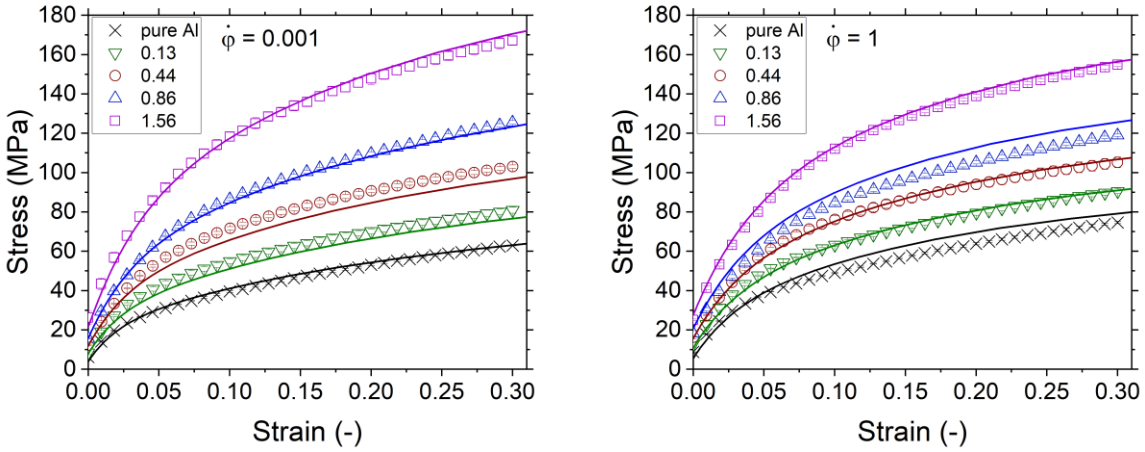

Figure 19. Flow curves of binary Al-Cu at strain rates of (a) 0.001, (b) 1 s^{-1}.

7 Summary

The plastic deformation behavior of various Al alloys is simulated in a wide temperature and strain rate range. Therefore, physically based models, which include thermal and athermal stress contributions, are combined with empirical creep relations. For all simulations, the effective diffusion coefficient, which is influenced by pipe diffusion enhancement, excess vacancies or trapping effects, is used. This new framework is brought into a condensed form so that it can be integrated in standard FEA tools, such as Abaqus, and is called 'simple MicroStructure Evolution' (sMSE) model in this work. Despite all simplifications, main strengthening mechanisms, such as precipitation strengthening, solid solution strengthening, or work hardening are included, and its validity is demonstrated. The sMSE framework is characterized by a low calculation time, which allows to simulate residual stresses of complex components, such as cylinder heads. Because of the consideration of the microstructure evolution across a broad range of temperatures and strain rates, this framework is suitable for various industrial applications, including hot forming processes and strain relaxation during stress relieve annealing. Furthermore, exemplary deformation maps for Al are calculated in this work to provide an overview of the dominant deformation mechanism at specific temperatures and applied shear stresses.

Another focus of this work is the investigation of the impact of solutes on the mechanical properties. Therefore, a comprehensive experimental study of the influence of dissolved alloying elements on the yield strength as well as the work hardening behavior is given for various binary Al-Mn, Al-Zn and Al-Cu alloys. For the simulation of the yield stress, a mechanical threshold concept is used, whereas the work hardening simulation is based on an advanced 3-Internal-Variables-Model (3IVM). The evolution of mobile, immobile and wall dislocations is calculated, where a suitable evaluation of the experiments can provide information about the materials hardening and recovery behavior, which is the basis of a valid model calibration.

8 References

1. Taylor, G.I. Plastic Strain in Metals. *Journal of the institute of metals* **1938**, *62*, 307–324.
2. Kocks, U.F. The Relation between Polycrystal Deformation and Single-Crystal Deformation. *Metallurgical and Materials Transactions* **1970**, *1*, 1121–1143.
3. Hansen, N.; Huang, X. Microstructure and Flow Stress of Polycrystals and Single Crystals. *Acta Mater* **1998**, *46*, 1827–1836.
4. Canova, G.R.; Kocks, U.F.; Jonas, J.J. Theory of Torsion Texture Development. *Acta Metallurgica* **1984**, *32*, 211–226.
5. Diehl, J.; Mader, S.; Seeger, A. Gleitmechanismus Und Oberflächenerscheinungen Bei Kubisch Flächenzentrierten Metallen. **1955**, *46*, 650–657.
6. Reinstaluminium, A. Zugverformung von Kupfer-Einkristallen 1. Verfestigungskurven Und Oberflächenerscheinungen. *Zeitschrift für Metallkunde* **1956**, *47*, 331–343.
7. Estrin, Y. Dislocation-Density-Related Constitutive Modeling. In *Unified Constitutive Laws of Plastic Deformation*; Krausz, A. S., Krausz, K., Eds.; Academic Press, Inc.: San Diego, 1996; pp 69–106.
8. Estrin, Y.; Tóth, L.S.; Molinari, A.; Bréchet, Y. A Dislocation-Based Model for All Hardening Stages in Large Strain Deformation. *Acta Mater* **1998**, *46*, 5509–5522.
9. Frost, H.J.; Ashby, M.F. *Deformation-Mechanism Maps, The Plasticity and Creep of Metals and Ceramics*, 1st ed.; Pergamon Press: Oxford, 1982.
10. Ludwik, P. Über Den Einfluss Der Deformationsgeschwindigkeit Bei Bleibenden Deformationen Mit Besonderer Berücksichtigung Der Nachwirkungserscheinungen. *Physikalische Zeitschrift* **1909**, *Nr.12*, 411–417.
11. Voce, E. A Practical Strain Hardening Function. *Metallurgia* **1955**, *51*, 219–226.
12. Johnson, G.R.; Cook, W.H. A Constitutive Model and Data for Metals Subjected to Large Strains, High Strain Rates and High Temperatures. *Proceedings of the Seventh International Symposium on Ballistic* **1983**, 541–547.
13. Zerilli, F.J.; Armstrong, R.W. Dislocation-Mechanics-Based Constitutive Relations for Material Dynamics Calculations. *J Appl Phys* **1987**, *61*, 1816–1825.
14. Huang, S.; Khan, A.S. Huang S., Khan A. S. Modelling the Mechanical Behavior of 1100-0 Aluminum at Different Strain Rates by the Bodner-Partom Model.Pdf. *Int J Plast* **1992**, *8*, 501–517.
15. Kreyca, F.J. State Parameter Based Modelling of Stress- Strain Curves in Aluminium Alloys, TU Wien, 2017.
16. Kocks, U.F. Laws for Work-Hardening and Low-Temperature Creep. *J Eng Mater Technol* **1976**, *98*, 76–85.
17. Estrin, Y.; Mecking, H. On the “Threshold Stress” for Creep of Particle-Strengthened Materials. *Scripta Metallurgica* **1985**, *19*, 451–455.

18. Kubin, L.P.; Estrin, Y. EVOLUTION OF DISLOCATION DENSITIES AND PORTEVIN-LE CHATELIER EFFECT. **1990**, *38*, 697–708.

19. Estrin, Y. Dislocation Theory Based Constitutive Modelling: Foundations and Applications. *J Mater Process Technol* **1998**, *80*, 33–39.

20. Roters, F.; Raabe, D.; Gottstein, G. Work Hardening in Heterogeneous Alloys-A Microstructural Approach Based on Three Internal State Variables.Pdf. 2000.

21. Nes, E. Modelling of Work Hardening and Stress Saturation in FCC Metals. *Prog Mater Sci* **1997**, *41*, 129–193.

22. Marthinsen, K.; Nes, E. Modelling Strain Hardening and Steady State Deformation of Al – Mg Alloys Modelling Strain Hardening and Steady State Deformation of Al – Mg Alloys. *Materials Science and Technology* **2001**, No. 17:4, 376–388.

23. Barlat, F.; Glazov, M.V.; Brem, J.C.; D.J., L. A Simple Model for Dislocation Behavior Strain and Strain Rate Hardening Evolution in Deforming Aluminum Alloys. *Journal of Plasticity* **2000**, 919–939.

24. Tóth, L.S.; Molinari, A.; Estrin, Y. Strain Hardening at Large Strains as Predicted by Dislocation Based Polycrystal Plasticity Model. *Journal of Engineering Materials and Technology, Transactions of the ASME* **2002**, *124*, 71–77.

25. Beyerlein, I.J.; Tome, C.N. A Dislocation-Based Constitutive Law for Pure Zr Including Temperature Effects. **2008**, *24*, 867–895.

26. Austin, R.A.; Mcdowell, D.L. A Dislocation-Based Constitutive Model for Viscoplastic Deformation of Fcc Metals at Very High Strain Rates. *Int J Plast* **2011**, *27*, 1–24.

27. Fan, X.G.; Yang, H. Internal-State-Variable Based Self-Consistent Constitutive Modeling for Hot Working of Two-Phase Titanium Alloys Coupling Microstructure Evolution. *Int J Plast* **2011**, *27*, 1833–1852.

28. Gao, C.Y.; Zhang, L.C. Constitutive Modelling of Plasticity of Fcc Metals under Extremely High Strain Rates. *Int J Plast* **2012**, *32–33*, 121–133.

29. Galindo-Nava, E.I.; Sietsma, J.; Rivera-Díaz-Del-Castillo, P.E.J. Dislocation Annihilation in Plastic Deformation: II. Kocks-Mecking Analysis. *Acta Mater* **2012**, *60*, 2615–2624.

30. Hansen, B.L.; Beyerlein, I.J.; Bronkhorst, C.A.; Cerreta, E.K. A Dislocation-Based Multi-Rate Single Crystal Plasticity Model. *Int J Plast* **2013**, *44*, 129–146.

31. Bertin, N.; Capolungo, L.; Beyerlein, I.J. Hybrid Dislocation Dynamics Based Strain Hardening Constitutive Model. *Int J Plast* **2013**, *49*, 119–144.

32. Li, D.; Zbib, H.; Sun, X.; Khaleel, M. Predicting Plastic Flow and Irradiation Hardening of Iron Single Crystal with Mechanism-Based Continuum Dislocation Dynamics. *Int J Plast* **2014**, *52*, 3–17.

33. Kreyca, J.; Kozeschnik, E. State Parameter-Based Constitutive Modelling of Stress Strain Curves in Al-Mg Solid Solutions. *Int J Plast* **2018**, *103*, 67–80.

34. Orowan, E. Problems of Plastic Gliding. *Proceedings of the Physical Society* **1940**, *52*, 8–22.

35. Goerdeler, M. *Application of a Dislocation Density Based Flow Stress Model in the Integrative Through-Process Modelling of Aluminium Production*; Shaker Verlag: Aachen, 2007.

36. Haasen, P. Dislocations in Solids. In *Solution hardening in f.c.c metals*; Nabarro, F. R. N., Ed.; North Holland, 1979; pp 156–189.

37. Friedel, J. *Les Dislocations*; Gauthier-Villars, Paris, 1956.

38. Fleischer, R.L. Substitutional Solution Hardening. *Acta Metallurgica* **1963**, *11*, 203–209.

39. Mott, N.F.; Nabarro, F.R.N. *Dislocation Theory and Transient Creep*; 1948.

40. Labusch, R. A Statistical Theory of Solid Solution Hardening. *Phys. Stat. Sol.* **1970**, *41*, 659–669.

41. Hull, D.; Bacon, D.J. *Introduction to Dislocations*, Fifth Edit.; Elsevier Ltd, 2011.

42. Haasen, P. Mechanical Properties of Solid Solutions. In *Physical Metallurgy*; 1996; pp 2010–2073.

43. Leyson, G.P.M.; Curtin, W.A. Friedel vs. Labusch: The Strong/Weak Pinning Transition in Solute Strengthened Metals. *Philosophical Magazine* **2013**, *93*, 2428–2444.

44. Leyson, G.P.M.; Curtin, W.A. Friedel vs. Labusch: The Strong/Weak Pinning Transition in Solute Strengthened Metals. *Philosophical Magazine* **2013**, *93*, 2428–2444.

45. Svoboda, J.; Fischer, F.D.; Fratzl, P.; Kozeschnik, E. Modelling of Kinetics in Multi-Component Multi-Phase Systems with Spherical Precipitates I: Theory. *Materials Science and Engineering A* **2004**, *385*, 166–174.

46. Kozeschnik, E.; Svoboda, J.; Fratzl, P.; Fischer, F.D. Modelling of Kinetics in Multi-Component Multi-Phase Systems with Spherical Precipitates II: Numerical Solution and Application. *Materials Science and Engineering A* **2004**, *385*, 157–165.

47. Kozeschnik, E.; Svoboda, J.; Fischer, F.D. Modified Evolution Equations for the Precipitation Kinetics of Complex Phases in Multi-Component Systems. *CALPHAD* **2004**, *28*, 379–382.

48. Russell, K.C. Nucleation in Solids: The Induction and Steady State Effects. *Advanced in Colloid and Interface Science* **1980**, *13*, 205–318.

49. Kozeschnik, E. *MODELING SOLID-STATE PRECIPITATION*; Momentum Press, LLC: New York, 2013.

50. Zeldovich, J.B. On the Theory of New Phase Formation Cavitation. *Acta Physicochimica URSS* **1943**, *18*, 1–22.

51. Fischer, F.D.; Svoboda, J.; Kozeschnik, E. Interstitial Diffusion in Systems with Multiple Sorts of Traps. *Model Simul Mat Sci Eng* **2013**, *21*.

52. Fischer, F.D.; Svoboda, J.; Appel, F.; Kozeschnik, E. Modeling of Excess Vacancy Annihilation at Different Types of Sinks. *Acta Mater* **2011**, *59*, 3463–3472.

53. Radis, R.; Kozeschnik, E. Numerical Simulation of NbC Precipitation in Microalloyed Steel. *Model Simul Mat Sci Eng* **2012**, *20*.

54. Dutta, B.; Palmiere, E.J.; Sellars, C.M. Modelling the Kinetics of Strain Induced Precipitation in Nb Microalloyed Steels. *Acta Mater* **2001**, *49*, 785–794.

55. Ahmadi, M.R.; Povoden-Karadeniz, E.; Öksüz, K.I.; Falahati, A.; Kozeschnik, E. A Model for Precipitation Strengthening in Multi-Particle Systems. *Comput Mater Sci* **2014**, *91*, 173–186.

56. Curtin, W.A.; Olmsted, D.L.; Hector, L.G. A Predictive Mechanism for Dynamic Strain Ageing in Aluminium-Magnesium Alloys. *Nat Mater* **2006**, *5*, 875–880.

57. Voce, E. A Practical Strain Hardening Function. *Metallurgia* **1955**, 219–226.

58. Brinckmann, S.; Sivanesapillai, R.; Hartmaier, A. On the Formation of Vacancies by Edge Dislocation Dipole Annihilation in Fatigued Copper. *Int J Fatigue* **2011**, *33*, 1369–1375.

59. Roters, F.; Raabe, D.; Gottstein, G. Work Hardening in Heterogeneous Alloys—a Microstructural Approach Based on Three Internal State Variables. *Acta mater* **2000**, *48*, 4181–4189.

60. Kratochvil, J.; Libovicky, S. Dipole Drift Mechanism of Early Stages of Dislocation Pattern Formation in Deformed Metal Single Crystals. *Pergamon Journals Ltd* **1986**, 1625–1630.

61. Teixeira, J.C.; Bréchet, Y.; Estrin, Y.; Hutchinson, C. The Strain Hardening Behaviour of Supersaturated Al-Cu Alloys. *Proceedings of the 12th International Conference on Aluminium Alloys* **2010**, 536–541.

62. Messerschmidt, U.; Bartsch, M. Generation of Dislocations during Plastic Deformation. *Mater Chem Phys* **2003**, *81*, 518–523.

63. Deschamps, A.; Bréchet, Y.; Necker, C.J.; Saimoto, S.; Embury, J.D. Study of Large Strain Deformation of Dilute Solid Solutions of Al-Cu Using Channel-Die Compression. *Materials Science and Engineering A* **1996**, *207*, 143–152.

64. Ashby, M.F. The Deformation of Plastically Non-Homogeneous Materials. *The Philosophical Magazine: A Journal of Theoretical Experimental and Applied Physics* **1979**, *21*, 399–424.

65. Kreyca, J.; Kozeschnik, E. Temperature-Dependent Strain Hardening, Precipitation and Deformation-Induced Microstructure Evolution in AA 6061. *Materials Science and Engineering A* **2017**, *708*, 411–418.

66. Ozturk, F.; Sisman, A.; Toros, S.; Kilic, S.; Picu, R.C. Influence of Aging Treatment on Mechanical Properties of 6061 Aluminum Alloy. *Mater Des* **2010**, *31*, 972–975.

67. Cheng, L.M.; Poole, W.J.; Embury, J.D.; Lloyd, D.J. The Influence of Precipitation on the Work-Hardening Behavior of the Aluminum Alloys AA6111 and AA7030. *Metallurgical and Materials Transactions A* **2003**, *34*, 2473–2481.

68. Fribourg, G.; Bréchet, Y.; Deschamps, A.; Simar, A. Microstructure-Based Modelling of Isotropic and Kinematic Strain Hardening in a Precipitation-Hardened Aluminium Alloy. *Acta Mater* **2011**, *59*, 3621–3635.

69. Hornbogen, E.; Zum Gahr, K.H. Distribution of Plastic Strain in Alloys Containing Small Particles. *Metallography* **1975**, *8*, 181–202.

70. Blankenship, C.P.; Hornbogen, E.; Starke, E.A. Predicting Slip Behavior in Alloys Containing Shearable and Strong Particles. *Materials Science and Engineering A* **1993**, *169*, 33–41.

71. Kelly, A.; Nicholson, R. Precipitation Hardening. *Prog Mater Sci* **1963**, *10*, 151–391.

72. Poole, W.J.; Wang, X.; Lloyd, D.J.; Embury, J.D. The Shearable-Non-Shearable Transition in Al-Mg-Si-Cu Precipitation Hardening Alloys: Implications on the Distribution of Slip, Work Hardening and Fracture. *Philosophical Magazine* **2005**, *85*, 3113–3135.

73. Bahrami, A.; Miroux, A.; Sietsma, J. Modeling of Strain Hardening in the Aluminum Alloy AA6061. **2013**, *44*, 2409–2417.

74. Marthinsen, K.; Nes, E. Modelling Strain Hardening and Steady State Deformation of Al-Mg Alloys.Pdf. 2001.

75. Viernstein, B.; Kozeschnik, E. Integrated Physical-Constitutive Computational Framework for Plastic Deformation Modeling. *Metals (Basel)* **2020**, *10*, 1–13.

76. Walser, B.; Sherby, O.D. The Structure Dependence of Power Law Creep. *Scripta Metallurgica* **1982**, *16*, 213–219.

77. Brown, A.M.; Ashby, M.F. On the Power-Law Creep Equation. *Scripta Metallurgica* **1980**, *14*, 1297–1302.

78. Frost, H.J.; Ashby, M.F. *Deformation-Mechanism Maps, The Plasticity and Creep of Metals and Ceramics*, 1st ed.; Pergamon Press: Oxford, 1982.

79. Stechauner, G.; Kozeschnik, E. Assessment of Substitutional Self-Diffusion along Short-Circuit Paths in Al, Fe and Ni. *CALPHAD* **2014**, *47*, 92–99.

80. Jonas, J.J. The Back Stress in High Temperature Deformation. *Acta Metallurgica* **1969**, *17*, 397–405.

81. Wong, W.A.; Jonas, J.J. Aluminum Extrusion as a Thermally Activated Process. *Met Soc of AIME -Trans* **1968**, *242*, 2271–2280.

82. Herring, C. Diffusional Viscosity of a Polycrystalline Solid. *J Appl Phys* **1950**, *21*, 437–445.

83. Coble, R.L. A Model for Boundary Diffusion Controlled Creep in Polycrystalline Materials. *J Appl Phys* **1963**, *34*, 1679–1682.

84. Stechauner, G.; Kozeschnik, E. Assessment of Substitutional Self-Diffusion along Short-Circuit Paths in Al, Fe and Ni. *CALPHAD* **2014**, *47*, 92–99.

85. Harper, J.G.; Shepard, L.A.; Dorn, J.E. Creep of Aluminum under Extremely Small Stresses. *Acta Metallurgica* **1958**, *6*, 509–518.

86. Yavari, P.; Miller, D.A.; Langdon, T.G. An Investigation of Harper-Dorn Creep-I. Mechanical and Microstructural Characteristics. *Acta Metallurgica* **1982**, *30*, 871–879.

87. Kassner, M.E.; Kumar, P.; Blum, W. Harper-Dorn Creep. *Int J Plast* **2007**, *23*, 980–1000.

88. Ruano, O.A.; Wadsworth, J.; Sherby, O.D. Harper-Dorn Creep in Pure Metals. *Acta Metallurgica* **1988**, *36*, 1117–1128.

89. Barrett, C.R.; Nix, W.D. High Temperature-Low Stress Creep of Al and Al + 0 . 5 % Fe. *Materials Science and Engineering* **1972**, *10*, 33–42.

90. Lüthy, H.; White, R.A.; Sherby, O.D. Grain Boundary Sliding and Deformation Mechanism Maps. *Materials Science and Engineering* **1979**, *39*, 211–216.

91. Ruano, O.A.; Miller, A.K.; Sherby, O.D. The Influence of Pipe Diffusion on the Creep of Fine-Grained Materials. *Materials Science and Engineering* **1981**, *51*, 9–16.

92. Hayden, H.W.; Floreen, S.; Goodell, P.D. The Deformation Mechanisms of Superplasticity. *Metallurgical and Materials Transactions B* **1972**, *3*, 833–842.

93. Alden, T.H. The Origin of Superplasticity in the Sn-5%bi Alloy. *Acta Metallurgica* **1967**, *15*, 469–480.

94. Herriot, G.; Suery, M.; Baudelet, B. Superplastic Behaviour of the Industrial Cu7wt.%P ALLOY. *Scripta Metallurgica* **1972**, *6*, 657–662.

95. Viernstein, B.; Wojcik, T.; Kozeschnik, E. State Parameter-Based Yield Strength Model for Integration in Finite Element User-Material Routines. *Metals (Basel)* **2022**, *12*.

96. Kreyca, J.; Kozeschnik, E. State Parameter-Based Constitutive Modelling of Stress Strain Curves in Al-Mg Solid Solutions. *Int J Plast* **2018**, *103*, 67–80.

97. Viernstein, B.; Solyom, L.; Kozeschnik, E. Strain Hardening in Dilute Binary Al–Cu, Al–Zn, and Al–Mn Alloys: Experiment and Modeling. *Metall Mater Trans A Phys Metall Mater Sci* **2024**, *55*, 3627–3639.

98. Yang, M.; Chen, H.; Orekhov, A.; Lu, Q.; Lan, X.; Li, K.; Zhang, S.; Song, M.; Kong, Y.; Schryvers, D.; Du, Y. Quantified Contribution of B" and B' Precipitates to the Strengthening of an Aged Al–Mg–Si Alloy. *Materials Science and Engineering A* **2020**, *774*, 138776.

99. Zhou, W.B.; Teng, G.B.; Liu, C.Y.; Qi, H.Q.; Huang, H.F.; Chen, Y.; Jiang, H.J. Microstructures and Mechanical Properties of Binary Al-Zn Alloys Fabricated by Casting and Heat Treatment. *J Mater Eng Perform* **2017**, *26*, 3977–3982.

100. Somerday, M.; Humphreys, F.J. Recrystallisation Behaviour of Supersaturated Al-Mn Alloys. Part 1 - Al-1.3 Wt-%Mn. *Materials Science and Technology* **2003**, *19*, 20–29.

101. Lüthy, H.; White, R.A.; Sherby, O.D. Grain Boundary Sliding and Deformation Mechanism Maps. *Materials Science and Engineering* **1979**, *39*, 211–216.

102. Falkinger, G.; Simon, P. Static Recovery of an AlMg4.5Mn Aluminium Alloy during Multi-Pass Hot-Rolling. In *Procedia Engineering*; 2017; Vol. 207, pp 31–36.

103. Gubicza, J.; Chinh, N.Q.; Horita, Z.; Langdon, T.G. Effect of Mg Addition on Microstructure and Mechanical Properties of Aluminum. *Materials Science and Engineering: A* **2004**, *387–389*, 55–59.

104. Gubicza, J.; Chinh, N.Q.; Horita, Z.; Langdon, T.G. Effect of Mg Addition on Microstructure and Mechanical Properties of Aluminum. *Materials Science and Engineering: A* **2004**, *387–389*, 55–59.

9 Appendix

Key Publications

Paper 1

Viernstein, B., Kozeschnik, E., Integrated physical-constitutive computational framework for plastic deformation modeling, Metals, 10(7), pp. 1–13, 869.

Paper 2

Viernstein, B., Tomasz W., Kozeschnik, E., State Parameter-Based Yield Strength Model for Integration in Finite Element User-Material Routines, Metals, 12(7), pp 1-16, 1207.

Paper 3

Viernstein, B., Tomasz W., Kozeschnik, E., State Parameter-Based Yield Strength Model for Integration in Finite Element User-Material Routines, Metals, 12(7), pp 1-16, 1207.

Journal Paper 1

Article

Integrated Physical-Constitutive Computational Framework for Plastic Deformation Modeling

Bernhard Viernstein *and Ernst Kozeschnik

Institute of Materials Science and Technology, TU Wien, Getreidemarkt 9, 1060 Vienna, Austria;

ernst.kozeschnik@tuwien.ac.at

***** Correspondence: bernhard.viernstein@tuwien.ac.at; Tel.: +43-1-58801-308103

Received: 31 March 2020; Accepted: 26 June 2020; Published: date

Abstract: An integrated framework for deformation modeling has been developed, which combines a physical state parameter-based formulation for microstructure evolution during plastic deformation processes with constitutive creep models of polycrystalline materials. The implementations of power law, Coble, Nabarro–Herring and Harper–Dorn creep and grain boundary sliding are described and their contributions to the entire stress response at a virtual applied strain rate are discussed. The present framework simultaneously allows calculating the plastic deformation under prescribed strain rate or constant stress, as well as stress relaxation after preceding stress or strain loading. The framework is successfully applied for the construction of deformation mechanism maps.

Keywords: creep; dislocations; microstructure; relaxation

---

1. Introduction

The physical understanding of creep mechanisms has been of significant academic interest within the last decades. Especially, the creep response of pure Al has been investigated over a wide temperature and stress range. The physical process of plastic flow is still the subject of controversial discussions for some deformation regimes [1–4], but semi-empirical equations

in literature satisfactorily reproduce the experimentally obtained stress-strain relations. The power law regime is associated with vacancy-assisted climb of dislocations, while diffusional flow of atoms is attributed to Coble creep [5] and Nabarro–Herring creep [6]. At low stresses and large grain sizes, Harper–Dorn creep dominates [7–11]. In fine grain structures, grain boundary sliding can control the deformation process [12–16].

In the present work, characteristic creep relations are brought into a homogeneous form and used to calculate the stress response of polycrystalline materials to a constant applied strain rate or the strain rate resulting from an applied external stress load, respectively. Since this framework is based on fundamental plastic deformation mechanisms, thermomechanical simulations are possible for a broad spectrum of metallic materials. Therefore, only characteristic material parameters, which are described in the following discussion, need to be calibrated for each material. Within this work, the model is exemplarily applied to Al. An inverse summation rule of the individual stress contributions ensures that the dominant deformation mechanism mainly defines the overall thermally activated stress response. Microstructural changes during the deformation process are represented by the average dislocation density evolution. The utilized Kocks–Mecking approach considers dislocation generation as well as dynamic and static recovery for dislocation annihilation. The combination of thermally activated stress contributions and the athermal stress contribution from dislocation hardening allows simulating the stress-strain relations over a wide range of temperatures and strain rates. This framework allows for modeling of plastic deformation by dislocation glide as well as of primary creep and secondary creep. The strain rate acceleration and damage accumulation due to cavitation, cracks or both is not considered, which is typical for tertiary creep. Consequently, this framework is valid for experiments, where creep damage is effectively suppressed, or for materials which show a pronounced secondary creep stage. As an additional feature, stress relaxation tests from literature are successfully simulated within this work to compare the simulation framework with experimental data.

Although not elaborated in the present work, the framework is fully capable of considering microstructural features, such as fine grain hardening, dislocation locking by Cottrell atmospheres or precipitates. Application of the latter two mechanisms has been demonstrated recently by Soliman et al. [17]. These features provide further barriers for ongoing dislocation glide, leading to a higher stress response to an applied strain rate.

Diffusion creep, such as Coble creep and Nabarro–Herring creep, are not affected by those microstructural barriers.

2. The model

The following two subchapters describe the implementation of both aspects of this framework, which are the constitutive creep relations on the one hand, and physically-based microstructure evolution on the other hand. A combination of the prevailing stress contribution is presented in chapter 3, Results and Discussion.

2.1. Constitutive Modeling of Creep

The deformation characteristics of crystalline materials are mainly controlled by the applied strain rate / external stress loading as well as temperature. Dependent on the particular combination of these parameters, the deformation process is made possible by different physical mechanisms. Generally, at high temperatures, the deformation characteristics show considerable dependency on the applied stress in combination with a low amount of strain hardening. At high temperatures, various creep mechanisms can be operative simultaneously, whereas mostly dislocation glide facilitates plastic deformation at low temperature, high stress or both. Interactions with obstacles, such as grain boundaries, solute atoms, precipitates or other dislocations cause a barrier for an ongoing movement of the mobile dislocations that carry the plastic deformation process. Consequently, the various obstacle strengths determine the rate of dislocation motion and, thus, the strain rate, $\dot{\varepsilon}$, which is typically represented by an Arrhenius equation [18–23] as

$$\dot{\varepsilon} = \dot{\varepsilon}_0 \cdot \exp\left(\frac{-\Delta G}{k_\mathrm{B} \cdot T}\right). \tag{1}$$

$\dot{\varepsilon}_0$ is a constant [24], k_B the Boltzmann constant, T is the temperature and ΔG is the shear stress-dependent free activation enthalpy, which can be expressed by [20]

$$\Delta G(\sigma_\mathrm{s}) = \Delta F \cdot \left[1 - \left(\frac{\sigma_\mathrm{s}}{\hat{\tau}}\right)^p\right]^q. \tag{2}$$

ΔF is the is the total free energy to overcome the obstacle barrier, σ_s the applied shear stress, $\hat{\tau}$ the mechanical threshold, which represents the activation energy barrier in the absence of thermal activation, and p and q define the shape of the energy barrier. In the following, a box shaped barrier is assumed by $p = q = 1$. A combination of Equations (1) and (2) leads to

$$\dot{\varepsilon} = \dot{\varepsilon}_0 \cdot \exp\left[-\frac{\Delta F}{k_B \cdot T} \cdot \left(1 - \frac{\sigma_S}{\hat{\tau}}\right)\right]. \quad (3)$$

At lower stresses, higher temperatures or both, ($T \geq 0.3 \cdot T_m$), diffusion-controlled deformation regimes, instead of dislocation glide, become dominant. T_m is the melting temperature. Although the following phenomenological equation does not describe the creep process on a physical basis, it is often successfully applied in literature [20,25,26] and it is also included within this framework as

$$\dot{\varepsilon} = \frac{A \cdot D_{tr} \cdot G \cdot b}{k_B \cdot T} \cdot \left(\frac{\sigma_S}{G}\right)^n. \quad (4)$$

D_{tr} is the tracer diffusion coefficient of the matrix-forming element, G the shear modulus and *b* the Burgers vector. Brown and Ashby [26] empirically correlated the coefficients, *A* and *n*, based on detailed evaluations of creep data of bcc, fcc, hpc metals (including their alloys), dispersion hardened materials, cubic elements, alkali halides and oxides. Missing explanations for the observed values of *n* and a huge variety in *A* of many orders of magnitude motivated Frost and Ashby to include dislocation core diffusion additionally to the bulk matrix diffusion coefficient [20]. Consequently, two rate equations are obtained: At low temperatures or high stresses, dislocation core diffusion is dominant, while lattice diffusion is the dominant mechanism at high temperatures and low stresses. In the following, both mechanisms, which are termed as low-temperature creep, LT creep, and high-temperature creep, HT creep, are dealt with separately. The weighted combination of creep mechanisms is discussed in section 3. The strain rate, $\dot{\varepsilon}_{HT}$, for HT creep can be expressed as

$$\dot{\varepsilon}_{HT} = \frac{A_{HT} \cdot G \cdot b \cdot D_{eff}}{k_B \cdot T} \cdot \left(\frac{\sigma_S}{G}\right)^{n_{HT}}. \quad (5)$$

n_{HT} is a coefficient and A_{HT} is microstructure-dependent within the present framework (see section 3). D_{eff} is the effective diffusion coefficient that includes trapping of vacancies at solute atoms [27], excess vacancies [28] and dislocation pipe diffusion [29,30] as inherent diffusion mechanisms. The migration of vacancies predominantly determines diffusion in polycrystalline solids. Here, the creation and annihilation of vacancies at grain boundaries, dislocation jogs or Frank loops are considered within the FSAK model [28]. Additionally, an increasing dislocation density during deformation causes a higher effective diffusion coefficient based on a higher pipe diffusion contribution. The strain rate $\dot{\varepsilon}_{LT}$ for the LT creep contribution is calculated as

$$\dot{\varepsilon}_{\mathrm{LT}} = \frac{A_{\mathrm{LT}} \cdot G \cdot b \cdot D_{\mathrm{c}}}{k_{\mathrm{B}} \cdot T} \cdot \left(\frac{\sigma_{\mathrm{S}}}{G}\right)^{n_{\mathrm{LT}}}. \tag{6}$$

n_{LT} is a constant, A_{LT} is a state-dependent parameter and D_{c} is the dislocation core diffusion coefficient, which, for Al-based alloys, is given by a correlation with the tracer diffusion coefficient D_{tr} [31]:

$$D_{\mathrm{c}} = 0.11 \cdot \exp\left(\frac{Q_{\mathrm{tr}} - Q_{\mathrm{c}}}{R \cdot T}\right) \cdot D_{\mathrm{tr}}. \tag{7}$$

Q_{tr} and Q_{c} are the activation energies for bulk diffusion and dislocation core diffusion. *R* is the universal gas constant. Above a certain stress of approximately $10^{-3}G$, the stress-strain relation typically changes, which is referred to as power law breakdown (PLB). This phenomenon is intensively discussed in literature [32,33]. Within the present framework, the following empirical equation is utilized

$$\dot{\varepsilon}_i = \frac{A_i \cdot G \cdot b \cdot D_i}{k_{\mathrm{B}} \cdot T} \cdot \left[\sinh\left(\alpha' \cdot \frac{\sigma_{\mathrm{S}}}{G}\right)\right]^{n_i}. \tag{8}$$

$\dot{\varepsilon}_i$, A_i, D_{i} and n_i refer to the prevailing deformation mechanisms and α' specifies the stress level at which the power law break down starts.

At low applied stresses ($\sigma/G < 10^{-5}$) and small grain sizes, diffusional flow determines the deformation process. In contrast to power law creep, strain is caused by the diffusion of vacancies, rather than dislocation mechanisms. This deformation mode has first been described by Nabarro and Herring [6]. The corresponding creep rate $\dot{\varepsilon}_{\mathrm{NH}}$, as implemented within the present framework, is given by [20]

$$\dot{\varepsilon}_{\mathrm{NH}} = \frac{42 \cdot b^3 \cdot D_{\mathrm{eff}}}{k_{\mathrm{B}} \cdot T \cdot d^2} \cdot \sigma_{\mathrm{S}}, \tag{9}$$

where *d* is the grain size. Since lattice diffusion is the predominate mechanism, the effective matrix diffusion coefficient, D_{eff}, is utilized.

Vacancy diffusion along grain boundaries instead of lattice diffusion leads to Coble creep [5]. The strain rate, $\dot{\varepsilon}_{\mathrm{C}}$, for Coble creep is formulated as

$$\dot{\varepsilon}_{\mathrm{C}} = \frac{42 \cdot b^3 \cdot \pi \cdot \delta \cdot D_{\mathrm{gb}}}{k_{\mathrm{B}} \cdot T \cdot d^3} \cdot \sigma_{\mathrm{S}}. \tag{10}$$

δ is the effective boundary thickness and D_{gb} is the grain boundary diffusion coefficient, which, for Al-based alloys is given [31] as

$$D_{\mathrm{gb}} = 1.4 \cdot \exp\left(\frac{Q_{\mathrm{tr}} - Q_{\mathrm{gb}}}{R \cdot T}\right) \cdot D_{\mathrm{tr}}. \tag{11}$$

Q_{gb} is the activation energy for grain boundary diffusion. At low stresses and large grain sizes, another deformation mechanism occurs, which was first reported by Harper et al. in 1957 [7]. In the following fifty years, the Harper–Dorn regime has been identified in many studies [7–11]. A phenomenological relation between the applied stress, σ_{s}, and the creep rate, $\dot{\varepsilon}_{\mathrm{HD}}$, reads

$$\dot{\varepsilon}_{\mathrm{HD}} = \frac{A_{\mathrm{HD}} \cdot D_{\mathrm{eff}} \cdot G \cdot b}{k_{\mathrm{B}} \cdot T} \cdot \left(\frac{\sigma_{\mathrm{s}}}{G}\right), \tag{12}$$

where A_{HD} is a coefficient. Equal to the Nabarro–Herring creep, $\dot{\varepsilon}_{\mathrm{HD}}$ increases linearly with the applied stress, σ_{s}, (Newtonian nature) and the activation energy is of the magnitude of self-diffusion. However, measured steady-state creep rates of Harper–Dorn creep are often higher by a factor of approximately 1400. Low initial dislocation densities, as well as high purity of the material, favor Harper–Dorn creep, as reported by [4,11]. The low steady-state dislocation density typical for this deformation mechanism remains constant and is independent of σ [8]. A possible explanation is given by the Ardell–Przystupa–Lee (APL) dislocation network theory [1]. The mechanism of the deformation process during Harper–Dorn creep has been discussed intensively in literature [4,7–10] and its analysis is beyond the of scope of this work. Another deformation mechanism, which can control the plastic behavior of fine-grained polycrystalline materials, is based on grain boundary sliding (GBS). Many observations confirm an inverse dependency of the strain rate, $\dot{\varepsilon}_{\mathrm{GBS}}$, on squared or cubed grain size [12–16]. If the activation energy is associated with grain boundary diffusion, D_{gb}, the creep rate is [12]:

$$\dot{\varepsilon}_{\mathrm{GBS-GB}} = \frac{A_{\mathrm{GBS-GB}} \cdot D_{\mathrm{gb}} \cdot G \cdot b^4}{k_{\mathrm{B}} \cdot T \cdot d^3} \cdot \left(\frac{\sigma}{G}\right)^2, \tag{13}$$

where the coefficient $A_{\mathrm{GBS-GB}} = 2 \cdot 10^5$. If effective lattice diffusion D_{eff} is the rate controlling mechanism, the following equation is utilized [12]:

$$\dot{\varepsilon}_{\mathrm{GBS-L}} = \frac{A_{\mathrm{GBS-L}} \cdot D_{\mathrm{eff}} \cdot G \cdot b^3}{k_{\mathrm{B}} \cdot T \cdot d^2} \cdot \left(\frac{\sigma}{G}\right)^2, \tag{14}$$

where the coefficient $A_{\mathrm{GBS-L}} = 8 \cdot 10^6$. The impact of grain boundary sliding processes on conventional Ashby–Frost [20] and Langdon–Mohamed [34,35] deformation mechanism maps are described by Lüthy et al. [12]. It is shown for Ni that D_{gb}- and D_{l}-controlled GBS

strongly reduces Coble creep and suppresses Nabarro–Herring creep to insignificant normalized stresses within the Ashby maps. Although Coble creep and Nabarro–Herring creep are overtaken by grain boundary sliding in Al at all temperatures at an applied normalized stress of $\sigma/G = 10^{-4}$, these mechanisms are incorporated into the framework to achieve a generalized form of all creep mechanisms. Except for the dislocation glide mechanism, all thermally activated deformation processes introduced so far are diffusion-controlled, either by lattice diffusion, pipe diffusion or grain boundary diffusion. The present models describe the activation of dislocation glide, dislocation climb and vacancy diffusion; however, under the assumption of a constant microstructure and no accumulation of creep damage, which is the condition of steady state creep. In real materials, the dislocation density changes during deformation before the steady-state dislocation density is reached. This microstructure evolution is characteristic for the transient range of creep and is discussed in the following.

2.2. Physical Modeling of Microstructure Evolution

For the simulation of the stress evolution during thermomechanical treatments, the knowledge of the current microstructure is mandatory. Therefore, physically based models are utilized, which can simulate the evolution of grain sizes [36,37], nucleation and growth of precipitates, or the current dislocation density. All these models are already implemented within the thermo-kinetic software package MatCalc (http://matcalc.at). To incorporate the dislocation strengthening contribution accompanying the transient deformation region, following extended one-parameter model of Kocks and Mecking is used to calculate the temperature and strain rate dependent dislocation density evolution [24]:

$$\frac{\mathrm{d}\rho}{\mathrm{d}\varepsilon} = \frac{\mathrm{d}\rho^{+}}{\mathrm{d}\varepsilon} + \frac{\mathrm{d}\rho^{-}}{\mathrm{d}\varepsilon} + \frac{\mathrm{d}\rho_{s}^{-}}{\mathrm{d}\varepsilon} = \frac{M}{bA}\sqrt{\rho} - 2BM\frac{d_{\mathrm{crit}}}{b}\rho - 2CD_{\mathrm{d}}\frac{Gb^{3}}{\dot{\varepsilon}kT}\left(\rho^{2} - \rho_{\mathrm{eq}}^{2}\right). \quad (15)$$

The Taylor factor, *M*, relates the macroscopically observed flow stress to the critical resolved shear stress acting on a slip plane within a polycrystalline material. *A* and *B* are material-specific coefficients and d_{crit} is the critical annihilation distance between two dislocations [24]. *C* is a constant and ρ_{eq} is the equilibrium dislocation density. The generation of dislocations $\frac{\mathrm{d}\rho^{+}}{\mathrm{d}\varepsilon}$ is caused by dislocation storage in the crystal, being inversely proportional to the current mean distance between dislocations and the dislocation density, □, respectively. Annihilation of dislocations occurs by cross slip processes $\frac{\mathrm{d}\rho^{-}}{\mathrm{d}\varepsilon}$ at low and intermediate

temperatures and by vacancy-assisted climb $\frac{\mathrm{d}\rho_s^-}{\mathrm{d}\varepsilon}$ at high temperatures. The latter annihilation process represents static recovery, which is marked by the index *s*. The Taylor equation correlates the athermal, plastic stress contribution with the dislocation density ρ [38,39] as

$$\sigma_\mathrm{p} = \alpha \cdot M \cdot b \cdot G \cdot \sqrt{\rho}\,. \tag{16}$$

The MatCalc software package includes models for the growth and shrinkage of subgrains during plastic deformation, which are out of scope in the present work. The calculation of the average dislocation density for the athermal stress contribution has often been validated [24] and possible industrial applications, such as hot rolling processes, which additionally include recrystallization, have been demonstrated recently [40].

In terms of the possible evolution of the precipitate microstructure, the SFFK model [41–43] is utilized as implemented in the MatCalc software package. Within this framework, a thermodynamic system out of equilibrium state is described by the Gibbs energy, *G,* given by

$$G = \sum_{i=1}^{n} N_{0i} \cdot \mu_{0i} + \sum_{k=1}^{m} \frac{4 \cdot \pi \cdot \rho_k^3}{3} \left(\lambda_k + \sum_{i=1}^{n} c_{ki} \cdot \mu_{ki} \right) + \sum_{k=1}^{m} 4 \cdot \pi \cdot \rho_k^2 \cdot \gamma_{k.} \tag{17}$$

The index *i* represents the component *i* in the matrix and the index *k* represents a specific precipitate with the radius ρ. N_0 is the number of moles, μ_0 the chemical potential, *c* the concentration and λ accounts for the elastic energy, which is associated with the elastic stress field around the precipitate. γ is the interface free energy density.

The steady-state nucleation rate, J_s, which is defined as the number of formed nuclei per unit volume and unit time, is given by [44,45]

$$J_\mathrm{s} = Z \cdot \beta^* \cdot N_\mathrm{C.} \exp\left(\frac{-\Delta G^*}{k_\mathrm{B} \cdot T}\right), \tag{18}$$

where Z is the Zeldovich factor, β^* the atomic attachment rate, N_C the number of available nucleation sites and ΔG^* is the critical nucleation energy. Equations (17) and (18) provide the basis for rather complex precipitation evolution models, which cause strengthening contributions by shearing- and non-shearing mechanisms. A detailed discussion of precipitation strengthening is beyond the scope of this work and the authors refer to Ahmadi et al. [46]. Solid solution strengthening models as well as the cross core diffusion effect, which can lead to negative strain-rate sensitivity, are implemented in MatCalc and successfully applied, e.g., in Kreyca and Kozeschnik [24]. These thermally activated stress contributions are

linked to the present framework by the mechanical threshold $\hat{\tau}$ (Equation (3)). In the following, $\hat{\tau}$ is assumed to remain constant for the benefit of clear discussion.

3. Results and Discussion

In classical creep tests, a constant stress is applied and the resulting creep rate is measured. In an inverse methodology, the creep relations described in the previous section can be utilized to calculate stresses at an applied constant true strain rate. The stress response σ_{G} of pure dislocation glide is calculated by Equation (3) and leads to

$$\sigma_{\mathrm{G}} = \hat{\tau} \cdot \left(1 - \left[\frac{k_{\mathrm{B}} \cdot T}{\Delta F}\right] \cdot \ln\left(\frac{\dot{\varepsilon}}{\dot{\varepsilon}_0}\right)\right). \tag{19}$$

Since Equation (19) delivers negative stress values above a certain critical temperature, T_{crit}, the following alternative equation is widely used in literature [24]:

$$\sigma_{\mathrm{G}} = \hat{\tau} \cdot \exp\left(\frac{-k_{\mathrm{B}} \cdot T}{\Delta F} \cdot \ln\left(\frac{\dot{\varepsilon}_0}{\dot{\varepsilon}}\right)\right). \tag{20}$$

The following equations summarize the present implementation of the LT creep, the HT creep and the Harper–Dorn creep in the integrated framework of deformation modeling. The indices display the different associated pre-factors, *A*, the diffusion coefficients, *D*, as well as the exponents, *n*, with

$$\sigma_i = \left(\frac{k_{\mathrm{B}} \cdot T \cdot \dot{\varepsilon}}{A_i \cdot D_i \cdot G \cdot b}\right)^{\frac{1}{n_i}} \cdot G. \tag{21}$$

The power law breakdown regime is implemented with

$$\sigma_i = \sinh^{-1}\left(\frac{k_{\mathrm{B}} \cdot T \cdot \dot{\varepsilon}}{A_i \cdot D_i \cdot G \cdot b}\right)^{\frac{1}{n_i}} \cdot \frac{G}{\alpha'}. \tag{22}$$

The stress response of Nabarro–Herring creep, σ_{NH}, and Coble creep, σ_{C}, are calculated by Equations (9) and (10) and D_{gb}- and D_{l}-controlled GBS are calculated by Equations (13) and (14). Kreyca [47] has correlated the thermally activated dynamic yield stress contribution at high temperatures with the HT power law creep relation, Equation (5), leading to the relation

$$A_{\mathrm{HT}} \propto \frac{\Delta F}{D_{\mathrm{eff}} \cdot \hat{\tau}} \cdot \exp\left(\frac{-\Delta F}{R \cdot T}\right), \tag{23}$$

where ΔF is the activation energy for lattice diffusion and D_{eff} is the effective diffusion coefficient. Although it is not very common to connect the mechanical threshold concept $\hat{\tau}$ with the creep behavior, this approach takes the influence of microstructure features, such as

precipitates on the creep rate, into account. It should be emphasized that the particular microstructural state also influences the diffusion coefficient, $\mathrm{D_{eff}}$, of Equation (23) by trapping effects, pipe diffusion or by excess vacancies. For correlating A_{LT} of Equation (6) with the mechanical threshold concept, the core diffusion z as well as the activation energy for pipe diffusion are utilized. This concept is used for calibrating A_{LT} and A_{HT} in the following. Figure 1 shows the Harper–Dorn creep (HD) and power law creep (PL) regime, including the power law breakdown (PLB) at higher stresses. The symbols indicate the normalized strain rate, $\dot{\varepsilon}\cdot k_{\mathrm{B}}\cdot T/D_{\mathrm{eff}}\cdot G\cdot b$, as a function of the normalized stress σ/G from Straub and Blum [48] for pure 99.999 Al.

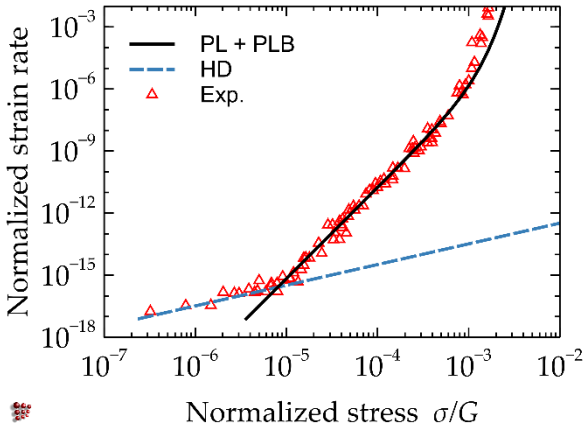

Figure 1. Harper–Dorn creep (HD), power law creep (PL), including power law breakdown (PLB). Symbols indicate experimental results for pure 99.999 Al from [48]. The normalized strain rate is defined by $\dot{\varepsilon}\cdot k_{\mathrm{B}}\cdot T/D_{\mathrm{eff}}\cdot G\cdot b$.

All simulation input parameters are listed in Table 1, but instead of α' = 1000, which is a typical value in literature [20], better agreement with experimental results are achieved with α' = 1300 in this case. In determination of the overall creep behavior, the assumption is made that the creep mechanism with the lowest resulting stress and, therefore, lowest deformation resistance, is dominant. The following summation rule is utilized

$$\left(\frac{1}{\sigma_{\mathrm{ges}}}\right)^{n_{\mathrm{c}}} = \left(\frac{1}{\sigma_{\mathrm{G}}}\right)^{n_{\mathrm{c}}} + \left(\frac{1}{\sigma_{\mathrm{LT}}}\right)^{n_{\mathrm{c}}} + \left(\frac{1}{\sigma_{\mathrm{HT}}}\right)^{n_{\mathrm{c}}} + \left(\frac{1}{\sigma_{\mathrm{NH}}}\right)^{n_{\mathrm{c}}} + \left(\frac{1}{\sigma_{\mathrm{C}}}\right)^{n_{\mathrm{c}}} + \left(\frac{1}{\sigma_{\mathrm{GBS-GB}}}\right)^{n_{\mathrm{c}}} + \left(\frac{1}{\sigma_{\mathrm{GBS-L}}}\right)^{n_{\mathrm{c}}} + \left(\frac{1}{\sigma_{\mathrm{HD}}}\right)^{n_{\mathrm{c}}}, \tag{24}$$

where n_{c} is the coupling coefficient. The total stress contribution at a certain temperature and strain rate is the sum of the athermal stress contribution, σ_{p}, of Equation (16) and σ_{ges} of Equation (24). Except for the dislocation glide mechanism, each creep regime is characterized

by a linear relation in a double-logarithmic plot until the power law breakdown is reached at high stresses. Exemplary stress-strain rate relations are illustrated in Figure 2 for all discussed deformation regimes at different temperatures from 100 to 500 °C, whereas σ_{ges} of Equation (24) is represented by the bold line, labeled ”DYN”. Table 1 lists all simulation input parameters.

Table 1. Parameters to calculate each deformation regime.

Symbol	Name	Unit	Value	Equation	Source
G	Shear modulus	MPa	29,438.4–15.052T	13,14,21,22	[49]
b	Burgers Vector	m	$2.86 \cdot 10^{-10}$	9,10,13,14, 21,22	[20]
α	Strengthening coefficient	-	0.34	16	[39]
M	Taylor factor	-	3.06	16	[24]
ΔF	Activation energy	J/mol	$0.25 \cdot G \cdot b^3$	19	[20]
$\dot{\varepsilon}_0$	constant	-	$1.46 \cdot 10^5$	19	[24]
δ	Effective boundary thickness	m	$2 \cdot 10^{-9}$	10	(MatCalc)
d	Grain size	m	$5 \cdot 10^{-6}$	9,10,13,14	This work
A_{LT}	LT constant	-	$5.71 \cdot 10^{-13}$	22	This work
A_{HT}	HT constant	-	$4.23 \cdot 10^{-7}$	22	This work
A_{HD}	HD constant	-	$1 \cdot 10^{-10}$	21	[20]
$A_{\mathrm{GBS-GB}}$	D_{GB} -controlled GBS coefficient	-	$2 \cdot 10^5$	13	[12]
$A_{\mathrm{GBS-L}}$	D_{l}-controlled GBS coefficient	-	$8 \cdot 10^6$	14	[12]
n_{c}	coupling coefficient	-	10	24	This work
α'	PLB	-	1000	24	[20]
n_{LT}	LT exponent	-	6.4	22	[20]
n_{HT}	HT exponent	-	4.4	22	[20]
n_{HD}	HD exponent	-	1	21	[20]
Q_{tr}	Activation energy for bulk diffusion	J/mol	127,200	7,11	[31]
Q_{c}	Activation energy for dislocation core diffusion	J/mol	83,200	7	[31]
Q_{gb}	Activation energy for grain boundary	J/mol	60,200	11	[31]

The exponent *n* of the power law mechanism (Equations (5) and (6)) determines the slope of the LT creep and the HT creep range, until the PLB becomes dominant. The Nabarro–Herring creep, the Coble creep and the Harper–Dorn creep deliver parallel shifted results based on the linear relation of stress and strain rate. The slope of the GBS regime is steeper and crosses the

Coble creep mechanism at a specific stress value, which depends on the initial grain size, which is 5 µm in this case, and the deformation temperature. At 100 °C, 200 °C and 300 °C, grain boundary diffusion-controlled GBS is dominant at intermediate stress values, which is finally overtaken by dislocation glide (at 100 °C) or high temperature creep (at 200 °C and 300 °C) at high stresses. Above 400 °C, D_{l}-controlled GBS replaces D_{gb}-controlled GBS as dominant deformation mode. Figure 2 illustrates that GBS controls plastic flow in the intermediate stress range, separating diffusional flow and power law creep range, in good agreement with literature [12]. The transition of these deformation regimes is governed by the exponent n_{c} in Equation (24). The higher the coupling coefficient n_{c}, the closer is the resulting stress, σ_{ges}, to the prevailing mechanism. A value of n_{c} = 10 is used in the present analysis, which assures that the resulting curves are rather close to the strain rates predicted by the dominating mechanism and numerical artifacts are minimized.

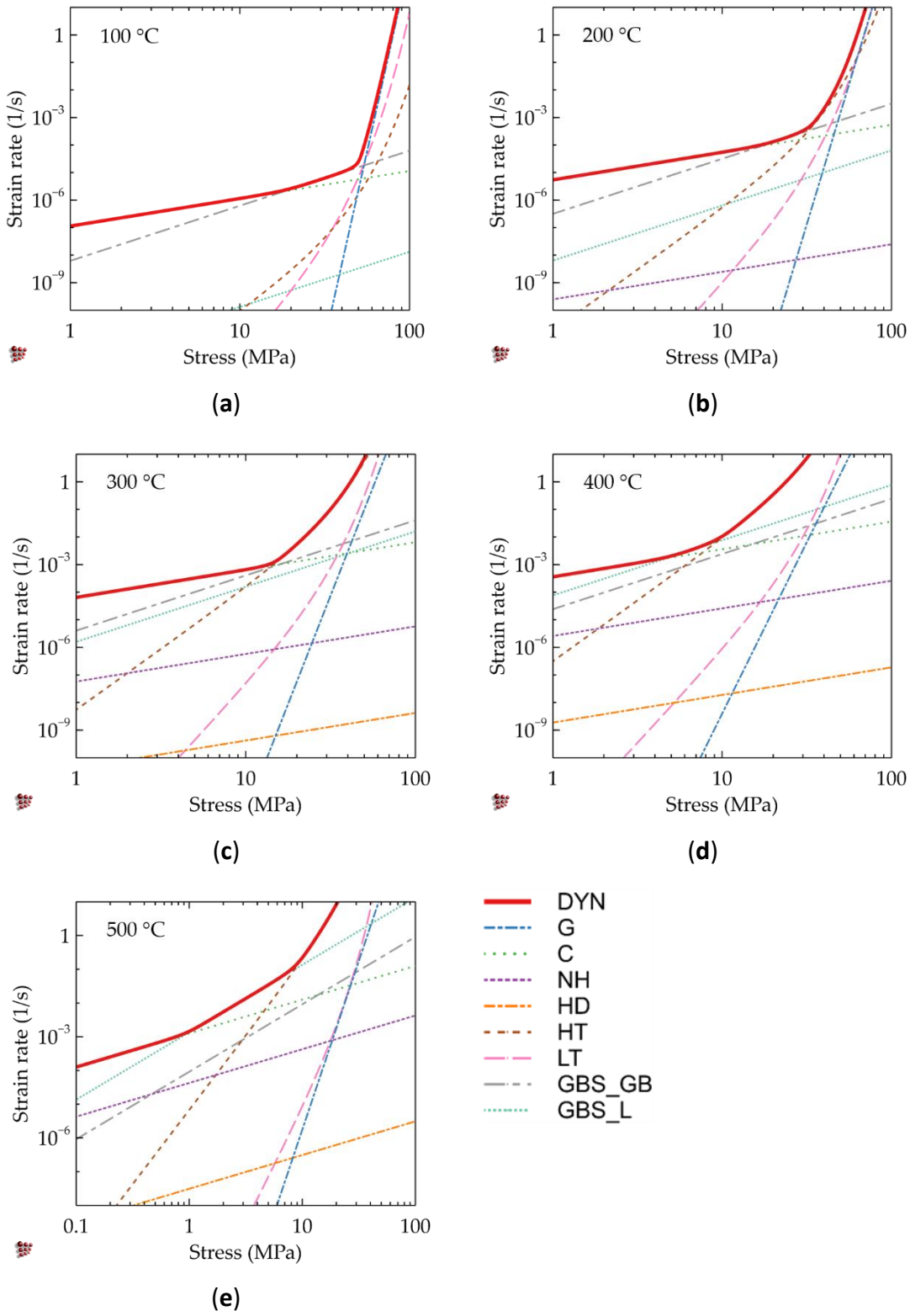

Figure 2. Dislocation glide (G), LT creep (LT), HT creep (HT), Nabarro–Herring creep (NH), Coble creep (C), Harper–Dorn creep (HD), and D_{gb}- and D_l-controlled GBS (GBS_GB and GBS_L) at different constant strain rates at (**a**) 100 °C; (**b**) 200 °C; (**c**) 300 °C; (**d**) 400 °C and (**e**) 500 °C. The resulting stress, σ_{ges}, of Equation (21) is displayed as bold line (DYN).

The mechanical threshold, $\hat{\tau}$, which represents the activation energy barrier in the absence of thermal activation, needs to be defined to calculate the dislocation glide contribution, especially at low temperatures (see Equation (20)). Since $\hat{\tau}$ comprises solid solution hardening, precipitation hardening and cross core diffusion hardening (see section 2.2, Physical modeling of microstructure evolution), the evolution of the microstructure during the deformation processes is inherently included in the integrated model. In the present analysis, no precipitation processes occur in this setup, leading to a constant mechanical threshold $\hat{\tau}$ = 145 MPa and consequently, to constants A_{LT} and A_{HT}.

The present framework allows calculating both, stresses during constant strain rates as well as time-dependent stress relaxation. The stress reduction, $\dot{\sigma}$, during relaxation is assumed to occur along the elastic region with

$$\dot{\sigma} = E \cdot \dot{\varepsilon}, \tag{25}$$

where *E* is the Youngs modulus. Hence, the stress reduction, $\dot{\sigma}$, is defined by the current dynamic strain rate, $\dot{\varepsilon}$. The new stress value, $\sigma_{t+\Delta t}$, in each iteration step, Δt, of the numerical integration procedure is given by

$$\sigma_{t+\Delta t} = \sigma_t - \dot{\sigma} \cdot \Delta t. \tag{26}$$

For a given materials' microstructure, each stress value corresponds to a unique strain rate, which determines the next stress relaxation step in Equation (25). In this setup, simulations of relaxation tests are carried out. Figure 3a shows relaxation curves of an AlMg4.5Mn alloy, after compressing cylindrical specimens with a constant strain rate of 0.01 (1/s) at different temperatures (350 °C, 400 °C, 450 °C, 500 °C). The experimental points are adopted from the work of Falkinger and Simon [50]. Figure 3b depicts the decreasing strain rate during the relaxation process, starting from 0.01 (1/s). The higher the deformation temperature in the pre-step, the lower the initial stress level for relaxation is, resulting in lower strain rates. The stress reduction of the HT creep (HT), the LT creep (LT), the Coble creep, lattice diffusion controlled GBS as well as grain boundary diffusion-controlled GBS are illustrated for 350 °C in Figure 3c and 500 °C in Figure 3d. According to Equation (24), Nabarro–Herring and Harper–Dorn creep are negligible in this example setup, due to their exceeding stress contributions. The calibration settings are summarized in Table 1, but $\mathrm{A_{HT}} = 2.15 \cdot 10^{-11}$ and $\mathrm{A_{LT}} = 5.71 \cdot 10^{-17}$ for this specific alloy. Usually, $\mathrm{A_{HT}}$ and $\mathrm{A_{LT}}$ are calibrated by conventional creep tests instead of relaxation tests. The aim of Figure 3 is to illustrate the possibility of calculating stress

relaxations within this framework for a specific set of parameters. When the stress relaxation starts after compressing the cylinder, HT creep controls the plastic flow at 350 °C and 500 °C, as shown in Figure 3c and Figure 3d at 0 s. As the strain rate rapidly decreases in both cases, lattice diffusion-controlled GBS becomes the dominant mechanism. At very low stresses and strain rates, Coble creep becomes the dominant mechanism at 500 °C. The total thermal stress contribution, σ_{ges}, of Equation (24) is named ”DYN” in Figure 3c and Figure 3d. The athermal stress contributions at the high temperatures and small strain rates (Equation (16)) are not significant due to a negligible amount of dislocation generation.

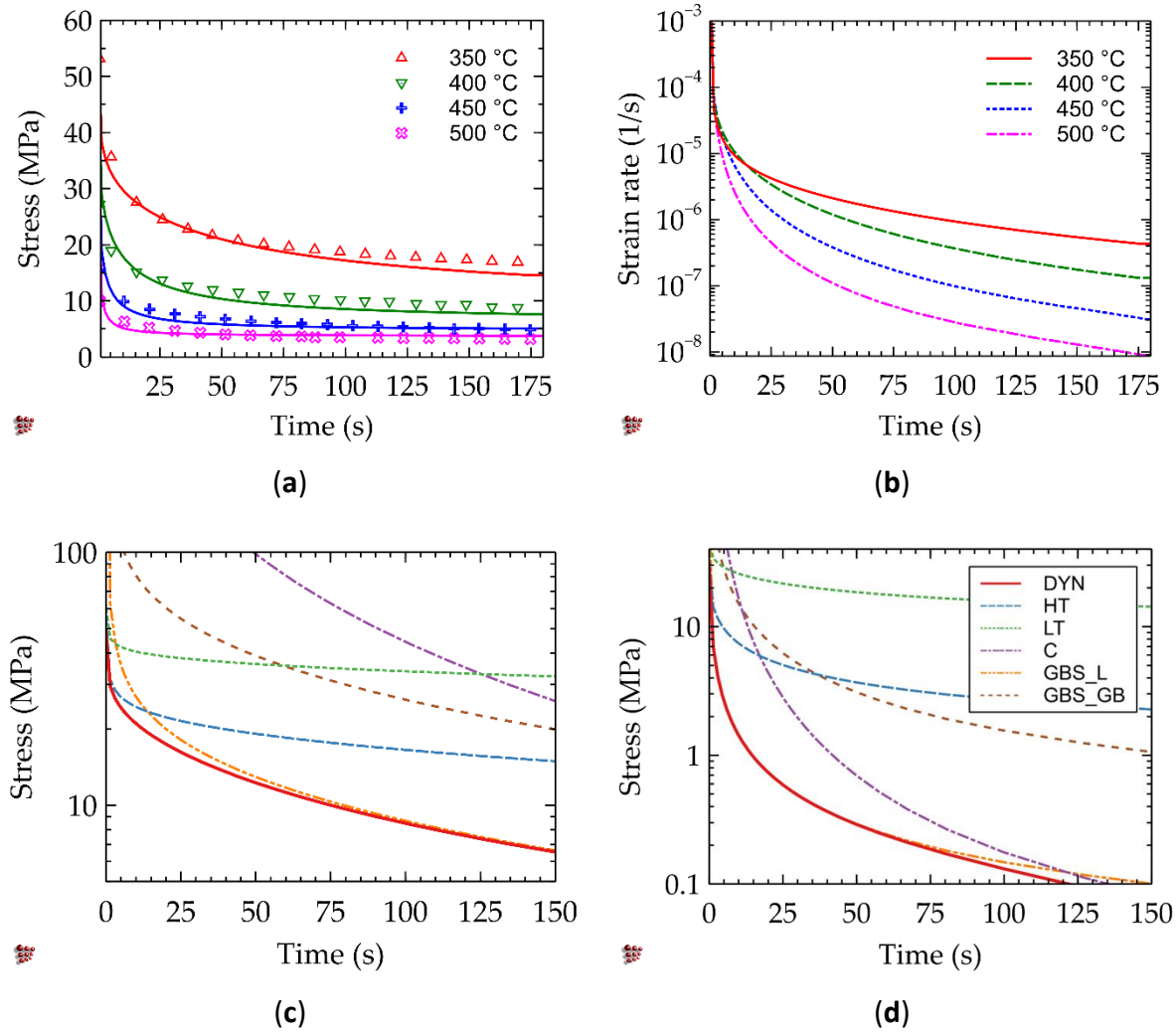

Figure 3. (**a**) Relaxation tests of an AlMg4.5Mn aluminium alloy at different temperatures. The solid lines are the simulations, whereas the symbols indicate the experimental results from [50]; (**b**) logarithmic strain rate reduction; logarithmic stress calculations of HT creep (HT), LT creep (LT), Coble creep, D_{gb}- and D_{l}-controlled GBS and the total thermal stress contribution (DYN) (**c**) at 350 °C and (**d**) at 500 °C.

An additional possible application of this framework is the construction of deformation maps, which provide information about the dominant deformation mechanism at specific temperatures and applied shear stresses. Figure 4 shows the calculated normalized stresses (σ/G) for different strain rates and temperatures in dependence of the grain diameter ((a) 5 µm, (b) 50 µm) for pure Al. Since grain rotation is not considered in the present work, application of the framework to sub-micrometer grain sizes might deliver inaccurate results (ultra-fine grained materials). The numbers in Figure 4 denote the corresponding deformation mechanisms and the black, bold lines indicate the transitions between the different deformation regimes.

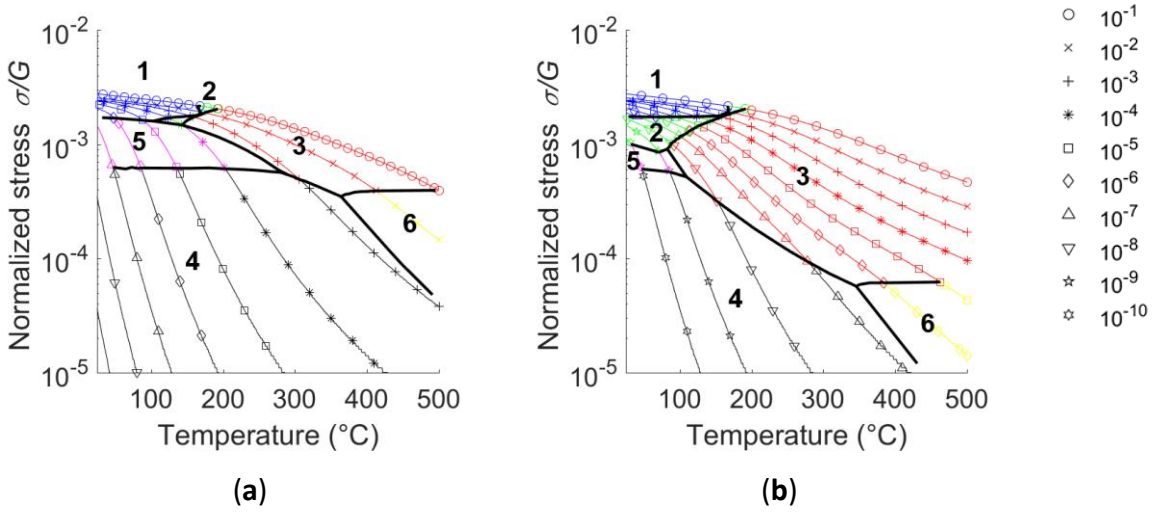

Figure 4. Exemplary deformation maps for pure Al. Normalized stress [-] for different temperatures and strain rates for (**a**) 5 µm and (**b**) 50 µm. The black, bold lines indicate transitions between the deformation regimes. The numbers indicate the dominant deformation mechanisms: dislocation glide (1); LT creep (2); HT creep (3); Coble creep (4); D_{gb}-controlled GBS (5) and D_{l}-controlled GBS (6).

Figure 4 shows representative deformation maps that have been generated without explicit calibration and thus they allow only for qualitative and exemplary analysis. In this sense, Figure 4a illustrates that GBS becomes the deformation-controlling mechanism at small grain sizes for a wide temperature range, which is in good agreement with literature [12]. Increasing GBS-fields are accompanied by shrinking LT creep and HT creep fields within the deformation maps. The dislocation density rapidly increases at high strain rates, leading to an increasing pipe diffusion coefficient, D_{C}, and a larger LT creep field (number 2). A detailed description of deformation maps and a catalogue of maps for various groups of materials are provided by

Frost and Ashby [20]. The effects of GBS on Frost–Ashby deformation maps are discussed in [12].

4. Conclusions

The implementation of creep mechanisms and their contributions to the stress response to an applied strain rate within an integrated framework for deformation modeling is discussed. Although, steady state is usually presumed for the secondary creep relations under no creep damage condition, athermal dislocation strengthening contribution and the mechanical threshold concept are considered. In the present framework, an integration of the influence of precipitates on the creep regimes is possible but was beyond the scope of this work. It is demonstrated that plastic flow is either governed by dislocation glide, diffusion of either vacancies or dislocations or by grain boundary sliding. The effective diffusion coefficient, which is influenced by pipe diffusion enhancement, excess vacancies or trapping effects, is accounted for. This new framework allows calculating the creep or plastic deformation behavior, while applying either a constant stress, stress relaxation after previous deformation or constant strain rate loading. Exemplary deformation maps for Al are calculated with the present model. Considering the microstructure evolution within a wide range of temperature and strain rate makes this framework suitable for many industrial applications, such as hot forming processes or strain relaxation during stress relieve annealing.

Author Contributions: Methodology, B.V.; software, B.V. and E.K.; investigation, B.V.; writing—original draft preparation, B.V.; writing—review and editing, E.K.; visualization, B.V.; supervision, E.K.;

Funding: This research received no external funding.

Acknowledgment: The authors acknowledge TU Wien Bibliothek for financial support through its Open Access Funding Program.

Conflicts of Interest: The authors declare no conflict of interest.

References

1 Ardell, A.J. Harper-Dorn creep—The dislocation network theory revisited. *Scr. Mater.* **2013**, *69*, 541–544.

2 Kumar, P.; Kassner, M.E.; Langdon, T.G. Fifty years of Harper-Dorn creep: A viable creep mechanism or a Californian artifact?. *J. Mater. Sci.* **2007**, *42*, 409–420.

3 Blum, W.; Maier, W. Harper-Dorn Creep - a Myth?. *Phys. Stat. Sol.* **1999**, *467*, 467–474.

4 Mohamed, F.A. Harper-Dorn creep: Controversy, requirements, and origin. *Mater. Sci. Eng. A* **2007**, *463*, 177–184.

5 Coble, R.L. A Model for Boundary Diffusion Controlled Creep in Polycrystalline Materials. *J. Appl. Phys.* **1963**, *34*, 1679–1682.

6 Herring, C. Diffusional viscosity of a polycrystalline solid. *J. Appl. Phys.* **1950**, *21*, 437–445.

7 Harper, J.G.; Shepard, L.A.; Dorn, J.E. Creep of aluminum under extremely small stresses. *Acta Metall.* **1958**, *6*, 509–518.

8 Yavari, P.; Miller, D.A.; Langdon, T.G. An investigation of harper-dorn creep-I. Mechanical and microstructural characteristics. *Acta Metall.* **1982**, *30*, 871–879.

9 Kassner, M.E.; Kumar, P.; Blum, W. Harper-Dorn creep. *Int. J. Plast.* **2007**, *23*, 980–1000.

10 Ruano, O.A.; Wadsworth, J.; Sherby, O.D. Harper-dorn creep in pure metals. *Acta Metall.* **1988**, *36*, 1117–1128.

11 Barrett, C.R.; Nix, W.D. High Temperature-Low Stress Creep of AI and AI + 0 . 5 % Fe. *Mater. Sci. Eng.* **1972**, *10*, 33–42.

12 Lüthy, H.; White, R.A.; Sherby, O.D. Grain boundary sliding and deformation mechanism maps. *Mater. Sci. Eng.* **1979**, *39*, 211–216.

13 Ruano, O.A.; Miller, A.K.; Sherby, O.D. The influence of pipe diffusion on the creep of fine-grained materials. *Mater. Sci. Eng.* **1981**, *51*, 9–16.

14 Hayden, H.W.; Floreen, S.; Goodell, P.D. Deformation mechanisms of superplasticity. *Met. Trans.* **1972**, *3*, 833–842.

15 Alden, T.H. The origin of superplasticity in the sn-5%bi alloy. *Acta Metall.* **1967**, *15*, 469–480.

16 Herriot, G.; Suery, M.; Baudelet, B. Superplastic behavior of the industrial Cu7wt.%P ALLOY. *Scr. Metall.* **1972**, *6*, 657–662.

17 Soliman, M.; Shan, Y.V.; Mendez-Martin, F.; Kozeschnik, E.; Palkowski, H. Strain Aging Characterization and Physical Modelling of Over-Aging in Dual Phase Steel. *Mater. Sci. Eng. A* **2020**, *788*, 139595.

18 Kocks, U.F. Laws for work hardening and low temperature creep.pdf. *J. Eng. Mater. Technol.* **1976**, *98*, 76–85.

19 Follansbee, P.S.; Kocks, U.F. A constitutive description of the deformation of copper based on the use of the mechanical threshold stress as an internal state variable. *Acta Metall.* **1988**, *36*, 81–93.

20 Frost, H.J.; Ashby, M.F. *Deformation-Mechanism Maps, The Plasticity and Creep of Metals and Ceramics*, 1st ed. Pergamon Press: Oxford, UK, 1982.

21 Schoeck, G. The Activation Energy of Dislocation Movement. *Phys. Stat. Sol.* **1965**, *8*, 499–507.

22 Argon, A.S. *Mechanical Properties of Single-Phase Crystalline Media: Deformation at Low Temperatures*, 4th, ed.; Elsevier B.V.: Amsterdam, The Netherlands, 1996.

23 Schulze, V.; Voehringer, O. Influence of Alloying Elements on the Strain Rate and Temperature Dependence of the Flow Stress of Steels. *Metall. Mater. Trans. A* **2000**, *31*, 825–830.

24 Kreyca, J.; Kozeschnik, E. State parameter-based constitutive modelling of stress strain curves in Al-Mg solid solutions. *Int. J. Plast.* **2018**, *103*, 67–80.

25 Walser, B.; Sherby, O.D. The Structure dependence of power law creep. *Scr. Metall.* **1982**, *16*, 213–219.

26 Brown, A.M.; Ashby, M.F. On the power-law creep equation. *Scr. Metall.* **1980**, *14*, 1297–1302.

27 Fischer, F.D.; Svoboda, J.; Kozeschnik, E. Interstitial diffusion in systems with multiple sorts of traps. *Model. Simul. Mater. Sci. Eng.* **2013**, *21*, 025008.

28 Fischer, F.D.; Svoboda, J.; Appel, F.; Kozeschnik, E. Modeling of excess vacancy annihilation at different types of sinks. *Acta Mater.* **2011**, *59*, 3463–3472.

29 Radis, R.; Kozeschnik, E. Numerical simulation of NbC precipitation in microalloyed steel. *Model. Simul. Mater. Sci. Eng.* **2012**, *20*, 055010.

30 Dutta, B.; Palmiere, E.J.; Sellars, C.M. Modelling the kinetics of strain induced precipitation in Nb microalloyed steels.pdf. *Acta Mater.* **2001**, *49*, 785–794.

31 Stechauner, G.; Kozeschnik, E. Assessment of substitutional self-diffusion along short-circuit paths in Al, Fe and Ni. *Calphad Comput. Coupling Phase Diagrams Thermochem.* **2014**, *47*, 92–99.

32 Jonas, J.J. The back stress in high temperature deformation. *Acta Metall.* **1969**, *17*, 397–405.

33 Wong, W.A.; Jonas, J.J. Aluminum Extrusion as a Thermally Activated Process. *Met. Soc. AIME Trans.* **1968**, *242*, 2271–2280.

34 Langdon, T.G.; Mohamed, F.A. A new type of deformation mechanism map for high-temperature creep. *Mater. Sci. Eng.* **1978**, *32*, 103–112.

35 Mohamed, F.A.; Langdon, T.G. Deformation Mechanism Maps Based on Grain Size. *Met. Trans.* **1974**, *5*, 2339–2345.

36 Maalekian, M.; Radis, R.; Militzer, M.; Moreau, A.; Poole, W.J. In situ measurement and modelling of austenite grain growth in a Ti/Nb microalloyed steel. *Acta Mater*. **2012**, *60*, 1015–1026.

37 Cha, S.C.; Hong, S.-H.; Kim, M.-Y.; Park, J.; Shim, J.-H.; Jung, W.-S.; Rath, M.; Kozeschnik, E. CALPHAD-based alloy design for advanced automotive steels—Part II: Compositional and microstructural modification for advanced carburizing steels. *Calphad Comput. Coupling Phase Diagrams Thermochem.* **2016**, *54*, 172–180.

38 Taylor, G.I. The Mechanism of Plastic Deformation of Crystals. Part I. *Theoretical. Proc. R. Soc. A Math. Phys. Eng. Sci.* **1934**, *145*, 362–387.

39 Sauzay, M.; Kubin, L.P. Scaling laws for dislocation microstructures in monotonic and cyclic deformation of fcc metals. *Prog. Mater. Sci*. **2011**, *56*, 725–784.

40 Buken, H.; Kozeschnik, E. State parameter-based modelling of microstructure evolution in micro-alloyed steel during hot forming. *IOP Conf. Ser. Mater. Sci. Eng.* **2016**, *119*, 012023.

41 Svoboda, J.; Fischer, F.D.; Fratzl, P.; Kozeschnik, E. Modelling of kinetics in multi-component multi-phase systems with spherical precipitates I: Theory. Mater. *Sci. Eng. A* **2004**, *385*, 166–174.

42 Kozeschnik, E.; Svoboda, J.; Fratzl, P.; Fischer, F.D. Modelling of kinetics in multi-component multi-phase systems with spherical precipitates II: Numerical solution and application. *Mater. Sci. Eng. A* **2004**, *385*, 157–165.

43 Kozeschnik, E.; Svoboda, J.; Fischer, F.D. Modified evolution equations for the precipitation kinetics of complex phases in multi-component systems. *Calphad Comput. Coupling Phase Diagrams Thermochem.* **2004**, *28*, 379–382.

44 Russell, K.C. Nucleation in solids: the induction and steady state effects. *Adv. Colloid Interface Sci.* **1980**, *13*, 205–318.

45 Kozeschnik, E. *Modeling Solid-State Precipitation*; Momentum Press, LLC: New York, NY, USA, 2013.

46 Ahmadi, M.R.; Povoden-Karadeniz, E.; Öksüz, K.I.; Falahati, A.; Kozeschnik, E. A model for precipitation strengthening in multi-particle systems. *Comput. Mater. Sci.* **2014**, *91*, 173–186.

47 Kreyca, F.J. *State Parameter based Modelling of Stress- Strain Curves in Aluminium Alloys*; TU Wien: Vienna, Austria, 2017.

48 Straub, S.; Blum, W. Does the natural third power law of steady state creep hold for pure aluminium. *Scr. Metall. Mater*. **1990**, *24*, 1837–1842.

49 Galindo-Nava, E.I.; Sietsma, J.; Rivera-Díaz-Del-Castillo, P.E.J. Dislocation annihilation in plastic deformation: II. Kocks-Mecking Analysis. *Acta Mater*. **2012**, *60*, 2615–2624.

50 Falkinger, G.; Simon, P. Static recovery of an AlMg4.5Mn aluminium alloy during multi-pass hot-rolling. *Procedia Eng.* **2017**, *207*, 31–36.

Journal Paper 2

Article

State Parameter-Based Yield Strength Model for Integration in Finite Element User-Material Routines

Bernhard Viernstein *, Tomasz Wojcik and Ernst Kozeschnik

Institute of Materials Science and Technology, TU Wien, Getreidemarkt 9, 1060 Vienna, Austria;

tomasz.wojcik@tuwien.ac.at (T.W.); ernst.kozeschnik@tuwien.ac.at (E.K.)

***** Correspondence: bernhard.viernstein@tuwien.ac.at; Tel.: +43-1-58801-308103

Abstract: A new state parameter-based user-subroutine for finite-element software packages, which can be used to simulate microstructure-dependent stress–strain relations, is presented. Well-established precipitation kinetics, strain hardening and strengthening models are brought into a condensed form to optimise computational efficiency, without losing their predictive capabilities. The framework includes main strengthening mechanisms, such as, precipitation strengthening, solid solution strengthening, the cross-core diffusion effect and work hardening. With the novel user-subroutine, the microstructure evolution of various thermo-mechanical treatments on the full integration point grid of the finite element (FE) mesh can be calculated. The validation of the simulations is carried out by mechanical testing as well as microstructure characterisation of an Al-6082 alloy, including transmission electron microscopy (TEM) investigations after various annealing times at 180 °C.

Keywords: finite element analysis; flow curve; aluminium alloy; user-materials subroutine

---

1. Introduction

The knowledge of residual stresses and distortions, which can be introduced into a workpiece during the manufacturing process, is essential for the optimisation of both, the design of the

components and the processing parameters. Since plasticity is dependent on the thermo-mechanical history of the material, the entire process chain, starting with solidification, must be taken into consideration for the simulation of temperature and strain rate-dependent stress evolution. An accurate material model is mandatory to relate flow stress to plastic strain. Many constitutive models were developed in the past decades, such as the Ludwik approach [1], the Voce type approach [2], the Johnson Cook model [3], Zerilli–Armstrong model [4], or the model of Khan and Huang [5]. Empirical material models or data table-based methods, which often describe experimental results but with limited physical meanings, are standard nowadays and they are included in most finite element analyses (FEA) tools. In contrast, advanced microstructure evolution models, which are, for instance, implemented in the MatCalc software package (http://matcalc.at, 12.07.2022), would lead to very long computing times and consume extensive computer memory, when included in FEA tools. FEA material models are presented in [6,7], which include strain hardening, recovery and recrystallisation, but do not consider precipitation kinetics or the evolution of excess vacancies. In the present paper, a mechanism- and state parameter-based model is introduced, which allows simulating the microstructure evolution in a metallic material during the manufacturing process and in-service conditions. In addition, the model allows for an extrapolation of these operating conditions, such as strain rate and temperature, while maintaining stable convergence behavior. Although the computation time can be up to twice as long as with typical standard models, a comprehensive microstructure description is provided, which gives insight into the underlying metallurgical processes that occur during the thermo-mechanical treatment.

A new user-subroutine, suitable for incorporation in commercial FEA-software packages, is presented in the first part of this work, which is called ‘simple MicroStructure Evolution’ (sMSE) model in the following. The sMSE model is based on the mechanical threshold concept and an extended Kocks–Mecking approach, which allows to calculate the evolution of the average dislocation density during thermo-mechanical treatments. With the temperature and strain rate profiles given from the finite element software, the sMSE materials subroutine returns local yield stresses as well as the corresponding derivatives with respect to strain and strain rate back to the finite element software.

The second part of the paper illustrates the application of this new framework to the simulation of flow curves in a precipitation-hardenable Al-6082 alloy in dependence of the

particular heat treatment condition. For this task, efficient models of precipitate nucleation and growth are included, which are an important component of the microstructure evolution beside the average dislocation density evolution. The work is, finally, experimentally validated by compression tests and electron microscopy investigations. The new framework conveniently balances low calculation time, which allows to simulate residual stresses of complex components, such as cylinder heads, and the evolution of physically based material properties on the full integration point grid of the FE-mesh.

2. The Model

The strength model consists of an athermal stress contribution σ_{ath} (see Section 2.1) and a thermally activated stress contribution σ_{th} (see Section 2.2). σ_{ath} is caused by forest dislocations and is expressed as an average dislocation density as formulated in an extended Kocks–Mecking approach [8]. σ_{th} includes strengthening mechanisms, such as, solid solution strengthening, precipitation strengthening, the cross-core diffusion effect and grain boundary strengthening in the mechanical threshold framework. The total stress contribution σ is given as a function of temperature T, strain rate $\dot{\varepsilon}$ and the vector of state parameter-based coefficients $\boldsymbol{\chi}$, which can include the concentration of the alloying elements in the matrix, the radius and number density of precipitates or the dislocation density, for instance.

$$\sigma = \sigma(T,\dot{\varepsilon},\boldsymbol{\chi}) \tag{1}$$

Adaptions of original models from literature are introduced for a suitable integration into the user-subroutine in FE simulations. Grain growth and recrystallisation effects are not included, because precipitation strengthening, and work hardening are the dominant mechanisms in the present experimental set up. Since a 6082 Al alloy is investigated, the model is introduced for an Al matrix with the two main alloying elements Mg and Si. Extension to higher-order systems is straightforward but not explicitly elaborated, here.

2.1. Athermal Stress Contribution

An extended one-parameter model of Kocks and Mecking is used to calculate the temperature and strain rate-dependent dislocation density evolution [8,9]

$$\frac{d\rho}{d\varepsilon} = \frac{d\rho^{+}}{d\varepsilon} + \frac{d\rho^{-}}{d\varepsilon} + \frac{d\rho_{s}^{-}}{d\varepsilon} = \frac{M}{b \cdot A}\sqrt{\rho} - 2 \cdot B \cdot M \frac{d_{crit}}{b}\rho - 2 \cdot C \cdot D_{d} \frac{Gb^{3}}{\dot{\varepsilon} k_{B} T}\left(\rho^{2} - \rho_{eq}^{2}\right) \tag{2}$$

M is the Taylor factor, *b* is the Burger's vector, k_{B} is the Boltzmann constant, *G* is the shear modulus, *A*, *B* and *C* are temperature and strain rate-dependent coefficients. Kreyca et al. [8] related the coefficients *A*, *B* and *C* to the initial hardening rate θ_0 and the saturation stress σ_∞. d_{crit} is the critical annihilation distance between two dislocations of opposite sign of the Burgers' vector [10] and ρ_{eq} is the equilibrium dislocation density. $\frac{\mathrm{d}\rho^+}{\mathrm{d}\varepsilon}$ represents the dislocation generation rate, which is inversely proportional to the current mean distance between dislocations and the total dislocation density, ρ. $\frac{\mathrm{d}\rho^-}{\mathrm{d}\varepsilon}$ and $\frac{\mathrm{d}\rho_s^-}{\mathrm{d}\varepsilon}$ take into account the annihilation of dislocations by cross slip processes and vacancy-assisted climb, respectively. The first annihilation term describes dynamic recovery processes at low and medium temperatures, whereas the second term represents static recovery at elevated temperatures. The latter quantity is marked by the subscript s. For each time integration interval Δt, the average dislocation density ρ is correlated with the athermal plastic stress contribution by the Taylor equation [11,12] with

$$\sigma_{\mathrm{p}} = \alpha \cdot M \cdot b \cdot G \cdot \sqrt{\rho} \tag{3}$$

where α is the strengthening coefficient. Further details on the implementation of the athermal strength framework are described in [13].

2.2. Thermal Stress Contributions

Many state parameter-based yield strength models capture the influence of temperature and strain rate on plastic deformation of polycrystalline materials in various ways [14–23]. One example is given in [8], where a low temperature and a high temperature part can be distinguished, labelled by 'lt' and 'ht' in the following. When dislocation motion is characterised by glide processes, the stress can be expressed as

$$\sigma_{\mathrm{lt}} = \hat{\tau} \cdot \exp\left(\frac{-k_{\mathrm{B}} \cdot T}{\Delta F_{\sigma_0}^{\mathrm{lt}}} \cdot \ln\left(\frac{\dot{\varepsilon}_0}{\dot{\varepsilon}}\right)\right) \tag{4}$$

where the subscript $'\sigma_0'$ refers to the initial yield stress, $\dot{\varepsilon}_0$ is a constant and $\hat{\tau}$ is the mechanical threshold, defined by the sum of a basic stress, solid solution hardening (see Section 2.2.1), cross core diffusion hardening (Section 2.2.2), grain size hardening, sub-grain size hardening and precipitation hardening (Section 2.2.3) in the absence of thermal activation.

When dislocation climb becomes dominant at high temperatures, the following stress contribution can be used [8]

$$\sigma_{\mathrm{ht}} = \left(\hat{t} \cdot \frac{\dot{\varepsilon}^{*} \cdot k_{\mathrm{B}} \cdot T \cdot (\alpha \cdot b \cdot G)^{2}}{2bc\Delta F_{\sigma_0}^{\mathrm{ht}} \cdot \exp\left(-\frac{\Delta F_{\sigma_0}^{\mathrm{ht}}}{k_{\mathrm{B}} T}\right)} \right)^{\frac{1}{n}} \tag{5}$$

c is the speed of sound, and the exponent *n* of the power law equation varies between 3 and 10 [24]. The true strain rate is modified in the present framework by the exponent $n_{\dot{\varepsilon}}$ to reduce the strain rate dependency with $\dot{\varepsilon}^{*} = \dot{\varepsilon}^{n_{\dot{\varepsilon}}}$. The activation energies $\Delta F_{\sigma_0}^{\mathrm{lt}}$ and $\Delta F_{\sigma_0}^{\mathrm{ht}}$ depend on the effective solute concentrations in the matrix [25–28], which vary due to the cross-core diffusion effect and by the nucleation and growth of precipitates (see Section 2.3). The total thermal stress σ_0 is evaluated by the summation rule according to

$$\sigma_0 = \left(\left(\frac{1}{\sigma_{\mathrm{lt}}}\right)^{n_{\mathrm{c}}} + \left(\frac{1}{\sigma_{\mathrm{ht}}}\right)^{n_{\mathrm{c}}} \right)^{\frac{1}{n_{\mathrm{c}}}} \tag{6}$$

where n_{c} is a coupling coefficient.

The overall temperature- and strain rate-dependent stress response at an applied constant strain rate $\dot{\varepsilon}$ is given by the summation of the athermal stress contribution σ_{p} of Equation (3) and the thermal stress contribution σ_0 of Equation (6).

2.2.1. Solid Solution Hardening

To incorporate the solid solution strengthening contribution into the present framework, the following equation is utilized, based on the Labusch approach [29]

$$\sigma_{\mathrm{SS}} = \left(\sum_i \left(k_i c_i^{\frac{2}{3}} \right)^{n_{\mathrm{SS}}} \right)^{\frac{1}{n_{\mathrm{SS}}}} \tag{7}$$

The subscript ‘SS’ refers to solid solution and the sum is taken over all alloying elements, *i*. The contribution of the alloying elements with the concentrations c_i are calculated separately and summed up, using the exponent n_{SS}. k_i is defined by

$$k_i = \left(\frac{{f_{\max}}^{4} \cdot w}{8 \cdot E_{\mathrm{L}} \cdot b^{7}} \right)^{\frac{1}{3}} \tag{8}$$

$f_{\max}$ is the maximum interaction force between the solutes and the dislocations, which is defined by [29]

$$f_{\max} = \frac{\sqrt{3}}{2} \cdot \left(\frac{1+\nu}{1-\nu}\right) G b^2 |\varepsilon_m| \tag{9}$$

$w = 5b$ is the interaction distance and the dislocation line tension $E_{\mathrm{L}} = \frac{1}{2} \cdot G \cdot b^2$ [30]. ν is the Poisson's ratio and ε_{m} is the misfit strain between solute and matrix atoms.

2.2.2. Cross-Core Diffusion Hardening

Dynamic strain aging (DSA) phenomena occur by the interaction of diffusing solutes with the stress fields of dislocations and retard the ongoing dislocation motion. Since the possible negative strain rate sensitivity can lead to plastic material instabilities due to local material softening, it plays a key role in material processing [31]. A well-known example for DSA is the Portevin–LeChatelier effect, which manifests itself in serrated stress–strain behavior. In the sMSE framework, the cross-core diffusion effect is included as developed by Curtin et al. [31]. The model is based on single atomic jumps of solutes from the compression side to the tension side in the core of a dislocation, leading to the additional strain rate-dependent strengthening [31] as

$$\Delta\tau_{\mathrm{s}}(\dot{\varepsilon}) = \alpha \left(\frac{2c_0\overline{\Delta W}}{\sqrt{3}b^3}\right) \tanh\left(\frac{\overline{\Delta W}}{2k_{\mathrm{B}}T}\right) \left[1 - e^{-6\cosh\left(\frac{\overline{\Delta W}}{2k_{\mathrm{B}}T}\right) \mathrm{r_c} \frac{\Omega}{\dot{\varepsilon}}}\right] \tag{10}$$

$\alpha = 0.56$, c_0 is the bulk solute concentration in each iteration step, $\overline{\Delta W}$ is the average binding energy difference between the core compression and tension sites, Ω is a constant in this framework, $\mathrm{r_c}$ is the reference core transition rate with

$$\mathrm{r_c} = \nu_0 e^{\frac{-\Delta H_{\mathrm{c}}}{k_{\mathrm{B}}T}} \tag{11}$$

where ν_0 is the attempt frequency and ΔH_{c} is the average activation enthalpy for transitions from tension to compression and vice versa. Generally, higher temperatures and smaller strain rates lead to more diffusion and, consequently, to higher cross-core diffusion strengthening. The effective concentration of solutes on the tension side of a dislocation core is calculated as [31]

$$c_{\mathrm{eff}} = c_0 + c_0 \tanh\left(\frac{\overline{\Delta W}}{2k_{\mathrm{B}}T}\right) \left[1 - e^{-6\cosh\left(\frac{\overline{\Delta W}}{2k_{\mathrm{B}}T}\right) \mathrm{r_c} \frac{\Omega}{\dot{\varepsilon}}}\right]. \tag{12}$$

Continuous changes of the effective concentration c_{eff} influences the strengthening contribution $\Delta\tau_{\mathrm{s}}$, which is linearly superimposed to the mechanical threshold. The cross-core diffusion effect is directly included to the sMSE framework without any simplification.

2.2.3. Precipitation Hardening

Obstacles within a material, such as precipitates, can hinder dislocation motion and thus lead to an increased strength of the material. In general, small and coherent precipitates can be sheared by dislocations, whereas, above a certain critical size, a transition to bypassing and formation of dislocation loops around the precipitates occurs. In the following, the stress contribution based on the Orowan dislocation looping mechanism [32], as well as the shearing mechanism is outlined and the equations, which are implemented in the sMSE framework, are presented. The mechanism, which delivers the least contribution to the total stress, is assumed to be the operative one and it is labelled σ_{prec} in the following. For simplification, no distinction between weak and strong precipitates is included, as described in detail, for instance, in [33].

The interaction of dislocations and non-shearable precipitates was first described by Orowan [32] and later modified by Ashby [34], Brown and Ham [35], and Ardell [36]. The implemented equations are taken from Ahmadi [33], based on the original Orowan model. The subscript 'O' is used subsequently and the Orowan strength is taken as

$$\sigma_{\mathrm{O}} = \frac{C_{\mathrm{O}} \cdot G \cdot b \cdot M}{2 \cdot \pi \cdot L_{\mathrm{S}}} \cdot \log\left(\frac{R_{\mathrm{eq}}}{2 \cdot b}\right) \tag{13}$$

where C_{O} is the precipitation strengthening coefficient and L_{S} is the mean distance between two equally sized spherical precipitate surfaces with [37]

$$L_{\mathrm{S}} = \sqrt{\frac{\ln(3)}{2 \cdot \pi \cdot N \cdot r} + \frac{8}{3} r^2} - \sqrt{\frac{8}{3}} r \tag{14}$$

N is the number density and *r* is the radius of the precipitate; the evolution equations are given in Section 2.3. The equivalent radius R_{eq} in Equation (13) describes the precipitate-dislocation interference area with

$$R_{\mathrm{eq}} = \frac{\pi}{4} \cdot r \tag{15}$$

To avoid negative values for the Orowan contribution, the equivalent radius has a minimum value of 4·*b*.

The shearing mechanisms involve the coherency effect, the modulus effect, the stacking fault effect and the interfacial effect. For simplicity, only the coherency effect, which provides the largest strengthening contribution in many practical applications, is included in the present framework. The coherency effect is based on the interaction of the elastic strain field, which is caused by the difference between the molar volumes of matrix and the precipitate, with a moving dislocation [33]. The stress contribution for coherency strengthening is given as

$$\sigma_{\mathrm{Coh}} = \frac{1.3416\cos(\theta)^2 + 4.1127\sin(\theta)^2}{L_{\mathrm{S}}} \cdot \left(\frac{G^3 \cdot \varepsilon^3 \cdot R_{\mathrm{eq}}^3 \cdot b}{E_{\mathrm{L}}}\right)^{\frac{1}{2}} \cdot M \cdot C_{\mathrm{Coh}} \tag{16}$$

where θ is the angle between dislocation line and its Burgers vector. $\theta = 0$ for pure screw dislocations and $\theta = \frac{\pi}{2}$ for pure edge dislocations. In the present treatment, $\theta = \frac{\pi}{4}$ is taken as a mean value. The linear misfit ε is approximated as $\frac{1}{3}$ of the volumetric misfit. C_{Coh} is the precipitation strengthening coefficient, which is a calibration parameter.

2.3. Precipitation Kinetics Model

Supersaturated states are unstable since a driving force exists to minimize the Gibbs free energy by the formation of a new phase, rearrangement of existing phases or redistribution of alloying constituents. For the evolution of the precipitate microstructure, the SFFK model [38–40] can be utilized, which is, for instance, implemented in the MatCalc software package (http://matcalc.at, 12.07.2022). However, these models need to be simplified to minimise both, the calculation time as well as the memory resources, within an FE framework. To determine the driving force for nucleation of precipitates, the knowledge of the equilibrium concentrations of Mg and Si in the Al matrix can be taken as a starting point. X_{Mg}^{0} and X_{Si}^{0} are the nominal Mg and Si mole fractions in the system and $X_{\mathrm{Mg}}^{\mathrm{p}}$ and $X_{\mathrm{Si}}^{\mathrm{p}}$ are the Mg and Si fractions inside the precipitates. The following description is given for one specific precipitation phase, e.g., clusters or the *θ*″ phase, but the extension to a multi-phase system is straightforward. The Mg and Si concentrations in equilibrium within the fcc Al matrix is given by mass conservation.

$$X_{\mathrm{Mg}}^{\mathrm{fcc\_eq}} = X_{\mathrm{Mg}}^{0} - X_{\mathrm{Mg}}^{\mathrm{p}} \cdot f_{\mathrm{eq}} \tag{17}$$

$$X_{\mathrm{Si}}^{\mathrm{fcc\_eq}} = X_{\mathrm{Si}}^{0} - X_{\mathrm{Si}}^{\mathrm{p}} \cdot f_{\mathrm{eq}} \tag{18}$$

f_{eq} is the equilibrium phase fraction of the precipitate, which is calculated by solving the following solubility product by numerical methods

$$X_{\mathrm{Mg}}^{\mathrm{p}} \cdot \log\left(X_{\mathrm{Mg}}^{\mathrm{fcc\_eq}}\right) + X_{\mathrm{Si}}^{\mathrm{p}} \cdot \log\left(X_{\mathrm{Si}}^{\mathrm{fcc\_eq}}\right) - \Delta G = 0 \tag{19}$$

where ΔG is the energy of (precipitate) dissolution normalized with respect to *RT*

$$\Delta G = \frac{C}{T} + D \tag{20}$$

C and *D* are input parameters within the sMSE framework. In contrast to classical precipitation calculations based on, e.g., the CALPHAD method, no thermodynamic databases are used in the sMSE framework, and the driving force is calibrated by the parameters C and *D*. The molar driving force for precipitation nucleation is approximated with

$$d_{\mathrm{m}} = R \cdot T \cdot \left(X_{\mathrm{Mg}}^{\mathrm{p}} \cdot \log\left(\frac{X_{\mathrm{Mg}}^{\mathrm{fcc}}}{X_{\mathrm{Mg}}^{\mathrm{fcc\_eq}}}\right) + X_{\mathrm{Si}}^{\mathrm{p}} \cdot \log\left(\frac{X_{\mathrm{Si}}^{\mathrm{fcc}}}{X_{\mathrm{Si}}^{\mathrm{fcc\_eq}}}\right)\right). \tag{21}$$

The nucleation of new precipitates can be evaluated on the basis of the steady-state nucleation rate, which is defined as the number of newly formed precipitate nuclei per unit volume and unit time as [41,42]

$$J = N_0 \cdot Z \cdot \beta^* \cdot e^{\frac{-G^*}{k_{\mathrm{B}} T}} \tag{22}$$

where N_0 is the number of available nucleation sites, Z is the Zeldovich factor, β^* is the atomic attachment rate and G^* is the critical nucleation energy. The Zeldovich factor is expressed as [41,43],

$$Z = \left(\frac{b^6}{64\pi^2 k_{\mathrm{B}} T} \frac{\left(\frac{d_{\mathrm{m}}}{v^{\alpha}}\right)^4}{\gamma^3} \right)^{\frac{1}{2}} \tag{23}$$

v^{α} represents the molar volume of the precipitate. In this simplified framework, an average molar volume of 10^{-6} $[\mathrm{m}^3/\mathrm{mol}]$ is assumed for all phases. γ is the specific interfacial energy. The critical nucleation energy is given by

$$G^* = \frac{16\pi}{3} \frac{\gamma^3}{\left(\frac{d_{\mathrm{m}}}{v^{\alpha}}\right)^2} \tag{24}$$

The atomic attachment rate reads

$$\beta^* = \frac{4\pi {r_{\mathrm{crit}}}^2}{b^4} D_{\mathrm{eff}} \tag{25}$$

with the critical radius

$$r_{\mathrm{crit}} = \frac{2\gamma}{\frac{d_{\mathrm{m}}}{\nu^{\alpha}}} \tag{26}$$

The effective diffusion coefficient D_{eff} is taken as

$$D_{\mathrm{eff}} = D_0 \cdot \exp\left(\frac{-Q}{R \cdot T}\right) \cdot \left(\frac{X_{\mathrm{Va}}}{X_{\mathrm{Va,eq}}}\right) \tag{27}$$

D_0 is the pre-exponential factor, Q is the activation energy for diffusion, X_{Va} is the current vacancy concentration and $X_{\mathrm{Va,eq}}$ is the equilibrium vacancy concentration. The evolution of quenched-in vacancies is described on the basis of the FSAK-model [44], which considers the formation and annihilation of vacancies at grain boundaries, dislocation jogs or Frank loops.
The change of mean radius in each time step due to precipitate growth is evaluated from the original SFFK treatment by solving the evolution equations for a single diffusing species and under the assumption that the precipitate is a stoichiometric compound. The rate of the radius due to particle growth, $\dot{r}_{\mathrm{g}}$, is then obtained with

$$\dot{r}_{\mathrm{g}} = \frac{d_{\mathrm{m}}}{RTr} \cdot D_{\mathrm{eff}} \tag{28}$$

After the growth of precipitates has seized due to decreasing supersaturation, further growth of large particles commences at the expense of the smaller particles. This so-called coarsening process occurs with continuously increasing mean radius of the precipitates and a simultaneous decrease of their number density. The radius change due to coarsening in the classical LSW mean-field approximation reads

$$\dot{r}_{\mathrm{LSW}} = \frac{1}{3r^2} \cdot K_{\mathrm{LSW}} \tag{29}$$

where the subscript ‘LSW’ refers to the original work of Lifshitz and Slyozov [45] and Wagner [46]. The coarsening rate constant is obtained as [47],

$$K_{\mathrm{LSW}} = \frac{8\gamma\nu^{\alpha}}{9RT} \frac{D_{\mathrm{eff}} \cdot \eta_{\mathrm{LSW\_fact}}}{\left(\frac{\left(X_{\mathrm{Mg}}^{\mathrm{p1}} - X_{\mathrm{Mg}}^{0}\right)^2}{X_{\mathrm{Mg}}^{0}} + \frac{\left(X_{\mathrm{Si}}^{\mathrm{p1}} - X_{\mathrm{Si}}^{0}\right)^2}{X_{\mathrm{Si}}^{0}}\right)} \tag{30}$$

where the effective diffusion coefficient D_{eff} is used in this framework and $\eta_{\mathrm{LSW\_fact}}$ is a fitting parameter.

2.4. State-Dependent Variables

For each time integration step *dt*, the evolution of the vector of state parameters, $\boldsymbol{\chi}$, is calculated within the subroutine. Table 1 assigns all state dependent variables to either thermal or athermal stress. The final stress $\sigma(T,\dot{\varepsilon},\boldsymbol{\chi})$ is then calculated by the sum of σ_{th} and σ_{at}.

Table 1. Assignment of all state variables to thermally activated σ_{th} and athermal σ_{at}.

Name	$\boldsymbol{\sigma_{\mathrm{th}}}$	$\boldsymbol{\sigma_{\mathrm{at}}}$
Mg concentration within the fcc Al matrix $X_{\mathrm{Mg}}^{\mathrm{fcc}}$	x	
Si concentration within the fcc Al matrix $X_{\mathrm{Si}}^{\mathrm{fcc}}$	x	
Current vacancy concentration X_{Va}	x	
Number density of precipitates *N*	x	
Radius of precipitates *r*	x	
Dislocation density ρ		x

Figure 1 shows a flow chart of a FEA solution procedure, where the input parameters are *T*, $\dot{\varepsilon}$ and Δt. The temperature gradient, $\dot{T}$, is not provided by all FEA software, which is why it is written in brackets. The state parameters are updated every time the final iteration step is performed. σ, $\frac{d\sigma}{d\varepsilon}$ and $\frac{d\sigma}{d\dot{\varepsilon}}$ are returned every time the materials subroutine is called by the FEA program.

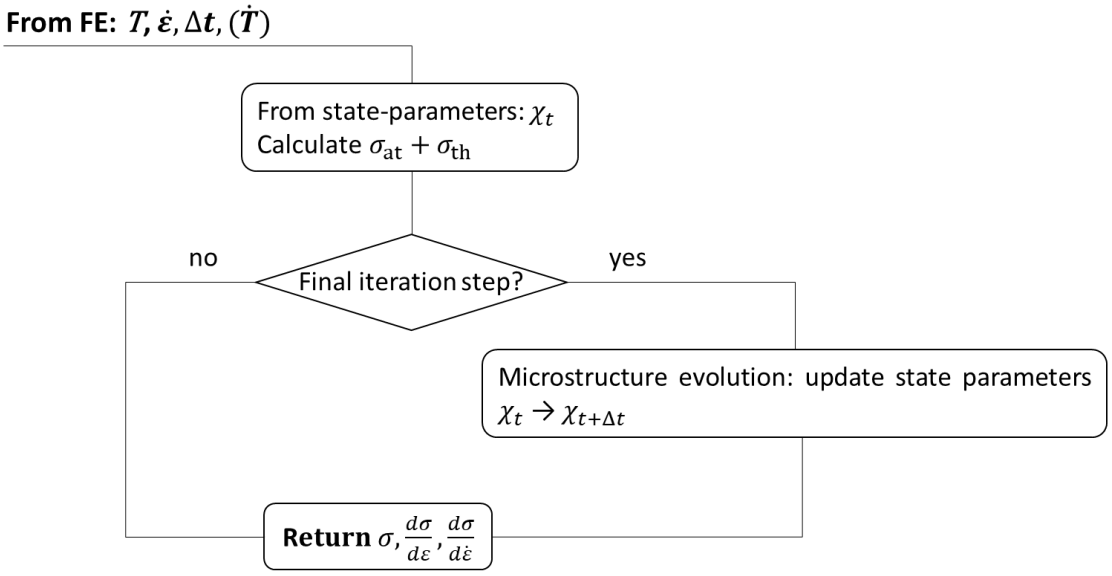

Figure 1. Flow chart of an FEA procedure, indicating the update of the state parameters after the final iteration step *Dt*.

3. Experimental

3.1. Material and Heat Treatment

The process of parameter identification and calibration of the present model is divided into two parts: (i) analysis of the nucleation and growth kinetics of precipitates during artificial aging, and (ii) characterisation of the work hardening behavior evaluated with compression tests. The chemical composition of the commercial AA6082 aluminium alloy, which is used in the present experiments, is given in Table 2.

Table 2. Composition of alloy AA6082 in wt%.

Alloy	Al	Si	Mg	Cu	Fe	Mn	Cr	Ti	Zn	V
AA6082	bal.	1.22	0.861	0.083	0.254	0.640	0.184	0.026	0.021	0.0105

After die-casting, the material is homogenised at 560 °C for 2 h, which represents the as-received state for the investigations. The specimens are then solution heat treated at 560 °C for 50 min in a circulating air furnace (Carbolite Type 3508), water-quenched and artificially aged in an oil bath between 0.5 h and 8 h for the first experimental setup (i). Between the solid solution heat treatment and the artificial aging (ii), the material remained at RT for 20 min.

3.2. Mechanical Testing

The compression tests are carried out in a high-speed quenching and deformation dilatometer DIL 805 A/D. Cylindrical specimens with lengths of 10 mm and diameters of 5 mm are produced from the as-received state. Prior to the deformation step, the specimens are solution heat treated at 530 °C for 5 min and helium-cooled with a cooling rate of 50 K/s to the deformation temperatures (25, 100, 200, 300, 400 and 500 °C), where they are held for 10 s to achieve sufficient thermal equilibration. Each deformation test is repeated at least twice with applied true strain rates of 0.1 s^{-1} and 1 s^{-1}.

Brinell hardness measurements (HBW 1/10) are carried out in an EMCO-Test M1C 010 unit, where at least eight measurements are performed for each aging time.

3.3. Electron Microscopy

Transmission electron microscopy (TEM) is applied for microstructure characterisation. The specimens are ground with SiC-papers until a thickness of approximately 0.1 mm is achieved. Subsequently, discs of 3 mm in diameter are punched out and electrochemically etched using a Struers Tenupol-5 in order to obtain electron-transparent regions. This process is carried out in a 2:1 mixture of methanol and nitric acid at temperatures between −20 °C and −10 °C applying a polishing voltage of 10 V. The analysis is performed on an FEI TECNAI F20 microscope equipped with a field emission gun and operated at 200 kV acceleration voltage. Bright field images in <001>Al zone axis reveal the lengths of the needle-shaped precipitates, whereas precipitate diameters are estimated using high-resolution transmission electron microscopy (HRTEM). The thickness of the observed regions is measured by electron energy loss spectrometry (EELS) using the t/λ (log-ratio) methodology [48]. Upon data collection, average lengths, diameters, and number densities of the precipitates are estimated.

4. Simulation

To demonstrate the potential of the present state parameter-based concept, all simulations are conducted on the basis of one single set of input parameters. Table 3 summarises all input parameters for the precipitation kinetics calculation as described in Section 2.3. The parameters are calibrated on the precipitation statistics determined by TEM. In this setup, only one precipitate type is listed, since only β'' precipitates are detected in TEM during the deformation tests. Although a second precipitate type is available for simulation in the sMSE

framework, only the observed β'' is accounted for in the following example according to experimental evidence.

Table 3. Input parameters for the precipitation kinetics simulation as described in Section 2.3.

Symbol	Name	Unit	Value	Equation	Source
$X_{\mathrm{Mg}}^{\mathrm{p}}$	Stoichiometry: Mg_5Si_6 (β'')	-	5/11	(17), (19)	[49]
$X_{\mathrm{Si}}^{\mathrm{p}}$	Stoichiometry: Mg_5Si_6 (β'')	-	6/11	(18), (19)	[49]
C	Normalized driving force calibration parameter	K	−950	(20)	This work
D	Normalized driving force calibration parameter	-	−3.35	(20)	This work
N_0	Number of available nucleation sites	$1/\mathrm{m}^3$	10^{28}	(22)	(MatCalc)
γ	Specific interfacial energy	$\mathrm{J/m}^2$	0.09	(23), (24), (30)	This work
D_0	Pre-exponential factor for diffusion	m^2/s	3×10^{-8}	(27)	This work
Q	Activation energy for diffusion	$\mathrm{J/mol}$	119,000	(27)	This work
$\eta_{\mathrm{LSW\_fact}}$	LSW coarsening factor	-	1	(30)	This work
h	Shape parameter of β''	-	5	(32)	This work

Table 4 lists the input parameters for the strengthening models, which are described in Sections 2.1 and 2.2. The parameters are calibrated on basis of the flow curves obtained in the compression tests. Since precipitation strengthening significantly impacts the yield stress, calibration of the precipitation kinetic models is carried out prior to the calibration of the work hardening models.

Table 4. All input parameters for the strengthening models as described in Sections 2.1 and 2.2.

Symbol	Name	Unit	Value	Equation	Source
M	Taylor factor	-	3.06	(2), (3), (13), (16)	[50]
b	Burger's vector	m	2.86×10^{-10}	(2), (3), (5), (9), (13), (16)	[24]
G	Shear modulus	MPa	29,438.4–15.052·T	(2), (3), (5), (9), (13), (16)	[23]
α	Strengthening coefficient	-	0.34	(3), (5)	[12],[51,52]
ρ_0	Initial dislocation density	$\mathrm{m/m}^3$	10^{11}	(4)	(MatCalc)
c	Speed of sound	m/s	5100	(4), (5)	[23]
$\dot{\varepsilon}_0$	Constant	1/s	$\rho_0 \cdot c \cdot b$	(4)	[23]
σ_{basic}	Basic stress	MPa	120	(4), (5)	This work
$\Delta F_{\sigma 0}^{\mathrm{lt}}$	Low temperature activation energy	J	$0.75 \cdot G \cdot b^3$	(4)	This work

$\Delta F_{\sigma 0}^{\mathrm{ht}}$	High temperature activation energy	kJ/mol	130	(5)	This work
$n_{\dot{\varepsilon}}$	Strain rate exponent	-	0.5	(5)	This work
n	Power law exponent	-	3	(5)	This work
n_{c}	Low and high temperature coupling coefficient	-	2	(6)	This work
n_{ss}	Solid solution coupling exponent	-	1.8	(7)	(MatCalc)
ν	Poisson's ratio	-	0.347	(9)	[53]
$\varepsilon_{\mathrm{m\_Mg}}$	Misfit-strain for Mg	-	0.0123	(9)	[54]
$\varepsilon_{\mathrm{m\_Si}}$	Misfit-strain for Si	-	0.0074	(9)	[54]
$\overline{\Delta W}$	Average binding energy difference	J	2.08×10^{-20}	(10), (12)	[31]
Ω	constant	-	0.00063	(10), (12)	[31]
ν_0	Attempt frequency	s^{-1}	3.8×10^{13}	(11)	[55]
ΔH_{c}	Activation enthalpy for transitions from tension to compression	J	1.55×10^{-19}	(11)	[31]
C_{O}	Precipitation strengthening coefficient for the Orowan mechanism	-	5	(13)	This work
C_{Coh}	Precipitation strengthening coefficient for the coherency effect	-	1	(16)	This work
ν^*	Volumetric misfit	-	0.05	(16)	This work
$\Delta F_{\theta_0}^{\mathrm{lt}}$	Low temperature activation energy for strain hardening rate θ	kJ/mol	700	[8]	This work
$\Delta F_{\theta_0}^{\mathrm{ht}}$	High temperature activation energy for strain hardening rate θ	kJ/mol	75	[8]	This work
$\Delta F_{\sigma_{\mathrm{sat}}}^{\mathrm{lt}}$	Low temperature activation energy for saturation stress σ_{sat}	J	$0.3 \cdot G \cdot b^3$	[8]	This work
$\Delta F_{\sigma_{\mathrm{sat}}}^{\mathrm{ht}}$	High temperature activation energy for saturation stress σ_{sat}	kJ/mol	110	[8]	This work
β_1	Flow stress correction factor for low strains	-	35	[13]	This work
β_2	Flow stress correction factor for low strains	-	0.625	[13]	This work
β_{exp}	Flow stress correction exponent for low strains	-	2.5	[13]	This work

5. Results and Discussion

5.1. Hardness Tests

The experimentally observed hardness curve for artificial aging at 180 °C is shown in Figure 2. The hardness rapidly increases until a peak is reached after approximately 8 h. Afterwards, the hardness decreases again due to overaging (coarsening) of the β'' precipitates. In addition, β'', which is assumed to be the main hardening phase in the 6xxx series alloys [49], transforms into β'. The latter process is not considered in the present analysis, though.

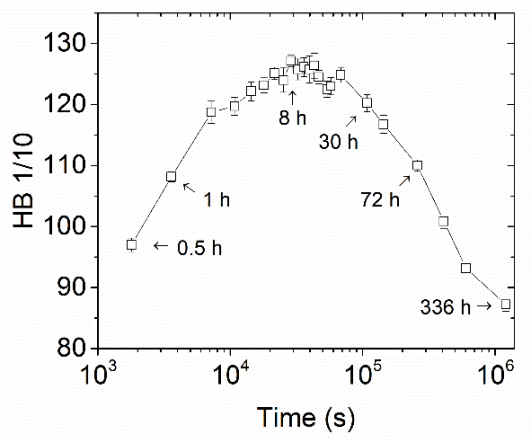

Figure 2. Brinell hardness as a function of aging time at 180 °C.

5.2. Precipitation Evolution

Figure 3 shows bright-field TEM images after annealing at 180 °C for different annealing times between 0.5 h and 8 h. The length of the precipitates rarely exceeds 10 nm at an annealing time of 0.5 h, whereas 27 nm is measured in the main growth directions at peak ageing.

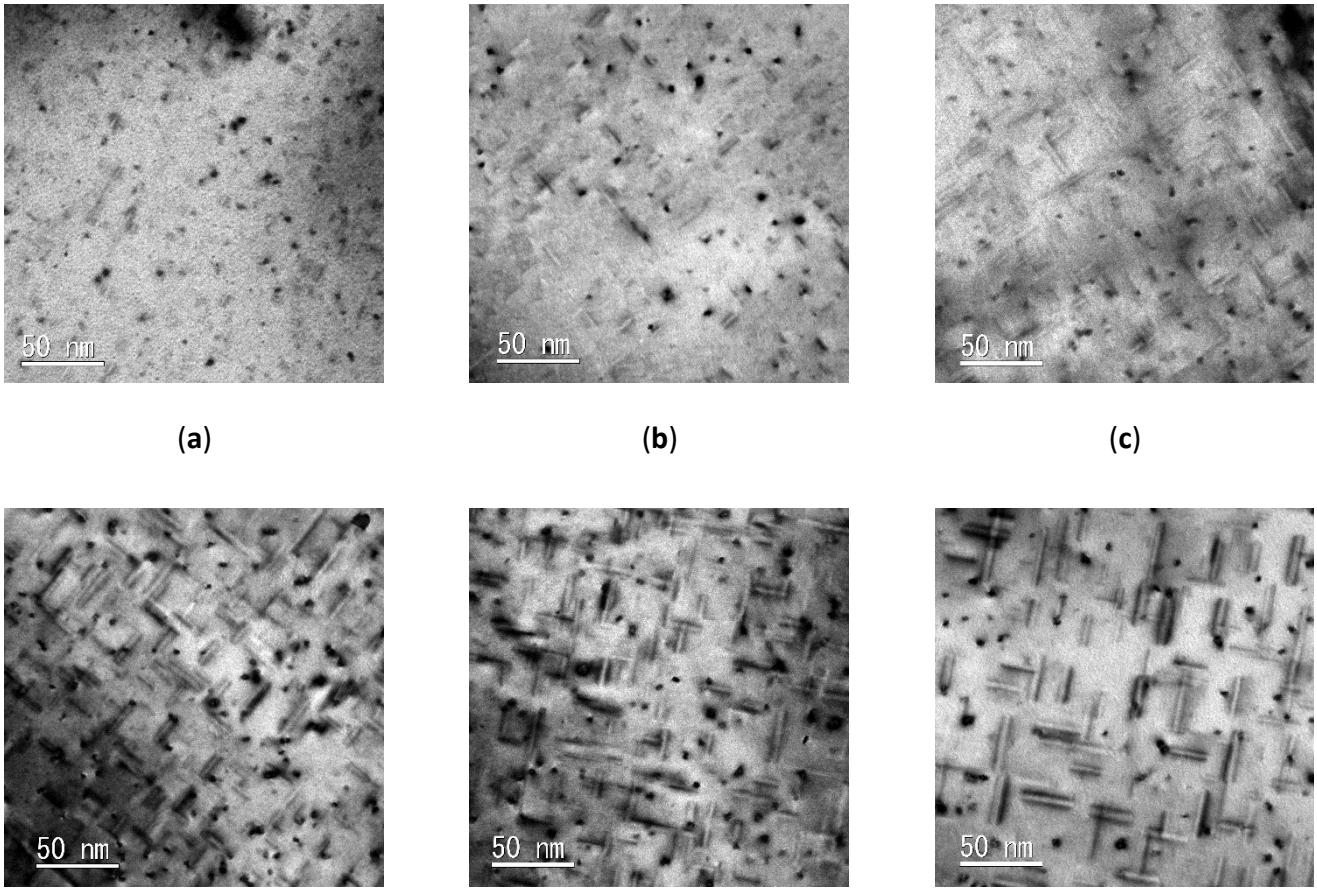

(**a**) (**b**) (**c**)

d) (**e**) (**f**)

Figure 3. TEM images after annealing at 180 °C for (**a**) 0.5 h; (**b**) 1 h; (**c**) 2 h; (**d**) 3 h; (**e**) 4 h and (**f**) 8 h.

Figure 4a shows the temperature profile of the heat treatment of the specimens, where the starting point for the annealing step is illustrated by the doted, vertical lines in Figure 4a–d. The symbols indicate the experimental results for the number density, the length of the precipitates and the phase fraction. The number density *N* is calculated from [56]

$$N = \frac{3 \cdot N_v}{(l + 0.8 \cdot t) \cdot A_{\mathrm{FOV}}} \tag{31}$$

N_v is the number of precipitates of the field of view (FOV) of the TEM image, *l* is the mean length of the precipitates, *t* is the thickness of the specimen, which is measured by EELS, and A_{FOV} is the area of the field of view. Since the evolution of the mean radius *r* of a spherical particle is calculated within the sMSE framework, a conversion to the needle-shaped β'' is necessary. This is done by Equation (32), with the shape parameter *h* [57]. The length *l* of the precipitates increases in good agreement with the measured values as shown in Figure 4c.

$$l = \sqrt[3]{\frac{16}{3} r^3 h^2} \tag{32}$$

It should be emphasised that all precipitates are assumed to be β'' in this simplified framework, because β'' is known to be the main strengthening phase during a T6 heat treatment. The measured number density is almost constant at low annealing times and increases slightly after two hours. The simulations show that the number density of β''rapidly increases when the material is heated up to 180 °C and remains constant during the holding time.

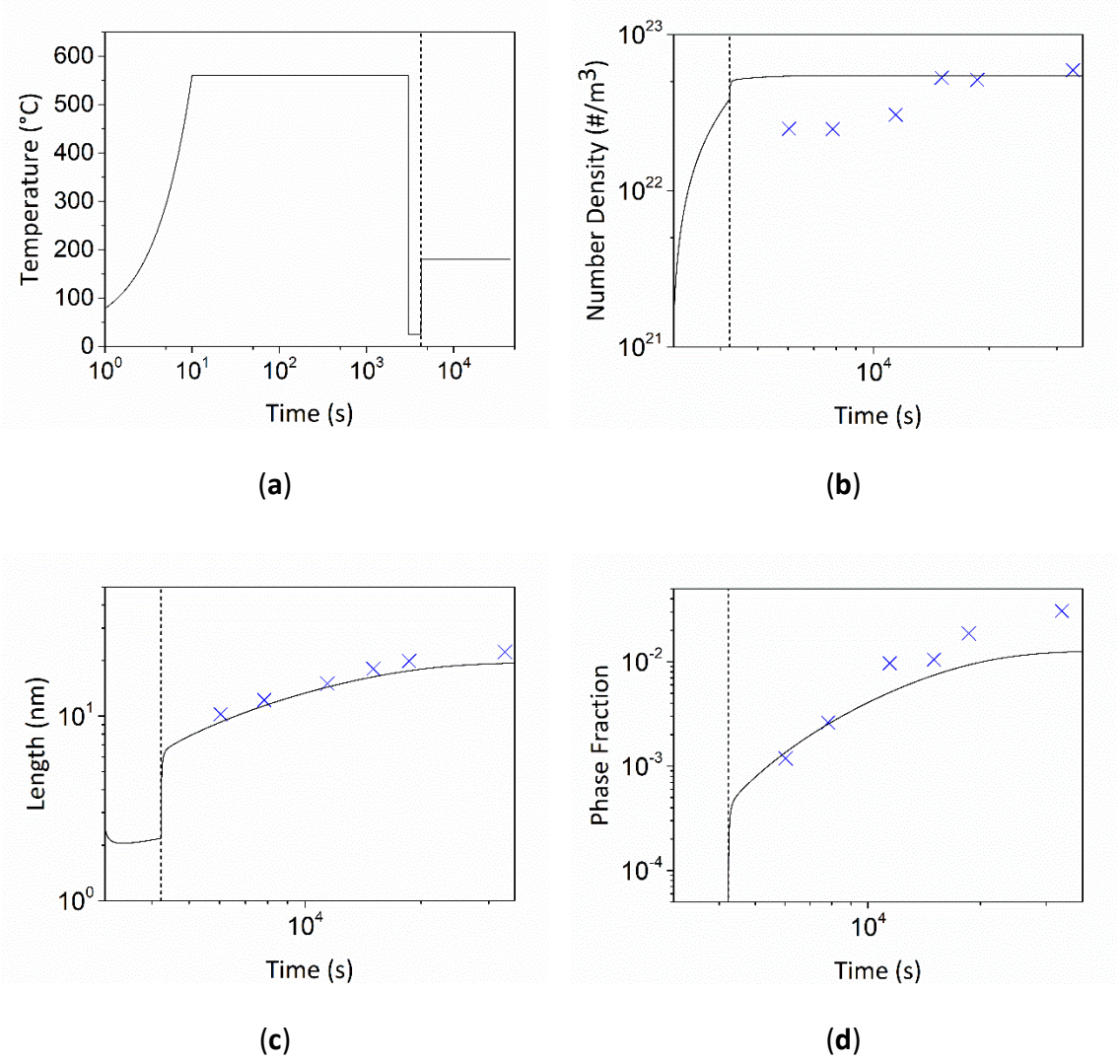

Figure 4. (**a**) The applied heat treatment; (**b**) number density; (**c**) length and (**d**) phase fraction. Solid lines represent simulation results, while symbols indicate experimental results.

5.3. Deformation Tests

Figure 5 shows the flow curves of the compression tests at temperatures between 25 °C and 500 °C and applied true strain rates of 0.1 s^{-1} (a) and 1 s^{-1} (b). The lines represent sMSE simulations, where all calibration parameters are listed in Tables 3 and 4. The stress simulation comprises all strengthening contributions, which have been discussed in Sections 2.1 and 2.2. The simulations show that, the lower the deformation temperature is, the higher is the work hardening contribution. The stronger hardening behavior at 200 °C and 300 °C at the lower deformation rate is due to strain-induced precipitation hardening. This effect is accounted for by an (artificially) adjusted specific interfacial energy of $\gamma = 0.085\ J/m^2$. To demonstrate the influence of precipitation strengthening on the work hardening behavior, simulations without precipitation strengthening, which are marked with *, are included.

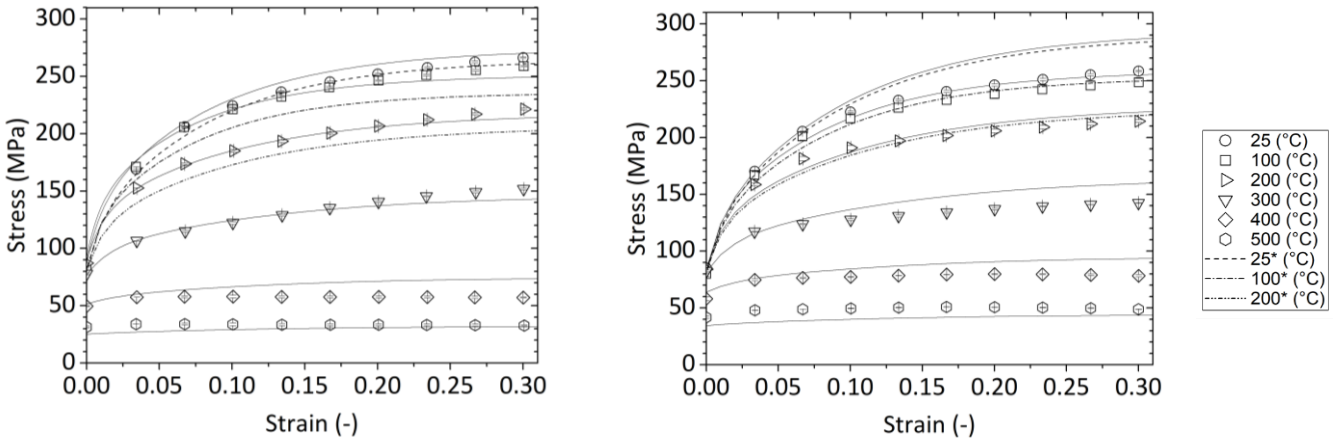

(**a**) (**b**)

Figure 5. Flow curves at different temperatures at applied true strain rates of (**a**) 0.1 s^{-1} and (**b**) 1 s^{-1}. Solid lines represent simulation results, while symbols indicate experimental results. Simulations without precipitation strengthening are marked with *.

To calculate internal stresses using the FEM mesh, an accurate simulation of the yield strength is required. Figure 6a shows the values for $R_{\mathrm{p0.2}}$ as a function of temperature for both strain rates, 0.1 s^{-1} and 1 s^{-1}. The stress values are higher for higher strain rates, except for a temperature of 100 °C and 200 °C. Although the quenching time and the holding time on the deformation temperature are very short, an explanation is given by the cross-core diffusion process on the one hand, and precipitation strengthening on the other hand. The calibration

for the precipitation nucleation process and precipitation growth is discussed in Section 2.3. In Figure 6b, the experimental results of the yield stress are compared to the results of the simulation for both strain rates and six different temperatures. Although simplified models are used in the sMSE framework, experiment and simulation are in good agreement for different temperatures and strain rates with a single set of input parameters.

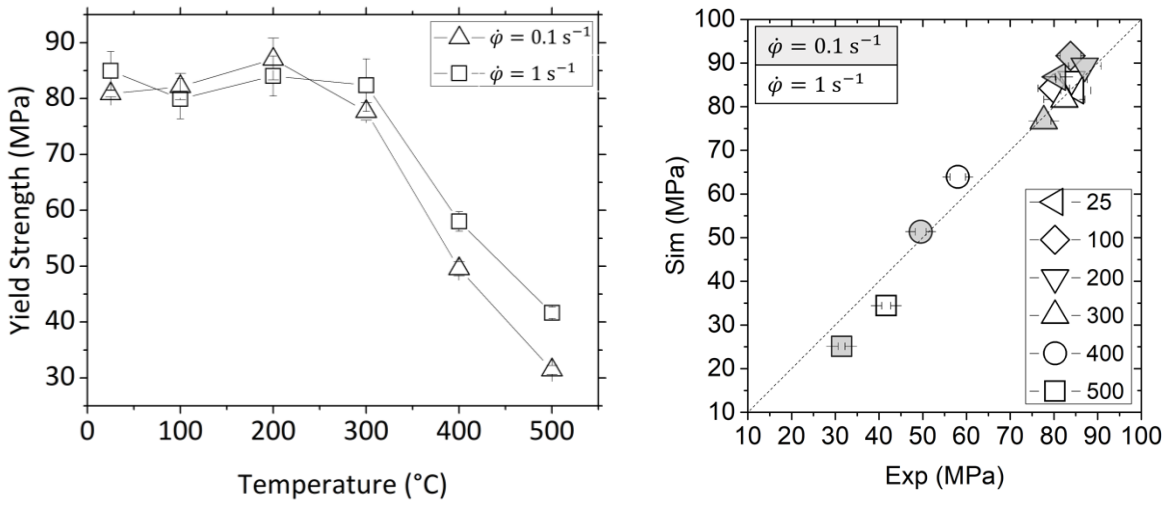

(**a**) (**b**)

Figure 6. (**a**) Yield stresses as a function of temperature for strain rates of 0.1 s^{-1} and 1 s^{-1}. (**b**) Comparison of simulated and experimentally obtained flow stresses.

6. Conclusions

A state parameter-based framework for plastic deformation modelling is introduced, which is suitable for implementation in a user-subroutine in commercial FE-software packages. Well established nucleation and growth models for precipitation kinetics, as well as models for strengthening mechanisms, such as solid solution strengthening, precipitation strengthening and work hardening, are brought into a condensed form to reduce the calculation time for the stress simulation of possible complex structures. In this framework, two alloying components are considered, as well as two precipitate types, which are defined by constant stoichiometry, are included. Although severe simplifications are adopted, flow curves at various temperatures and strain rates are successfully reproduced and the trend of nucleation and growth of precipitates are reflected.

Author Contributions: Conceptualisation, B.V. and E.K.; methodology, B.V.; software, B.V. and E.K.; investigation, B.V. and T.W.; writing—original draft preparation, B.V.; writing—review

and editing, E.K.; visualisation, B.V.; supervision, E.K.; All authors have read and agreed to the published version of the manuscript.

Funding: This research received no external funding.

Institutional Review Board Statement: Not applicable

Informed Consent Statement: Not applicable

Acknowledgments: The TEM analysis was carried out, using facilities at the University Service Centre for Transmission Electron Microscopy, TU Wien, Austria. The authors acknowledge Open Access Funding by TU Wien. Furthermore, the authors thank Neuman Aluminium Industries for providing the materials.

Conflicts of Interest: The authors declare no conflict of interest.

References

1. Ludwik, P. Über Den Einfluss Der Deformationsgeschwindigkeit Bei Bleibenden Deformationen Mit Besonderer Berücksichtigung Der Nachwirkungserscheinungen. *Phys. Zeitschrift* **1909**, *12*, 411–417.
2. Voce, E. A Practical Strain Hardening Function. *Metallurgia* **1955**, 51, 219–226.
3. Johnson, G.R.; Cook, W.H. A Constitutive Model and Data for Metals Subjected to Large Strains, High Strain Rates and High Temperatures. In Proceedings of the 7th International Symposium on Ballistics, The Hague, The Netherlands, 19–21 April 1983; pp. 541-547.
4. Zerilli, F.J.; Armstrong, R.W. Dislocation-Mechanics-Based Constitutive Relations for Material Dynamics Calculations. *J. Appl. Phys.* **1987**, *61*, 1816–1825.
5. Huang, S.; Khan, A.S. Modelling the Mechanical Behavior of 1100-0 Aluminum at Different Strain Rates by the Bodner-Partom Model.Pdf. *Int. J. Plast.* **1992**, *8*, 501–517.
6. Jansen van Rensburg, G.J.; Kok, S.; Wilke, D.N. Modelling Multiple Cycles of Static and Dynamic Recrystallisation Using a Fully Implicit Isotropic Material Model Based on Dislocation Density. *Comput. Mech.* **2018**, *62*, 1343–1367.
7. Wang, Y.; Peng, J.; Zhong, L.; Pan, F. Modeling and Application of Constitutive Model Considering the Compensation of Strain during Hot Deformation. *J. Alloys Compd.* **2016**, *681*, 455–470.
8. Kreyca, J.; Kozeschnik, E. State Parameter-Based Constitutive Modelling of Stress Strain Curves in Al-Mg Solid Solutions. *Int. J. Plast.* **2018**, *103*, 67–80.
9. Sherstnev, P.; Lang, P.; Kozeschnik, E. Treatment of Simultaneous Deformation and Solid-State Precipitation in Thermo-Kinetic Calculations. In Proceedings of the 6th European Congress on

Computational Methods in Applied Sciences and Engineering (ECCOMAS 2012), Vienna, Austria, 10–14 September 2012; pp. 5331–5338.

10. Brinckmann, S.; Sivanesapillai, R.; Hartmaier, A. On the Formation of Vacancies by Edge Dislocation Dipole Annihilation in Fatigued Copper. *Int. J. Fatigue* **2011**, *33*, 1369–1375.
11. Taylor, G.I. The Mechanism of Plastic Deformation of Crystals Part I-Theoretical. *Proc. R. Soc. A Math. Phys. Eng. Sci.* **1934**, *145*, 362–387.
12. Sauzay, M.; Kubin, L.P. Scaling Laws for Dislocation Microstructures in Monotonic and Cyclic Deformation of Fcc Metals. *Prog. Mater. Sci.* **2011**, *56*, 725–784.
13. Viernstein, B.; Schumacher, P.; Milkereit, B.; Kozeschnik, E. State Parameter-Based Simulation of Temperature- and Strain Rate Dependent Flow Curves of Al-Alloys. In *Minerals, Metals and Materials Series*; Springer International Publishing AG, Cham, 2020; pp 267–271.
14. Kocks, U.F. Laws for Work-Hardening and Low-Temperature Creep. *J. Eng. Mater. Technol.* **1976**, *98*, 76–85.
15. Kubin, L.P.; Estrin, Y. Evolution of Dislocation Densities and the Critical Conditions for the Portevin-Le Chatelier Effect. *Acta Met. Mater.* **1990**, *38*, 697–708.
16. Estrin, Y. Dislocation Theory Based Constitutive Modelling: Foundations and Applications. *J. Mater. Process. Technol.* **1998**, *80*, 33–39.
17. Nes, E. Modelling of Work Hardening and Stress Saturation in FCC Metals. *Prog. Mater. Sci.* **1997**, *41*, 129–193.
18. Barlat, F.; Glazov, M.V.; Brem, J.C.; Lege, D.J. A Simple Model for Dislocation Behavior, Strain and Strain Rate Hardening Evolution in Deforming Aluminum Alloys. *Int. J. Plast.* **2002**, *18*, 919–939.
19. Tóth, L.S.; Molinari, A.; Estrin, Y. Strain Hardening at Large Strains as Predicted by Dislocation Based Polycrystal Plasticity Model. *J. Eng. Mater. Technol. Trans. ASME* **2002**, *124*, 71–77.
20. Austin, R.A.; Mcdowell, D.L. A Dislocation-Based Constitutive Model for Viscoplastic Deformation of Fcc Metals at Very High Strain Rates. *Int. J. Plast.* **2011**, *27*, 1–24.
21. Fan, X.G.; Yang, H. Internal-State-Variable Based Self-Consistent Constitutive Modeling for Hot Working of Two-Phase Titanium Alloys Coupling Microstructure Evolution. *Int. J. Plast.* **2011**, *27*, 1833–1852.
22. Gao, C.Y.; Zhang, L.C. Constitutive Modelling of Plasticity of Fcc Metals under Extremely High Strain Rates. *Int. J. Plast.* **2012**, *32–33*, 121–133.
23. Galindo-Nava, E.I.; Sietsma, J.; Rivera-Díaz-Del-Castillo, P.E.J. Dislocation Annihilation in Plastic Deformation: II. Kocks-Mecking Analysis. *Acta Mater.* **2012**, *60*, 2615–2624.
24. Frost, H.J.; Ashby, M.F. *Deformation-Mechanism Maps. The Plasticity and Creep of Metals and Ceramics*, 1st ed.; Pergamon Press: Oxford, UK, 1982.

25. Leyson, G.P.M.; Curtin, W.A.; Hector, L.G.; Woodward, C.F. Quantitative Prediction of Solute Strengthening in Aluminium Alloys. *Nat. Mater.* **2010**, *9*, 750–755.
26. Leyson, G.P.M.; Hector, L.G.; Curtin, W.A. Solute Strengthening from First Principles and Application to Aluminum Alloys. *Acta Mater.* **2012**, *60*, 3873–3884.
27. Leyson, G.P.M.; Curtin, W.A. Friedel vs. Labusch: The Strong/Weak Pinning Transition in Solute Strengthened Metals. *Philos. Mag.* **2013**, *93*, 2428–2444.
28. Leyson, G.P.M.; Curtin, W.A. Thermally-Activated Flow in Nominally Binary Al-Mg Alloys. *Scr. Mater.* **2016**, *111*, 85–88.
29. Labusch, R. A Statistical Theory of Solid Solution Hardening. *Phys. Stat. Sol.* **1970**, *41*, 659–669.
30. Haasen, P. Mechanical Properties of Solid Solutions. In *Physical Metallurgy*; Elsevier Science B.V., Amsterdam, 1996; pp. 2010–2073.
31. Curtin, W.A.; Olmsted, D.L.; Hector, L.G. A Predictive Mechanism for Dynamic Strain Ageing in Aluminium-Magnesium Alloys. *Nat. Mater.* **2006**, *5*, 875–880.
32. Orowan, E. *Symposium on Internal Stresses in Metals and Alloys*, *Session III, Discussion*; Institute of Metals: London, UK, 1948.
33. Ahmadi, M.R.; Povoden-Karadeniz, E.; Öksüz, K.I.; Falahati, A.; Kozeschnik, E. A Model for Precipitation Strengthening in Multi-Particle Systems. *Comput. Mater. Sci.* **2014**, *91*, 173–186.
34. Ashby, M.F. The Theory of the Critical Shear Stress and Work Hardening of Dispersion-Hardened Crystals. *Metall. Soc. Conf.* **1966**, *47*, 143–205.
35. Brown, L.M.; Ham, R.K. *Strengthening Mechanisms in Crystals*; Kelly, A., Nicholson, R.B., Elsevier; New York, NY, USA, 1971; pp. 9–70.
36. Ardell, A.J. Precipitation Hardening. *Metall. Trans. A* **1985**, *16A*, 2131–2165.
37. Sonderegger, B.; Holzer, I.; Kozeschnik, E.; Sommitsch, C. Particle Distance Distributions and Their Effect on Precipitation Strengthening. *Comput. Methods Mater. Sci.* **2011**, *11*, 148–143.
38. Svoboda, J.; Fischer, F.D.; Fratzl, P.; Kozeschnik, E. Modelling of Kinetics in Multi-Component Multi-Phase Systems with Spherical Precipitates I: Theory. *Mater. Sci. Eng. A* **2004**, *385*, 166–174.
39. Kozeschnik, E.; Svoboda, J.; Fratzl, P.; Fischer, F.D. Modelling of Kinetics in Multi-Component Multi-Phase Systems with Spherical Precipitates II: Numerical Solution and Application. *Mater. Sci. Eng. A* **2004**, *385*, 157–165.
40. Kozeschnik, E.; Svoboda, J.; Fischer, F.D. Modified Evolution Equations for the Precipitation Kinetics of Complex Phases in Multi-Component Systems. *Calphad* **2004**, *28*, 379–382.
41. Russell, K.C. Nucleation in Solids: The Induction and Steady State Effects. *Adv. Colloid Interface Sci.* **1980**, *13*, 205–318.
42. Kozeschnik, E. *Modeling Solid-State Precipitation*; Momentum Press, LLC: New York, NY, USA, 2013.

43. Zeldovich, J.B. On the Theory of New Phase Formation Cavitation. *Acta Physicochim. URSS* **1943**, *18*, 1–22.
44. Fischer, F.D.; Svoboda, J.; Appel, F.; Kozeschnik, E. Modeling of Excess Vacancy Annihilation at Different Types of Sinks. *Acta Mater.* **2011**, *59*, 3463–3472.
45. Lifshitz, L.M.; Slyozov, V.V. The Kinetics of Precipitation from Supersaturated Solid Solutions*. *J.Phys.Chem. Solids* **1959**, *19*, 35–50.
46. Wagner, C. Theorie Der Alterung von Niederschlägen Durch Umlösen (Ostwald-Reifung). *Z. Für Elektrochem.* **1961**, *65*, 581–591.
47. Ågren, J.; Clavaguera-Mora, M.T.; Golcheski, J.; Inden, G.; Kumar, H.; Sigli, C. Application of Computational Thermodynamics to Phase Transformation Nucleation and Coarsening. *Calphad* **2000**, *24*, 42–54.
48. Malis, T.; Cheng, S.C.; Egerton, R.F. EELS Log-ratio Technique for Specimen-thickness Measurement in the TEM. *J. Electron Microsc. Tech.* **1988**, *8*, 193–200.
49. Andersen, S.J.; Zandbergen, H.W.; Jansen, J.; Træholt, C.; Tundal, U.; Reiso, O. The Crystal Structure of the β" Phase in Al-Mg-Si Alloys. *Acta Mater.* **1998**, *46*, 3283–3298.
50. Kocks, U.F. The Relation between Polycrystal Deformation and Single-Crystal Deformation. *Metall. Mater. Trans.* **1970**, *1*, 1121–1143.
51. Madec, R.; Devincre, B.; Kubin, L.P. From Dislocation Junctions to Forest Hardening. *Phys. Rev. Lett.* **2002**, *89*, 1–4.
52. Schoeck, G.; Frydman, R. The Contribution of the Dislocation Forest to the Flow Stress. *Phys. Status Solidi* **1972**, *53*, 661–673.
53. Hirth, J.P.; Lothe, J. *Theory of Dislocations*; Krieger Publishing Company, Malabar, Florida, 1991.
54. Uesugi, T.; Higashi, K. First-Principles Studies on Lattice Constants and Local Lattice Distortions in Solid Solution Aluminum Alloys. *Comput. Mater. Sci.* **2013**, *67*, 1–10.
55. Fujikawa, S.; Hirano, K. Diffusion of 28Mg in Aluminum. *Mater. Sci. Eng.* **1977**, *27*, 25–33.
56. Yang, M.; Chen, H.; Orekhov, A.; Lu, Q.; Lan, X.; Li, K.; Zhang, S.; Song, M.; Kong, Y.; Schryvers, D.; Du, Y. Quantified Contribution of β" and β' Precipitates to the Strengthening of an Aged Al–Mg–Si Alloy. *Mater. Sci. Eng. A* **2020**, *774*, 138776.
57. Kozeschnik, E.; Svoboda, J.; Fischer, F.D. Shape Factors in Modeling of Precipitation. *Mater. Sci. Eng. A* **2006**, *441*, 68–72.

Journal Paper 3

Article

Strain hardening in dilute binary Al-Cu, Al-Zn, and Al-Mn alloys: Experiment and modeling

Bernhard Viernstein, Laszlo Solyom, Ernst Kozeschnik *

1 Institute of Materials Science and Technology, TU Wien, Getreidemarkt 9, 1060 Vienna, Austria;

* Correspondence: ernst.kozeschnik@tuwien.ac.at

Abstract:

During thermo-mechanical processing, dissolved alloying elements have a huge impact on the microstructure evolution by influencing the overall dislocation storage rate. Especially, for non-heat treatable Al alloys, the effects of strain hardening and solid solution strengthening are of significant practical interest. In the present work, a detailed study of the room-temperature work-hardening behavior of binary Al-Cu, Al-Zn, and Al-Mn alloys with varying solute concentrations is carried out. Stress-strain curves at different strain rates are recorded and computationally analyzed by an advanced 3-Internal-Variables-Model (3IVM) approach for the dislocation density evolution. The initial strengthening rate is examined as a function of the solute concentration.

Keywords: Strengthening mechanisms, Dislocations, Rate-dependent material, Mechanical testing

1. Introduction

Accurate and reliable constitutive models of dislocation–solute interactions are mandatory for the design of new alloys. The influence of alloying elements on the properties of the materials is manifold: Solid solution strengthening increases the yield stress [1], the energy of thermal activation is modified [2–4], and the evolution of mobile dislocations is changed [5]. Solid

solution strengthening is determined by the interaction of dislocation and solute atoms, leading to the following mechanisms: size effect [6], modulus effect [7], Suzuki effect [8], and electrostatic interaction [9]. The size effect is often the most important contribution and is based on the misfit strain, caused by the size difference of the substitutional solute atom, compared to the matrix element. These misfit strains can be obtained by first principle studies [3]. Mott and Nabarro suggested a linear relationship between the stress and the atomic concentration, c [10], Friedel correlated the stress with $c^{1/2}$ [11], and Labusch suggested a dependency of $c^{2/3}$ [1]. As demonstrated by Leyson and Curtin [12], the Labusch model controls the strengthening for concentrations greater than 10^{-4} (at.%) and temperatures above 78 K for Al alloys. Therefore, the Labusch model is used for the simulation of solid solution strengthening in the present work. Apart from solutes, precipitates and grain boundaries are potential obstacles for moving dislocations. The characteristic energy barrier for pinned segments is assumed to be dependent on $c^{1/3}$ [2–4].

Apart from influencing the yield stress and the activation energy for dislocation movement, solute atoms modify the strain-hardening behavior (see, e.g. refs. [13,14]). The formation mechanisms of mobile- and immobile dislocation structures are discussed in literature (e.g., in [15]), but detailed studies of their concentration dependencies are often missing. Therefore, binary Al-X (X = Mn, Zn, Cu) alloys are analyzed in the present paper and the generation of dislocations and the dynamic recovery are expressed as a function of the concentration of the alloying elements. An increasing hardening rate can be interpreted as a decrease in the stacking fault energy and the subsequent drop in the cross-slip probability of dislocations due to solute additions [16]. However, an opposing effect is also reported in refs. [17–19]. A decreased stacking fault energy reduces the generation rate of new dislocations since double cross slip can result in new Frank-Read sources. Furthermore, local solute concentration in the dislocation core influences strain hardening by modifying the critical annihilation distance for dynamic recovery [5].

The model for the simulation of the mechanical properties of the alloys consists of a thermal stress contribution, including solid solution strengthening, as well as an athermal work hardening. An advanced 3-Internal-Variables-Model (3IVM) [20,21] is used and adapted to describe the cellular dislocation microstructure, which is characterized by cell interior dislocations and cell wall dislocations. The strain rate- and concentration-dependency of mobile and immobile dislocation production, as well as dynamic and static recovery are

analyzed for all binary Al alloys of the present study. Through this approach, both, the strengthening contribution of solutes as well as its influence on the microstructure evolution during the deformation process are described. Suitable heat treatments suppress strengthening due to grain refinement and precipitation strengthening.

In the first part of the work, the models for the flow curve simulations are introduced. In the second part, the experimental results are compared to simulations, which are performed with the thermo-kinetic software package MatCalc **(http://matcalc.at)**, version 6.04.0134, which incorporates the suggested models.

2. The model

The present model comprises a thermal stress contribution, σ_{th}, which is based on the mechanical threshold concept, and an athermal stress contribution, σ_{ath}, which accounts for the impact of dislocations. The total stress contribution, which is strongly dependent on the microstructure, is calculated by the superposition of both stress contributions.

2.1 Thermal stress contribution σ_{th}

Plastic deformation of polycrystalline materials can be described by empirical models, such as those developed in refs. [22–26], or by state parameter-based yield strength models, as given in refs. [27–36]. In a physically-based picture of plastic deformation, a mobile dislocation can overcome an obstacle/energy barrier by thermal activation. Kreyca and Kozeschnik [37] distinguish between a low-temperature regime, 'lt', where dislocation glide is dominant, and a high-temperature regime, 'ht', where obstacles can be overcome by climbing processes of dislocations. Since all deformation tests are carried out at room temperature, in the present work, only σ_{lt} is of relevance ($\sigma_{\mathrm{th}} = \sigma_{\mathrm{lt}}$), which can be expressed by the Arrhenius type equation [37]

$$\sigma_{\mathrm{lt}} = \hat{\tau} \cdot \exp\left(\frac{-k_{\mathrm{B}} T}{\Delta F^{\mathrm{lt}}} \cdot \ln\left(\frac{\dot{\varepsilon}_0}{\dot{\varepsilon}}\right)\right). \tag{1}$$

$\hat{\tau}$ is the mechanical threshold, which comprises the basic stress, solid solution strengthening σ_{SS} (see 2.1.1), and strengthening stemming from the cross-core diffusion effect [38]. k_{B} is the Boltzmann constant, *T* is the temperature, $\dot{\varepsilon}_0$ is a constant and $\dot{\varepsilon}$ is the strain rate. The

activation energy ΔF^{lt} depends on the effective concentration, c_{eff}, of the alloying elements, and is given by [37]

$$\Delta F^{\mathrm{lt}} = (k_1 + k_2 \cdot c_{\mathrm{eff}}^{n}) \cdot G b^3. \tag{2}$$

k_1 and k_2 are constants, *n* is a fitting exponent, *b* is the Burgers vector and *G* is the shear modulus. The cross-core diffusion effect [38] is accounted for in the effective concentration c_{eff}.

2.1.1 Solid solution hardening

To incorporate the solid solution strengthening contribution in the present framework, the following equation, which is based on the Labusch approach [1], is utilized

$$\sigma_{\mathrm{SS}} = \left(\sum_i \left(k_i c_i^{\frac{2}{3}} \right)^{n_{\mathrm{SS}}} \right)^{\frac{1}{n_{\mathrm{SS}}}}. \tag{3}$$

The subscript 'SS' refers to solid solution. The contributions of the alloying elements, with the concentrations c_i, are calculated separately and summed up, using the exponent coefficient n_{SS}. k_i is adopted from [1] and reads as

$$k_i = \left(\frac{{f_{\max}}^4 \cdot w}{8 \cdot E_{\mathrm{L}} \cdot b^7} \right)^{\frac{1}{3}}. \tag{4}$$

$f_{\max}$ is the maximum interaction force between the solute and the dislocation, given by [1]

$$f_{\max} = \frac{\sqrt{3}}{2} \cdot \left(\frac{1+\nu}{1-\nu} \right) G b^2 |\varepsilon_{\mathrm{m}}|. \tag{5}$$

$w = 5b$ is the interaction distance and the dislocation line tension $E_{\mathrm{L}} = \frac{1}{2} \cdot G \cdot b^2$ [39]. ν is the Poisson's ratio and ε_{m} is the misfit strain between solute and matrix atoms.

2.2 Athermal stress contribution σ_{ath}

For the calculation of the athermal stress contribution, an advanced ABC model is used, which is derived from the original 3-Internal-Variables-Model (3IVM) [20]. The designation 'ABC' originally refers to the dislocation generation parameter A, the dynamic annihilation parameter relevant at low and intermediate temperatures B, and the static recovery

parameter C at elevated temperatures, as used in ref. [40]. The advanced ABC model describes the generation and reduction of mobile and immobile dislocations, with the respective dislocation density in the cell interior, ρ_{int}, and the cell wall dislocation density, ρ_{w}. It is described in detail in the subsequent sections. The Taylor equation is used to describe the athermal stress contribution in the form

$$\sigma_{\mathrm{ath}} = \alpha_1(1-f_{\mathrm{w}})bMG\sqrt{\rho_{\mathrm{int}}} + \alpha_2 f_{\mathrm{w}} bMG\sqrt{\rho_{\mathrm{w}}}, \tag{6}$$

where the strengthening coefficients $\alpha_1 = \alpha_2 = 0.34$. The strengthening coefficient α is thoroughly discussed for instance in [41–45]. A constant value for α is assumed for the different dislocation structures in the present work for the merit of clear interpretation of the simulation results. This is certainly a simplification, but it provides a consistent correlation between the simulated dislocation density and the measured flow stress with respect to our experimental observations. The volume fraction of cell walls is also assumed to be constant with *f*w=0.1, for the same reason as for the value of α. *M* is the Taylor factor.

2.2.1 Internal dislocation density

The internal dislocation density, ρ_{int}, is defined as the sum of the excess mobile dislocation density in the cell interior, $\rho_{\mathrm{ex,m}}$ or simply ρ_{m}, the immobile dislocation density ρ_{im}, and the equilibrium internal dislocation density $\rho_{\mathrm{equ,i}}$, which is assumed to be 10^{11} m^{-2} in this work. Mobile dislocations are produced at dislocation sources and move through the cell interiors and cell walls until they eventually become immobilized or annihilated. The mobile generation term can be written as [31]

$$\dot{\rho}_{\mathrm{m}}^{+} = \frac{M\dot{\epsilon}}{bL_{\mathrm{eff}}}. \tag{7}$$

L_{eff} is the effective mean free travel distance of a mobile dislocation [20], and it is expressed as

$$\frac{1}{L_{\mathrm{eff}}} = \frac{\sqrt{\rho_{\mathrm{int}}}}{A_{\mathrm{m}}} + \frac{\sqrt{\rho_{\mathrm{w}}}}{\beta_{\mathrm{w}}} + \frac{\beta_{\mathrm{G}}}{D_{\mathrm{G}}} + \beta_{\mathrm{SS}}\cdot\sqrt{\rho_{\mathrm{m}}}. \tag{8}$$

The first two contributions on the right-hand side account for the interaction of mobile dislocations with internal dislocations as well as wall dislocations. A_{m} and β_{w} are constants,

related to the impact of dislocations on the free travel distance of mobile dislocations during deformation. β_{G} is a constant related to the effect of grain size with diameter D_{G}. Although this simplified approach neglects the interaction of the individual contributions, it is widely used in literature and it has the potential to be extended by twinning- and precipitation effects [46,47]. The applied model is also suitable for simulating the dislocation structures within a wide temperature range (e.g. -196 °C – 500 °C), as successfully shown in [48]. The equations (9), (10) and (11) describe the reduction rate of mobile dislocations by annihilation due to dislocation glide, and the formation of dipoles and locks. The different critical distances related to each mechanism are accounted for by the parameters B_{m}, A_{w} and A_{im}, in the attempt to use the same value of d_{crit} for each mechanism, however, with individual pre-factors. The reduction rate for mobile dislocations due to annihilation is expressed as [37]

$$\dot{\rho}_{\mathrm{m,ann}}^{-} = 2 \cdot B_{\mathrm{m}} \cdot \frac{d_{\mathrm{crit}} \dot{\epsilon} M}{b} \rho_{\mathrm{m}}. \tag{9}$$

It should be emphasized that B_{m} can be concentration-dependent (see section 5.1 later). For a detailed explanation of this relation see, e.g. Deschamps et al. [5].

Dislocation dipoles can form if the stress fields of two antiparallel mobile dislocations interact but they are too far away from each other to annihilate. Dislocation dipoles are often swept into the cell walls and do not contribute to plastic shear deformation at all. The reduction rate of mobile dislocations due to the formation of dipoles is given as

$$\dot{\rho}_{\mathrm{m,dip}}^{-} = 2 \cdot A_{\mathrm{w}} \cdot \frac{d_{\mathrm{crit}} \cdot \dot{\epsilon} M}{b} \rho_{\mathrm{m}}. \tag{10}$$

Dislocation locks can be created, when two dislocations come closer to each other than a critical distance but move on different slip planes such that the resulting Burgers vector of the combined dislocation is located outside an active glide plane. The corresponding reduction rate is expressed as

$$\dot{\rho}_{\mathrm{m,lock}}^{-} = 4 \cdot A_{\mathrm{im}} \cdot \frac{d_{\mathrm{crit}} \cdot \dot{\epsilon} M}{b} \rho_{\mathrm{m}}. \tag{11}$$

At higher temperatures, annihilation due to climbing processes takes place, leading to [37]

$$\dot{\rho}_{\mathrm{m,climb}}^{-} = 2 \cdot C_{\mathrm{m}} \cdot M \cdot \frac{D_{\mathrm{eff}} G b^3}{k_{\mathrm{B}} T} \left({\rho_{\mathrm{m}}}^2 - \rho_{\mathrm{equ,i}}^2 \right). \tag{12}$$

C_{m} is a constant and D_{eff} is the effective diffusion coefficient that includes the accelerating effect of excess vacancies [49], dislocation pipe diffusion [50], and the retarding effect of trapping of vacancies at solute atoms [51]. Since all experiments are conducted at room temperature in this work, climbing processes are neglected in the following treatment, although the respective terms are included in the rate equations of the MatCalc software. The overall evolution equation of the mobile dislocation density is finally

$$\dot{\rho}_{\mathrm{m}} = \dot{\rho}_{\mathrm{m}}^{+} - \dot{\rho}_{\mathrm{m,ann}}^{-} - \dot{\rho}_{\mathrm{m,dip}}^{-} - \dot{\rho}_{\mathrm{m,lock}}^{-} - \dot{\rho}_{\mathrm{m,climb}}^{-}. \tag{13}$$

The production rate of immobile dislocations ρ_{im} in the cell interior is equal to the formation rate of dislocation locks from mobile dislocations with

$$\dot{\rho}_{\mathrm{im}}^{+} = \dot{\rho}_{\mathrm{m,lock}}^{-}. \tag{14}$$

The immobile dislocations can become annihilated at sufficiently high temperatures by climbing expressed as

$$\dot{\rho}_{\mathrm{im,climb}}^{-} = -2 \cdot C_{\mathrm{im}} \cdot M \cdot \frac{D_{\mathrm{eff}} G b^3}{k_{\mathrm{B}} T} \rho_{\mathrm{im}}^2, \tag{15}$$

where C_{im} is a constant. In the present framework, the immobile dislocation density can also be reduced dynamically at room temperature at a rate of

$$\dot{\rho}_{\mathrm{im,ann}}^{-} = -4 \cdot B_{\mathrm{im}} \cdot \frac{d_{\mathrm{crit}} \cdot \dot{\epsilon} M}{b} \rho_{\mathrm{im}}, \tag{16}$$

where the parameter B_{im} is defined in Table 5. The overall evolution rate for immobile dislocations ρ_{im} is given by the sum of equations (14), (15) and (16).

2.2.2 Wall dislocation density

In addition to the stored mobile and immobile dislocations, the dipoles, which form inside the cells, are swept into the cell walls, as originally proposed by Kratocvil and Libovicky [52]. Therefore, the production rate of excess wall dislocations is assumed to be

$$\dot{\rho}_{\mathrm{w}}^{+} = \frac{1}{f_{\mathrm{w}}} \dot{\rho}_{\mathrm{m,dip}}^{-}. \tag{17}$$

Only diffusion-controlled climbing is assumed, in the present work, to reduce the wall dislocation density, given by

$$\dot{\rho}_{\mathrm{w}}^{-} = 2 \cdot C_{\mathrm{w}} \cdot M \cdot \frac{D_{\mathrm{eff}} G b^{3}}{k_{\mathrm{B}} T} (\rho_{\mathrm{w}}^{2}), \tag{18}$$

where C_{w} is a constant. The overall wall dislocation density evolution is given by the weighted sum of the internal dislocation density evolution rates, $\dot{\rho}_{\mathrm{w}}^{+}$ and $\dot{\rho}_{\mathrm{w}}^{-}$. The total dislocation density is finally

$$\rho_{\mathrm{tot}} = (1 - f_{\mathrm{w}}) \cdot \rho_{\mathrm{int}}(t) + f_{\mathrm{w}} \cdot \rho_{\mathrm{w}}(t). \tag{19}$$

3. Experimental

3.1 Material and heat treatment

All binary Al-X alloys are cast in an inductive melting furnace using high purity Al 99.999 wt%, Cu 99.99 wt%, Zn 99.99 wt% and Mn 99.99 wt%. The ingots with the highest alloying concentrations are used as master alloys for preparing the more dilute alloys. The following Table 1, Table 2 and Table 3 describe the designation of the alloys and the measured concentrations in weight percent by a wet-chemical analysis.

Table 1. Cu alloys designation and measured concentration in wt%.

	Cu 0.1 %	Cu 0.4 %	Cu 0.8 %	Cu 1.6 %
Cu (%)	0.13	0.44	0.86	1.56

Table 2. Zn alloys designation and measured concentration in wt%.

	Zn 0.4 %	Zn 0.8 %	Zn 2 %	Zn 4 %
Zn (%)	0.46	0.94	2.17	4.81

Table 3. Mn alloys designation and measured concentration in wt%.

	Mn 0.1 %	Mn 0.2 %	Mn 0.4 %	Mn 0.8 %
Mn (%)	0.11	0.23	0.43	0.82

The processing of the cylindrical specimens for the deformation tests follows the same procedure for all binary alloys: casting, homogenization, extrusion, additional heat treatment, and mechanical sample preparation. All heat treatments are carried out in a circulating air furnace (Carbolite Type 3508). The ingots are homogenized in the following way: Al-Cu - 480 °C for 6 h; Al-Zn - 530 °C for 5 h; Al-Mn - 630 °C for 5 h. The homogenization temperatures are chosen to ensure a solid solution of the alloying elements within the Al matrix. The ingots are quenched in water to prevent the nucleation of precipitates. These quenching rates are high enough to avoid the formation of precipitates at these low alloying concentrations, as reported in [16,53,54]. To get rid of the casting microstructure, the ingots are extruded to a final diameter of 10 mm before additional heat treatment (Al-Cu - 530 °C for 1 h; Al-Zn - 530 °C for 1 h; Al-Mn - 630 °C for 1 h), ensuring homogeneous and large grain sizes. Since this work focuses on the influence of solutes on both, the yield stress and the work hardening behavior, hardening due to fine grains is thus excluded. Finally, cylindrical specimens with a diameter of 5 mm and a length of 10 mm are fabricated.

3.2 Mechanical testing

The compression tests to obtain the flow curves are performed on a dilatometer DIL 805 A/D. Prior to the deformation step, the specimens are solution heat treated at 530 °C for 5 min and helium-cooled with a cooling rate of 50 K/s to room temperature. Each deformation test is repeated at least twice with applied true strain rates of 0.001 s^{-1}, 0.01 s^{-1}, 0.1 s^{-1} and 1 s^{-1}.

4. Experimental results

To analyze the influence of solutes on the plastic deformation behavior, the yield stress $Rp_{0.2}$ and the initial hardening rate θ_0, which is the slope of the stress-strain curve at the yield point, are utilized. For a schematic illustration of θ_0, see, e.g., Kreyca and Kozeschnik [37]. Attention should be drawn to the fact that the evaluation of θ_0 is very sensitive to the applied data evaluation criteria and to the nature of the data in general. Still, this analysis delivers a trend, which can provide valuable insight into the dislocation evolution behavior.

In this section, the initial hardening rates θ_0 and the yield stresses are plotted as a function of the solute content and the strain rates for the binary Al-Mn, Al-Cu and Al-Zn alloys. In each plot, the results for pure Al are included, to have a baseline for a better illustration of the influence of the alloying elements on the mechanical properties. The results of the flow curves are shown in chapter 5.3, where the MatCalc simulations are also included.

4.1 Binary Al-Mn alloys

Figure 1 (a) shows an increasing initial hardening rate θ_0 with an increasing concentration of Mn. Interestingly, 0.1 wt% and 0.2 wt% Mn have almost no impact on the hardening rate, compared to pure Al. A clear increase in the initial hardening rate can be noticed at high strain rates as shown in Figure 1 (b).

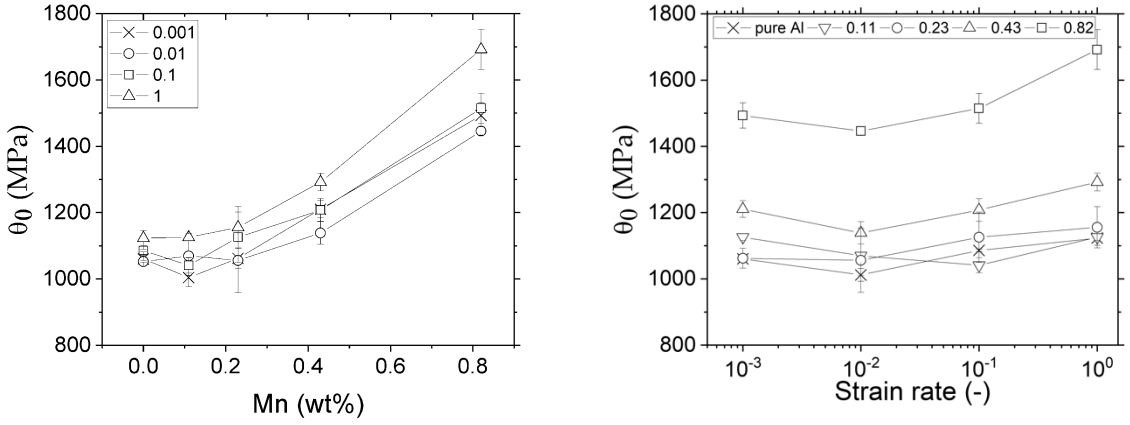

(a) **(b)**

Figure 1. Initial hardening rate θ_0 as a function of (**a**) the concentration of Mn and (**b**) the true strain rate.

The yield stress, $\mathrm{Rp}_{0.2}$, is strongly increased by additions of Mn, and a clear trend of increasing yield stress as a function of the strain rate, especially, at high concentrations, is visible in Figure 2 (a) and (b).

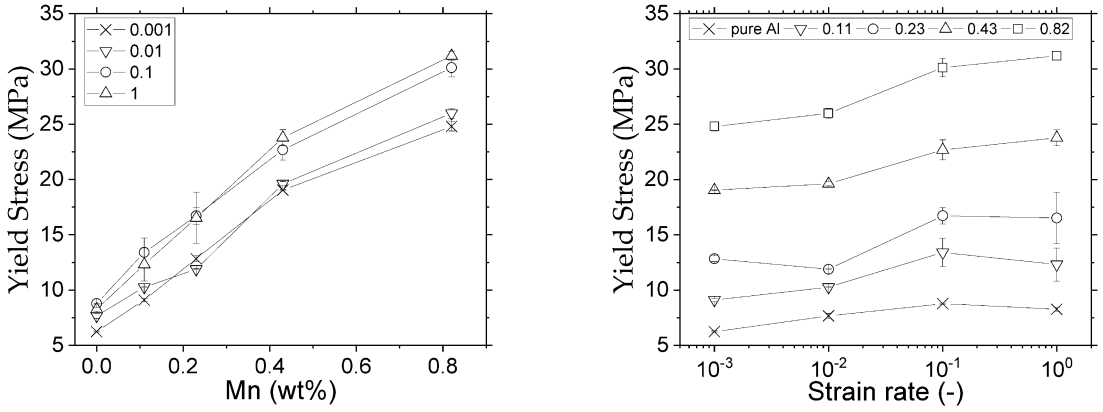

(a) **(b)**

Figure 2. Yield stress as a function of (**a**) the concentration of Mn and (**b**) the true strain rate.

4.2 Binary Al-Cu alloys

The higher the amount of dissolved Cu within the Al matrix, the higher is the initial hardening rate θ_0, as indicated in Figure 3 (a). However, θ_0 slightly decreases with an increasing strain rate, as shown in Figure 3 (b), which is different from the effects of Mn and the dependency in pure Al.

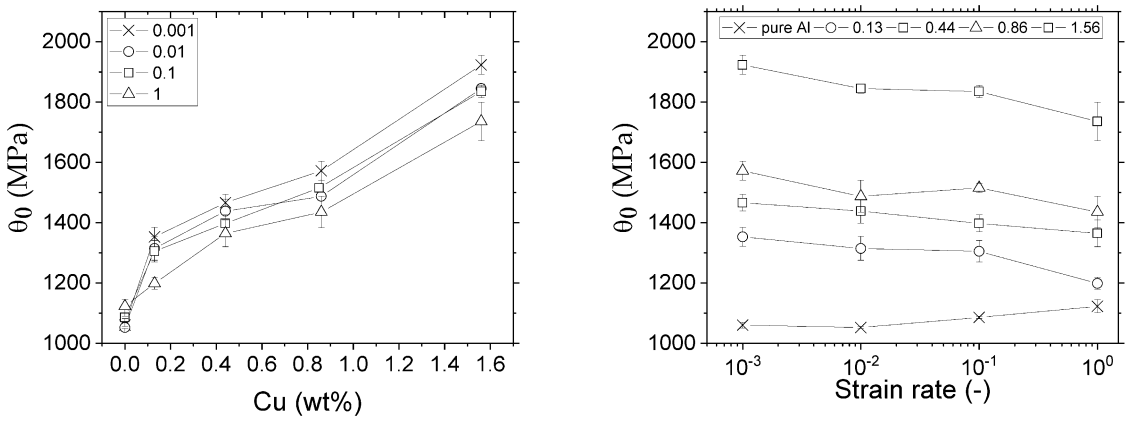

(a) **(b)**

Figure 3. Initial hardening rate θ_0 as a function of (**a**) the concentration of Cu and (**b**) the true strain rate.

The yield stress increases with an increasing amount of Cu, whereas no clear trend is observed as a function of the strain rate, as shown in Figure 4.

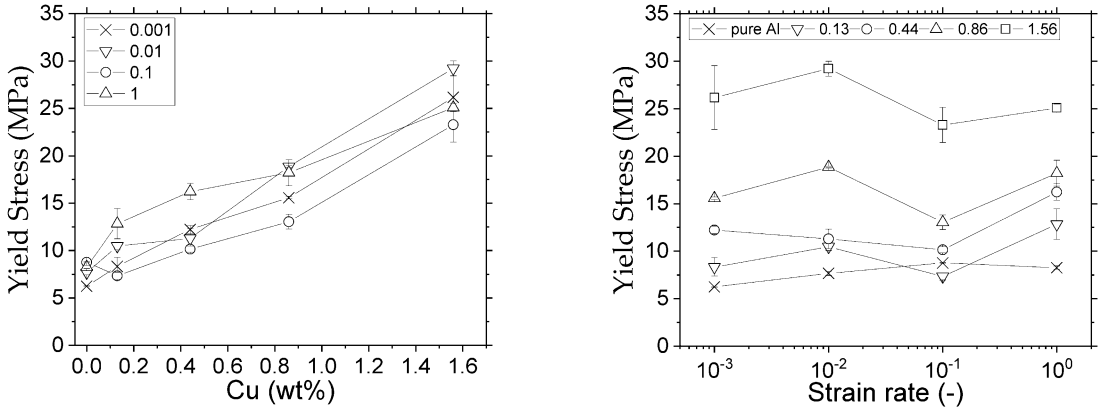

(a) **(b)**

Figure 4. Yield stress as a function of (**a**) the concentration of Cu and (**b**) the true strain rate.

4.3 Binary Al-Zn alloys

A small amount of Zn within the Al matrix strongly increases the initial hardening rate θ_0, compared to pure Al, as shown in Figure 5 (a). The more Zn is included, the smaller the θ_0 value becomes. Furthermore, θ_0 slightly decreases with an increasing strain rate, as shown in Figure 5 (b).

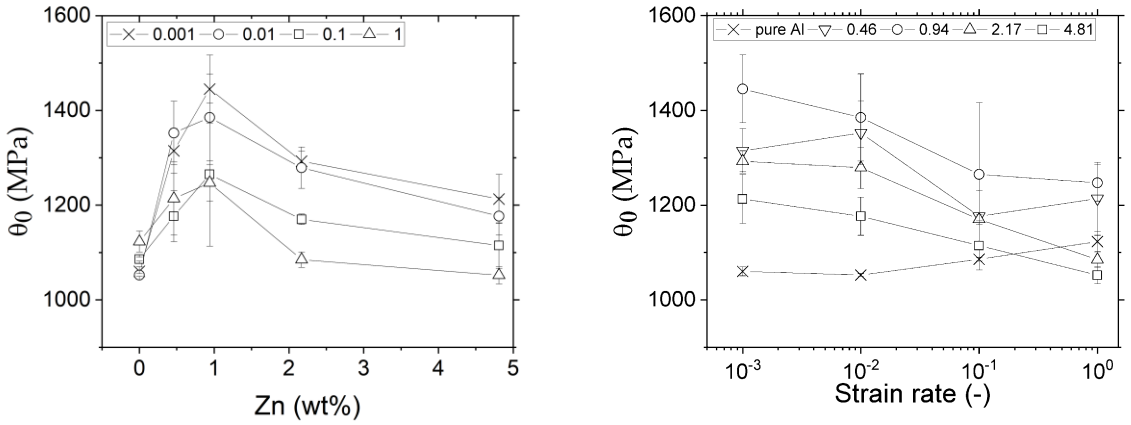

(a) **(b)**

Figure 5. Initial hardening rate θ_0 as a function of (**a**) the concentration of Zn and (**b**) the true strain rate.

Zn has a rather low impact on the solid solution strengthening effect, leading to similar yield stresses, as shown in Figure 6 (a). The higher the strain rate, the higher is the yield stress, as indicated in Figure 6 (b).

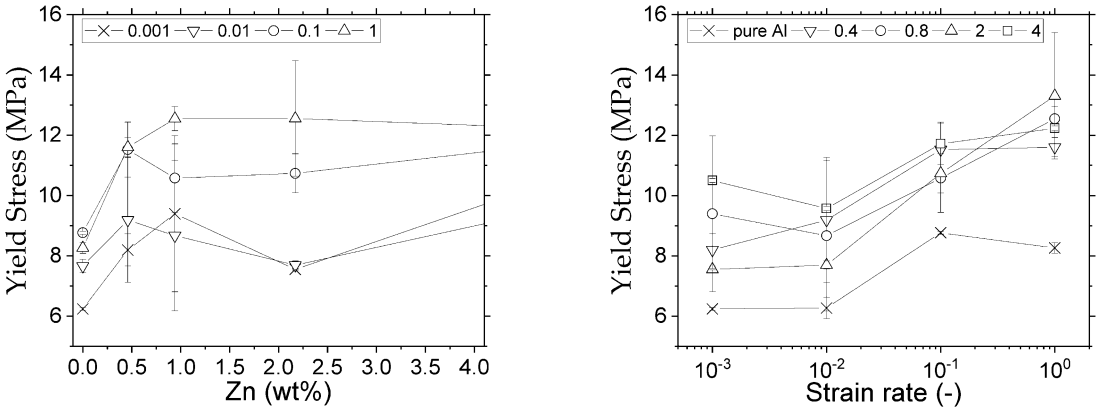

(a) **(b)**

Figure 6. Yield stress as a function of (**a**) the concentration of Zn and (**b**) the true strain rate.

5. Simulation and discussion

5.1 Simulation input parameters

The general parameters, which are used in the models of section 2**,** are summarized in Table 4. The calibration parameters for the strengthening models are listed in Table 5, for pure Al as well as the Al-X (X = Mn, Cu, Zn) alloys. The input parameters used for simulating the thermal stress contribution are marked with 'Th.', whereas the input parameters for the athermal stress contribution are marked with 'Ath.'. Since the strain rate and concentration dependence of the thermal stress contribution are given by the equations (1)-(5)., the respective parameters are constant in Table 5. For calibrating the dislocation density evolution, the so-called Kocks-Mecking (KM) plot, which shows the strain hardening rate as a function of stress, gives a good indication of the dislocation recovery behavior. Stronger recovery effects typically cause a steeper slope of the KM-plot and, therefore, affect the parameter B_{m} in Table 5, for instance. Since dynamic recovery is not dependent on the concentration in the investigated Al-Mn alloys, B_{m} and B_{im} are constants. The parameters C_{m}, C_{im} and C_{w} take dislocation climbing into account and can be treated as constant for the deformation tests at room temperature. It should be noted that this approach does not claim to be a comprehensive representation of all occurring physical mechanisms, but it represents a consistent way to describe the dislocation density evolution and successfully simulate a variety of flow curves with a single set of parameters.

Table 4. General input parameters for the strengthening models as described in sections 2.1 -2.2.

Symbol	Meaning	Unit	Value	Source
b	Burgers vector	m	$2.86 \cdot 10^{-10}$	[55]
G	Shear modulus	MPa	29,438.4–15.052T	[36]
ν	Poisson's ratio	-	0.347	[56]
M	Taylor factor	-	3.06	[57]

Table 5. Input parameters for the strengthening models as described in sections 2.1 and 2.2. The input parameters used for simulating the thermal stress contribution are marked with 'Th.', whereas the input parameters for the athermal stress contribution are marked with 'Ath.'.

		Pure Al	Mn	Cu	Zn	Equ.
σ_{basic}	Th.	18 MPa				(1)
k_1		0.1				(2)
k_2		0	0.55	0.8	0.3	(2)
n		1/3				(2)
n_{ss}		1.8				(3)
ε_{m}		0	0.042	0.0194	0.0038	(5)
A_{m}	Ath.	$-0.22 \cdot \ln(\dot{\varepsilon}) + 33.75$				(8)
β_{ss}		0	$202.17 \cdot c^{1.80}$	$2.62 \cdot \dot{\varepsilon}^{-0.064} c$	$0.0046 \cdot c^{0.11}$	(8)
β_{w}		750				(8)
β_{G}		0.08				(8)
A_{w}		$-0.07 \cdot \ln(\dot{\varepsilon}) + 0.68$				(10)
A_{im}		$-(1.3 \cdot 10^{-4}) \cdot \ln(\dot{\varepsilon}) + 0.85$				(11)
B_{m}		$-0.564 \cdot \ln(\dot{\varepsilon}) + 8.94$	$B_{\mathrm{m,Al}}$	$B_{\mathrm{m,Al}} - 27.2 \cdot \dot{\varepsilon}^{-0.14} c^{0.52}$	$B_{\mathrm{m,Al}} - 0.78 \cdot \dot{\varepsilon}^{-0.3} \cdot c^{0.24}$	(9)
B_{im}		$0.03 \cdot \ln(\dot{\varepsilon}) + 0.9$	$B_{\mathrm{im,Al}}$	$B_{\mathrm{im,Al}}$	$B_{\mathrm{im,Al}}$	(16)
C_{m}		0.2				(12)
C_{im}		0.2				(15)
C_{w}		0.2				(18)

5.2 Dislocation density evolution in pure Al and in Al-Cu

Figure 7 shows the calculated evolution of the mobile dislocation density, ρ_{m}, the wall dislocation density, ρ_{w}, the immobile dislocation density, ρ_{im} and a weighted sum, ρ_{tot}, during deformation at RT with a true strain rate of 0.001 s^{-1} for (a) pure Al and (b) binary Al-Cu (1.6 wt%). The simulated dislocation density ρ_{tot} agrees reasonable with the obtained dislocation densities from [58], which are also included in Figure 7 (a). In the early stages of deformation,

the total dislocation density is mainly controlled by the generation of mobile dislocations. With increasing mobile dislocation density, the transformation into locks and dipoles gains relevance and, in addition to the mobile dislocation annihilation process, leads to a saturation of the mobile dislocation density. Only the formation and the annihilation of the mobile dislocations are directly affected by the alloying elements, as defined by β_{ss} and B_{m} in Table 5. With an increasing amount of Cu, more mobile dislocations are generated, leading to a higher saturation level, as shown in Figure 7 (b). Since immobile and wall dislocations arise from mobile dislocations, these dislocation densities are indirectly concentration-dependent, as well.

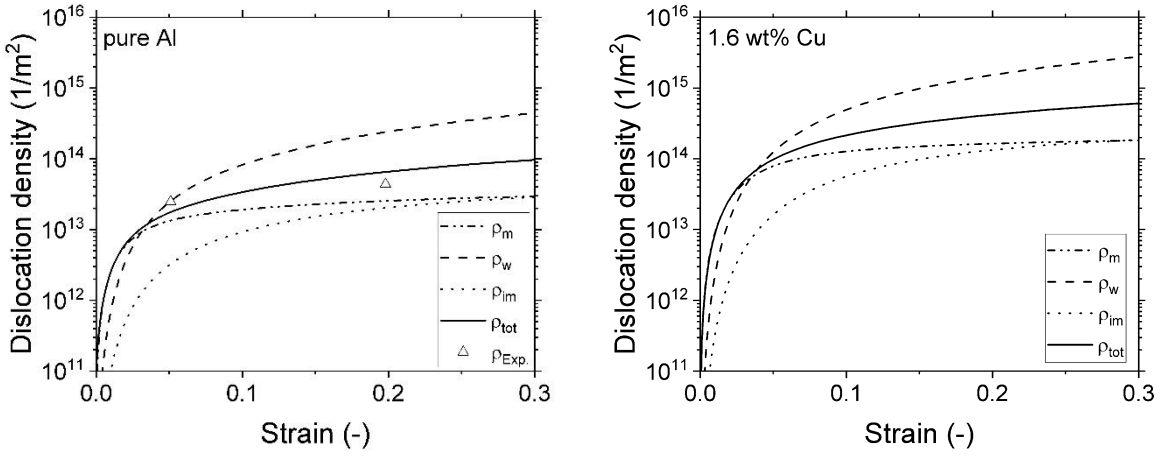

Figure 7. Calculated dislocation density evolution at RT and a strain rate of 0.001 s^{-1} for (**a**) pure Al and (**b**) Al-Cu (1.6 wt%).

The highest dislocation densities are predicted to occur inside the cell walls, with a maximum value of almost 10^{15} m^{-2} at 0.5 strain. Note that the total strain is the weighted sum of strain produced by internal and wall dislocations based on the cell volume fraction, f_w.

Although no direct experimental evidence has been provided to confirm the development of the different dislocation structures as shown in Figure 7, the measured flow curves provide valuable information about the dislocation development especially in pure Al, where work hardening is considered as the main strengthening mechanism.

5.3 Flow curve simulations

In Figure 8, flow curves of different binary Al-Mn alloys are plotted for strain rates between 0.001 s^{-1} and 1 s^{-1}. The solid lines represent the simulations, which are calculated on the basis of the simulation parameters listed in Table 4 and Table 5. The experimental results are indicated by the symbols. The plastic deformation behavior is given by the sum of the thermal and athermal stress contribution, as discussed in section 2. The thermal part determines the initial yield stress of each flow curve and is calculated by the superposition of the basic stress and solid solution strengthening. Due to thermal activation, the measured yield stress can be lower than the basic stress, as shown in equation (1). Especially for high strain rates ($\dot{\varphi}$ = 0.1 and $\dot{\varphi}$ = 1 s^{-1}) and high concentrations, a trend of increasing hardening rate θ can be observed in the experimental data.

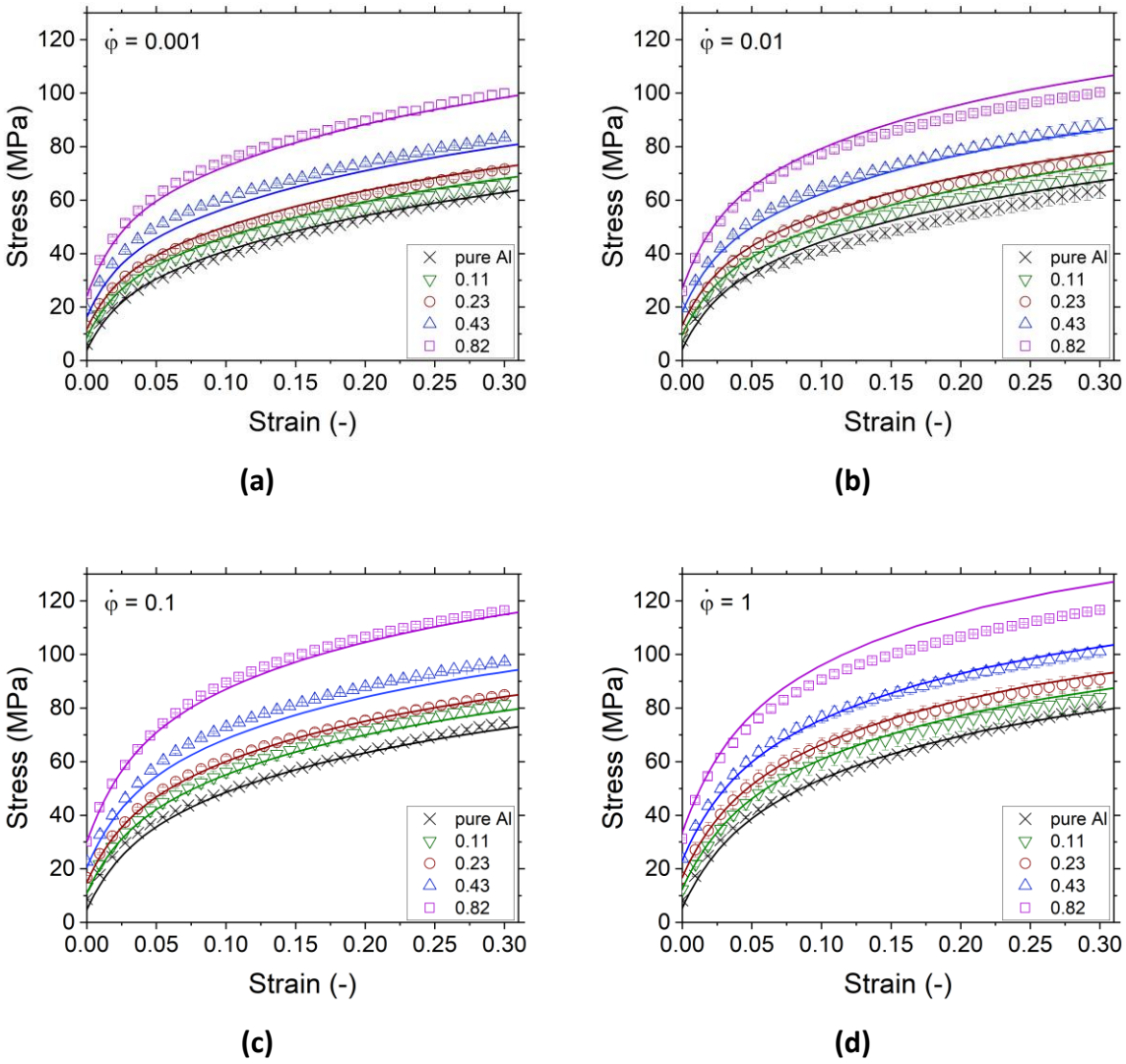

Figure 8. Flow curves of binary Al-Mn alloys at strain rates of **(a)** 0.001; **(b)** 0.01; **(c)** 0.1; **(d)** 1 s^{-1}.

Figure 9 shows the flow curves of the binary Al-Cu alloys for applied strain rates between 0.001 s^{-1} and 1 s^{-1}. The concentration-dependency of the work hardening rate is determined by the influence of the dissolved atoms on the internal and wall dislocation density, as discussed in section 2.2. An increasing Cu amount lowers the effective mean free travel distance of mobile dislocations and decreases B_{m}, as indicated by the equations in Table 5. Consequently, more mobile dislocations are formed, and less annihilation occurs at the same time, leading to a higher athermal stress contribution. The model calibration of β_{ss} and A_{m} suggest a negative strain rate sensitivity of the initial strengthening rate θ_0, as observed in the experiments. A slightly increasing dynamic recovery effect with increasing strain rate is given by the strain rate dependency of B_{m}. This can be observed if Figure 9 (a) and (d) are compared at 1.56 wt%

Cu. Although the flow curve has a higher initial yield stress at a strain rate of 1 s^{-1}, the evaluated stress at a strain of 0.3 is less compared to the curve at a strain rate of 0.001 s^{-1}.

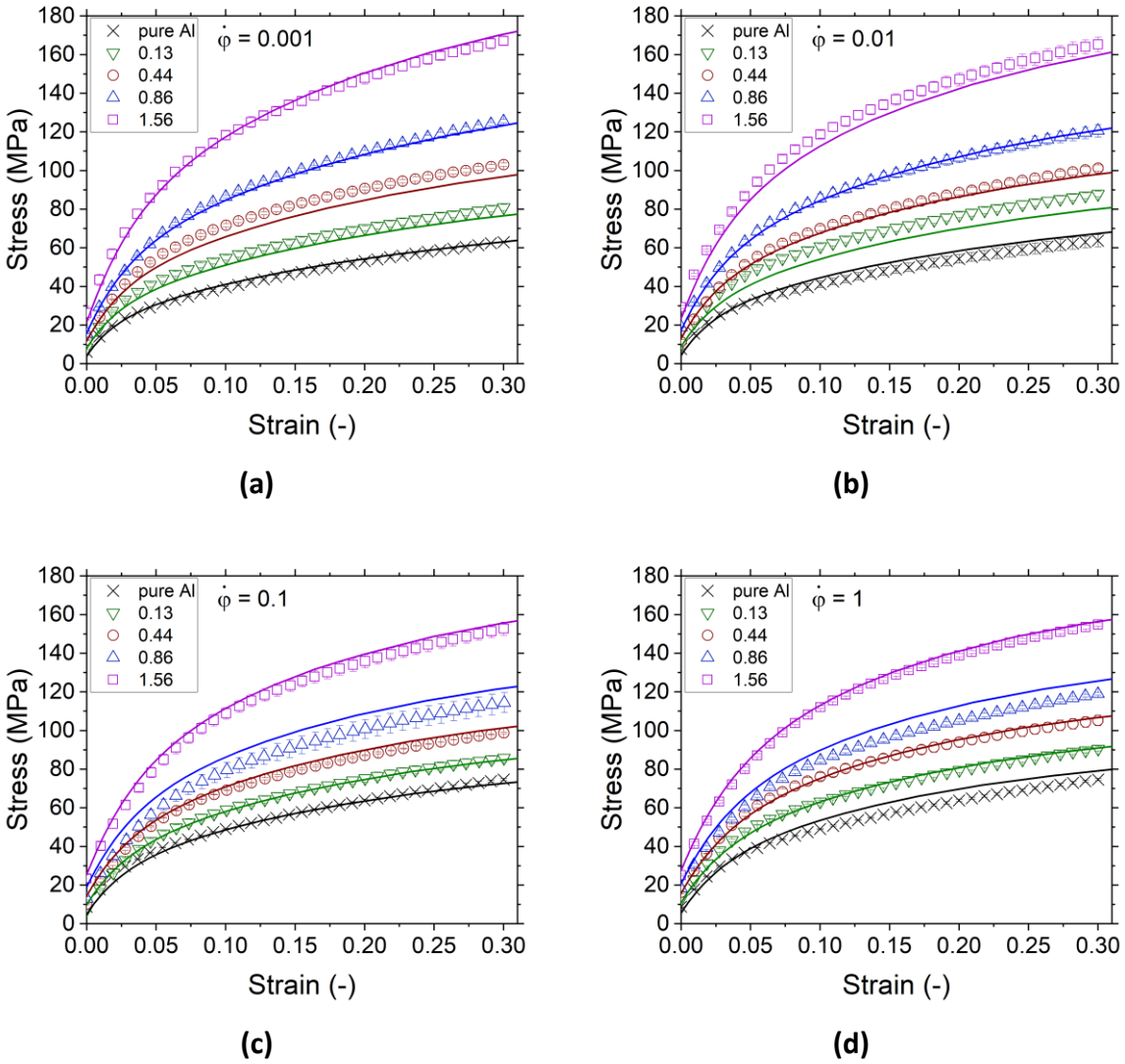

Figure 9. Flow curves of binary Al-Cu at strain rates of **(a)** 0.001, **(b)** 0.01; **(c)** 0.1; **(d)** 1 s^{-1}.

Figure 10 shows the flow curves of different binary Al-Zn alloys for strain rates between 0.001 s^{-1} and 1 s^{-1}. As discussed in section 4.3, the initial hardening rate rapidly increases, even at a small amount of dissolved Zn. However, the work hardening rate at higher strains seems to be almost independent of the Zn concentration, which is also seen in the simulation, represented by the solid lines in Figure 10. The yield stresses are almost independent of the Zn content, which is consistent with Figure 6 a.

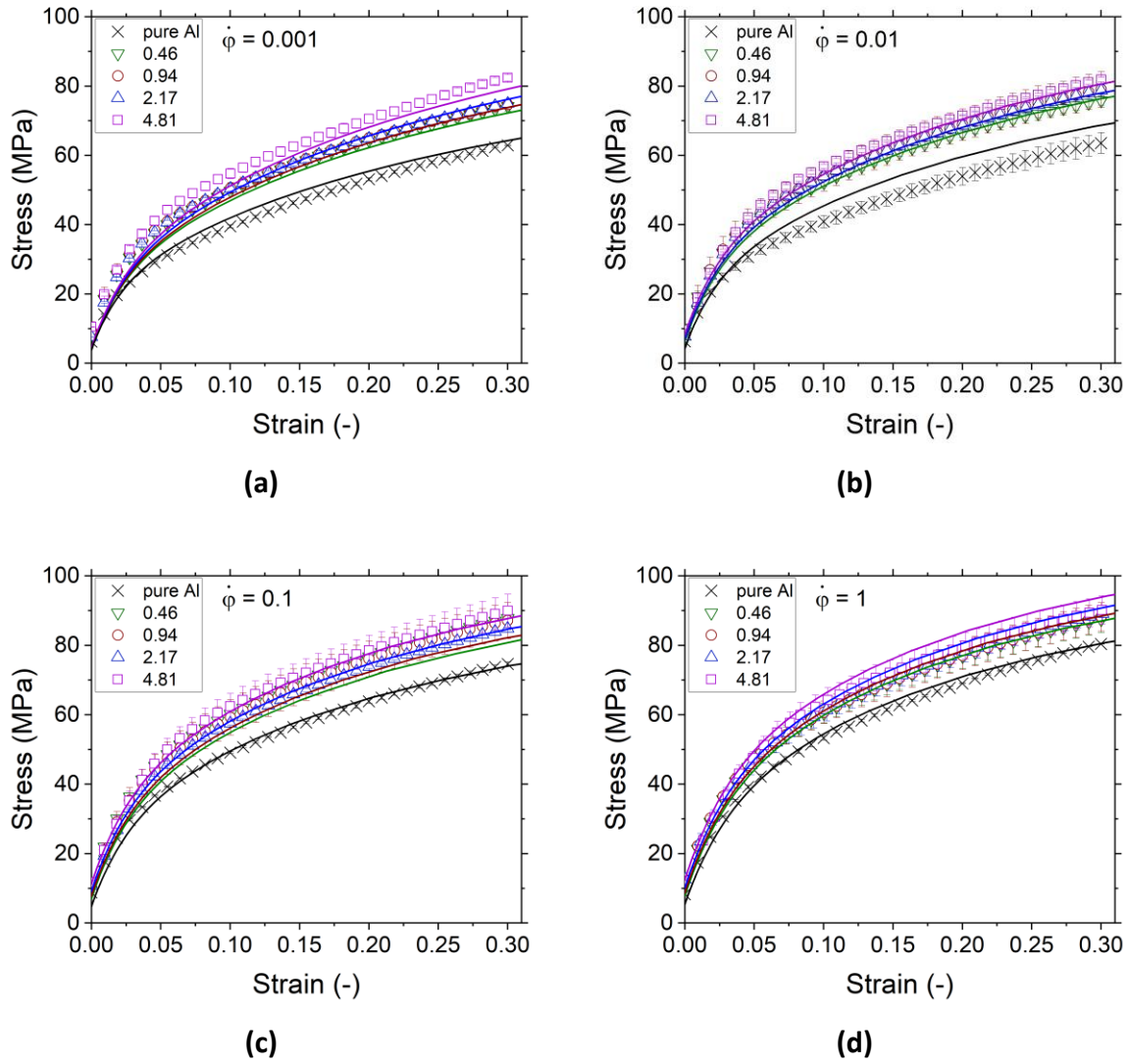

Figure 10. Flow curves of binary Al-Zn alloys at strain rates of **(a)** 0.001, **(b)** 0.01; **(c)** 0.1; **(d)** 1 s^{-1}.

6. Conclusion

In this work, a comprehensive experimental study of the influence of dissolved alloying elements on the yield strength as well as the work hardening is given. In addition, the evolution of mobile, immobile and wall dislocations is simulated. A better understanding of the strain rate- and concentration-dependent microstructure evolution can help to design novel Al-alloys. Therefore, binary Al-Cu, Al-Mn and Al-Zn alloys are cast, heat treated, extruded, and deformed. The main conclusions are:

- Higher concentration of Mn or Cu increases the yield stress, whereas Zn has only a low impact on solid solution strengthening. For calculating the yield stress, the mechanical threshold concept is used, where the activation energy depends on the effective concentration, c_{eff}, of the alloying elements.
- The strain rate dependency of the initial strain hardening rate θ_0 is opposite for Mn and Cu. A higher strain rate increases θ_0 in Mn-containing alloys, whereas a lowering effect is observed in Cu-containing alloys. This effect is accounted for in the calibration of the dislocation evolution model.
- Except for an increase in the initial work hardening rate, Zn has little influence on the strain-hardening effect.

For the flow curve simulations, an advanced 3IVM is used, which differentiates between mobile, immobile, and wall dislocations and also includes dynamic recovery terms for the immobile and wall dislocations. By using the Taylor equation, the dislocation densities are translated into stress contributions and flow curves are successfully simulated for different alloying concentrations and strain rates. All simulations are successfully performed on basis of a single set of composition-dependent input parameters.

Conflict of Interest Statement: On behalf of all authors, the corresponding author states that there is no conflict of interest.

CRediT Author Statement: Methodology, B.V.; software, B.V. and E.K.; investigation, B.V. and L.S.; writing—original draft preparation, B.V.; writing—review and editing, E.K.; visualization, B.V.; supervision, E.K.;

Acknowledgement: The authors are grateful to AMAG Austria Metall AG for the chemical analysis of the alloys. The authors acknowledge TU Wien Bibliothek for financial support through its Open Access Funding Program.

Appendix

List of symbols:

Symbol	Meaning
k_1	Calibration parameter for the low temperature activation energy
k_2	Calibration parameter for the low temperature activation energy
n	Calibration exponent for the low temperature activation energy
A_{m} β_{w} β_{G} β_{ss}	Calibration parameters, which consider the contributions of mobile dislocations (A_{m}), dislocation dipoles (β_{w}), the grain size (β_{G}), and the solutes (β_{ss}) to the mean free path.
B_{m} A_{im} A_{w}	Calibration parameters for dynamic recovery terms caused by dislocation annihilation (B_{m}), formation of dislocations locks (A_{im}) and dipoles (A_{w}).
C_{m} C_{im} C_{w}	Calibration parameters for static recovery of mobile dislocations (C_{m}), immobile dislocations (C_{im}) and wall dislocations (C_{w})

References

1. R. A. Labusch: *Phys. Stat. Sol.*, 1970, vol. 41, pp. 659–669.
2. G. P. M. Leyson, W. A. Curtin, L. G. Hector and C. F. Woodward: *Nat. Mater.*, 2010, vol. 9, pp. 750–755.
3. G. P. M. Leyson, L. G. Hector and W. A. Curtin: *Acta Mater.*, 2012, vol. 60, pp. 3873–3884.
4. G. P. M. Leyson and W. A. Curtin: *Scr. Mater.*, 2016, vol. 111, pp. 85–88.
5. A. Deschamps, Y. Bréchet, C. J. Necker, S. Saimoto and J. D. Embury: *Mater. Sci. Eng. A*, 1996, vol. 207, pp. 143–152.
6. A. H. Cottrell and M. A. Jaswon: *Proc. R. Soc. London*, 1949, vol. 199, pp. 104–144.
7. R. L. Fleischer: *Acta Metall.*, 1949, vol. 11, pp. 203–209.
8. H. Suzuki: *J. Phys. Soc. Japan*, 1962, vol. 17, pp. 322–325.
9. P. Haasen: *Mechanical Properties of Solid Solutions*. in *Physical Metallurgy III* (eds. R. W. Cahn and P. Haasen), pp. 2009–2073 (North-Holland, 1996).
10. N. F. Mott and F. R. N. Nabarro: *Physical Society Bristol Conference Report* (1948).
11. J. Friedel: *Les Dislocations.* (Gauthier-Villars, Paris, 1956).
12. G. P. M Leyson.and W. A. Curtin: *Philos. Mag.*, 2013, vol. 93, pp. 2428–2444.
13. M. Jobba, R. K. Mishra and M. Niewczas: *Int. J. Plast.*, 2015, vol. 65, pp. 43–60.
14. A. Kula, X. Jia, R.K. Mishra and M. Niewczas: *Int. J. Plast.*, 2022, vol. 155, 103321.
15. A. Hunter and D. L. Preston: *Int. J. Plast.*, 2022, vol. 151, 103178.
16. J. C. Teixeira, Y. Bréchet, Y. Estrin and C. Hutchinson: *Proc. 12th Int. Conf. Alum. Alloy.*, 2010, pp. 536–541.

17. N. Grilli, K. G. F. Janssens, J. Nellessen, S. Sandlöbes and D. Raabe: *Int. J. Plast.*, 2018, vol. 100, pp. 104–121.

18. E. Bitzek, C. Brandl, P. M. Derlet and H. Van Swygenhoven: *Phys. Rev. Lett.*, 2008, vol. 100, pp. 1–4.

19. U. Messerschmidt and M. Bartsch: *Mater. Chem. Phys.*, 2003, vol. 81, pp. 518–523.

20. F. Roters, D. Raabe and G. Gottstein: *Acta mater*, 2000, vol. 48, pp. 4181–4189.

21. M. Goerdeler: *Application of a Dislocation Density Based Flow Stress Model in the Integrative Through-Process Modelling of Aluminium Production.* (Shaker Verlag, 2007).

22. P. Ludwik: *Phys. Zeitschrift Nr.12*, 1909, pp. 411–417.

23. E. Voce: *Metallurgia*, 1955, pp. 219–226.

24. G. R. Johnson and W. H. Cook: *Proc. Seventh Int. Symp. Ballist.*, 1983, pp. 541–547.

25. F. J. Zerilli and R. W Armstrong: *J. Appl. Phys.*, 1987, vol. 61, pp. 1816–1825.

26. S. Huang and A.S. Khan, S. Huang, A. S. Khan: *Int. J. Plast.*, 1992, vol. 8, pp. 501–517.

27. U. F. Kocks: *J. Eng. Mater. Technol.*, 1976, vol. 98, pp. 76–85.

28. L. P. Kubin and Y. Estrin: *Acta Met. mater.*, 1990, vol. 38, pp. 697–708.

29. Y. Estrin: *J. Mater. Process. Technol.*, 1998, vol. 80, pp. 33–39.

30. E. Nes: *Prog. Mater. Sci.*, 1997, vol. 41, pp. 129–193.

31. F. Barlat, M. V. Glazov, J. C. Brem and D. J. Lege: *Int. J. Plast.*, 2002, vol. 18, pp. 919–939.

32. L. S. Tóth, A. Molinari and Y. Estrin: *J. Eng. Mater. Technol. Trans. ASME*, 2002, vol. 124, pp. 71–77.

33. R. A. Austin and D. L. Mcdowell: *Int. J. Plast.*, 2011, vol. 27, pp. 1–24.

34. X. G. Fan, and H. Yang: *Int. J. Plast.*, 2011, vol. 27, pp. 1833–1852.

35. C. Y Gao and L. C. Zhang: *Int. J. Plast.*, 2012, vol. 32–33, pp. 121–133.

36. E. I.Galindo-Nava, J. Sietsma and P. E. J. Rivera-Díaz-Del-Castillo: *Acta Mater.*,2012, vol. 60, pp. 2615–2624.

37. J. Kreyca and E. Kozeschnik: *Int. J. Plast.*, 2018, vol. 103, pp. 67–80.

38. W. A. Curtin, D. L. Olmsted and L. G. Hector: *Nat. Mater.*, 2006, vol. 5, pp. 875–880.

39. P. Haasen: *Mechanical properties of solid solutions* in *Physical Metallurgy*, pp. 2010–2073 (1996).

40. P. Sherstnev, P. Lang and E. Kozeschnik: *ECCOMAS 2012 - Eur. Congr. Comput. Methods Appl. Sci. Eng. E-b.,* 2012*,* pp*.* 5331–5338.

41. N. Hansen and X. Huang: *Acta Mater.,* 1998*,* vol*.* 46, pp. 1827–1836.

42. U. Kocks and H. Mecking: *Prog. Mater. Sci.,* 2003*,* vol 48, pp. 171–273.

43. F.F. Lavrentev: *Mater. Sci. Eng.,* 1980*,* vol. 46, pp. 191–208.

44. M. Sauzay and L. P. Kubin: *Progress in Materials Science,* 2011*,* vol. 56, pp. 725–784.

45. H. Mughrabi: *Curr. Opin. Solid State Mater. Sci.,* 2016*,* vol. 20, pp. 411–420.

46. D.R. Steinmetz, T. Jäpel, B. Wietbrock, P. Eisenlohr, I. Gutierrez-Urrutia, A. Saeed–Akbari, T. Hickel, F. Roters and D. Raabe: Acta Mater., 2013, vol. 61, pp. 494–510.

47. Y. Wang, H. Zhao, X. Chen, B. Gault, Y. Brechet, C. Hutchinson: *Acta Mater.,* 2024, vol. 265, 119643

48. A. Sadeghi and E. Kozeschnik: *Metall. Mater. Trans. A,* 2024, vol. 55, pp. 1643–1653.

49. F. D. Fischer, J. Svoboda, F. Appel and E. Kozeschnik: *Acta Mater.*, 2011, vol. 59, pp. 3463–3472.

50. R. Radis and E. Kozeschnik: *Model. Simul. Mater. Sci. Eng.*, 2012, vol. 20, pp. 1-15.

51. F. D. Fischer, J. Svoboda and E. Kozeschnik: *Model. Simul. Mater. Sci. Eng.*, 2013, vol. 21, pp. 1-13.

52. J. Kratochvil and S. Libovicky: *Pergamon Journals Ltd*, 1986, pp. 1625–1630.

53. W. B. Zhou, G.B. Teng, C.Y. Liu, H.Q. Qi, H.F. Huang, Y. Chen and H.J. Jiang, *l. J. Mater. Eng. Perform.*, 2017, vol. 26, pp. 3977–3982.

54. M. Somerday and F.J. Humphreys: *Mater. Sci. Technol.*, 2003, vol. 19, pp. 20–29.

55. H. J. Frost and M. F. Ashby: *Deformation-Mechanism Maps,* The Plasticity and Creep of Metals and Ceramics. (Pergamon Press, 1982).

56. J. P. Hirth and J. Lothe: *Theory of Dislocations.* (Krieger Publishing Company, 1991).

57. U. F. Kocks: *Metall. Mater. Trans.*, 1970, vol. 1, pp. 1121–1143.

58. J. Gubicza, N. Q. Chinh, Z. Horita and T. G. Langdon: *Mater. Sci. Eng. A*, 2004, vol. 387–389, pp. 55–59.

Conference Paper

Article

State Parameter-Based Simulation of Temperature- and Strain Rate Dependent Flow Curves of Al-Alloys

Bernhard Viernstein[a,1], Philipp Schumacher[b,2], Benjamin Milkereitb[c,3], Ernst Kozeschnik[a,4]

a Institute of Materials Science and Technology, TU Wien, Getreidemarkt 9, Vienna, 1060, Austria

b Chair of Materials Science, University of Rostock, Justus v. Liebig Weg 2, 18059 Rostock, Germany

c Competence Center for Calorimetry and Thermal Analysis Rostock - °CALOR, Department Life, Light and Matter, University of Rostock, Albert-Einstein-Str. 25, Rostock, 18059, Germany

1 bernhard.viernstein@tuwien.ac.at, 2 philipp.schumacher@mail.de, 3 benjamin.milkereit@uni-rostock.de,

4 ernst.kozeschnik@tuwien.ac.at

Abstract When simulating the material behavior during thermo-mechanical processes, the understanding of the microstructure evolution is fundamental. Therefore, state parameter-based models are utilized to describe physical effects such as work hardening, precipitation hardening, solid solution hardening and cross core diffusion. Using the thermo-kinetic software package MatCalc, temperature- and strain rate dependent flow curves of compression tests are successfully simulated. The theoretical background of the underlying physical models and the influence of alloying elements on the cross core diffusion behavior are discussed. Various Al-alloys are investigated and the experimentally obtained flow curves are evaluated in terms of initial strain hardening rate, initial yield stress and saturation stress. In Al-alloys, especially the effect of Mg is dominant due to its ability to diffuse from the compression side to the tension side of the dislocations core, leading to additional barriers for the dislocation movement.

Keywords Flow curve, Strengthening mechanisms, Solutes, Small strains

1. Introduction

Many state parameter based yield strength models capture the influence of temperature- and strain rate behavior on plastic deformation of polycrystalline materials [1-12]. Mobile dislocations interact with obstacles, leading to work hardening, precipitation strengthening, or solid solution hardening, which are strongly dependent on the current microstructure. Grain boundary hardening is out of the scope of the present work. The thermo-kinetic software package MatCalc is used to simulate flow curves of different binary Al-Mg alloys. This work focuses on the influence of temperature, strain rate and solute concentration on the initial yield strength. Generally, flow curves, which represent material properties, can be used as input data in FE-simulations for calculating internal stresses. Therefore, the transition from the linear elastic deformation to plastic deformation needs to be calculated properly. The existing model, which is implemented in MatCalc, is adapted by a correction term, due to the difficulty of reproducing the initial stress-strain slopes θ_0 and the saturation stresses σ_{sat} starting from Rp0.2 in experimental results. The modified model significantly improves the agreement of simulations and experimental results of different flow curves.

2. State of the art

2.1 Thermal activation at constant microstructure

The strength and density of obstacles determine the dislocation motion rate $\dot{\varepsilon}$, represented by an Arrhenius equation [13-18], as

$$\dot{\varepsilon} = \dot{\varepsilon}_0 \cdot \exp\left(\frac{-\Delta G}{kT}\right). \tag{1}$$

$\dot{\varepsilon}_0$ is a constant and ΔG is the free activation enthalpy. An assumed box-shaped energy barrier leads to [15, 19]

$$\Delta G(\sigma) = \Delta F[1 - \left(\frac{\sigma}{\hat{\tau}}\right)], \tag{2}$$

where ΔF is the total free energy to overcome the obstacle barrier, σ is the applied shear stress and $\hat{\tau}$ is the mechanical threshold, which is the required stress for ongoing dislocation movement without thermal activation at 0 K. The activation energy ΔF depends on the

obstacle strength and is expressed as a function of the effective concentration of solutes within the matrix [19]. Additional microstructural dependence of ΔF, for instance on precipitates, will be the scope of further investigations. However, $\hat{\tau}$ is related to the material state and strongly depends on the thermo-mechanical history of the material. The mechanical threshold combines strengthening mechanisms, such as, the cross core diffusion effect, solid solution hardening, precipitation hardening and grain size hardening. Combining Eq. (1) and Eq. (2) leads to

$$\sigma = \hat{\tau} \cdot \left(1 - \left[\frac{kT}{\Delta F}\right] \ln\left(\frac{\dot{\varepsilon}}{\dot{\varepsilon}_0}\right)\right). \tag{3}$$

Since Eq. (3) becomes invalid at a critical temperature Tcrit, the following alternative equation is widely used in literature [19, 20]:

$$\sigma_{\mathrm{lt}} = \hat{\tau} \cdot exp\left(\frac{-kT}{\Delta F_{\sigma 0}^{\mathrm{lt}}} * ln\left(\frac{\dot{\varepsilon}_0}{\dot{\varepsilon}}\right)\right). \tag{4}$$

At elevated temperatures, dislocation climb becomes the dominant mechanism, leading to an increasing resolved strain rate dependence of stress, which is expressed by the following power-law equation [15]

$$\dot{\gamma} \propto \left(\frac{\sigma}{\mu}\right)^n. \tag{5}$$

The exponent n varies between 3 and 10 [15]. In the following, yield stress at high temperatures is calculated according to [19]

$$\sigma_{\mathrm{ht}} = \left(\hat{\tau} \frac{\dot{\varepsilon} k T (\alpha b G)^2}{2bc\Delta F_{\sigma 0}^{\mathrm{lt}} \cdot exp\left(-\frac{\Delta F_{\sigma 0}^{\mathrm{lt}}}{kT}\right)}\right)^{1/n}. \tag{6}$$

α is the strengthening coefficient, b the Burgers vector, G the shear modulus, and c the speed of sound.

The total thermal stress σ_0 is then given as

$$\sigma_0 = \left(\frac{1}{\sigma_{\mathrm{lt}}} + \frac{1}{\sigma_{\mathrm{ht}}}\right)^{-1}. \tag{7}$$

2.2 Microstructure evolution

The Kocks-Mecking model is a state-parameter based representation of the microstructure evolution during a thermo-mechanical treatment and is expressed as [13, 21]

$$\frac{\partial \rho}{\partial \varepsilon} = \frac{d\rho^+}{d\varepsilon} + \frac{d\rho^-}{d\varepsilon} = \frac{M}{bA}\sqrt{\rho} - 2BM\frac{d_{\mathrm{crit}}}{b}\rho. \quad (8)$$

The first term $\frac{d\rho^+}{d\varepsilon}$ refers to the generation of dislocations, while $\frac{d\rho^-}{d\varepsilon}$ takes the annihilation of dislocations during plastic deformation into account. M is the Taylor factor, A and B are proportionality constants and d_{crit} is the critical annihilation distance between two dislocations [22]. At high temperatures, vacancy-assisted climb becomes dominant and is incorporated by the following term, which represents static recovery

$$\frac{d\rho_s^-}{d\varepsilon} = -2CD_d\frac{Gb^3}{\dot{\varepsilon}kT}\left(\rho^2 - \rho_{\mathrm{eq}}^2\right). \quad (9)$$

C is a constant, $D_{\mathrm{d}}\ is$ the diffusion coefficient along dislocation pipes, $\dot{\varepsilon}$ the strain rate and ρ_{eq} is the equilibrium dislocation density. The Taylor equation correlates the present material state with the athermal plastic stress contribution σ_{p} as

$$\sigma_{\mathrm{p}} = g_1\sqrt{\rho}\,, \quad (10)$$

with $g_1 = \alpha MbG$.

Recently, Kreyca [19] established a relation between A$(\dot{\varepsilon}, T)$, B$(\dot{\varepsilon}, T)$ and C$(\dot{\varepsilon}, T)$ to the initial slope θ_0 and the saturation stress σ_{sat} of a stress-strain curve by

$$A = \frac{g_1 M}{2b\theta_0}, \quad (11)$$

$$B = \frac{b\theta_0}{\sigma_\infty^{\mathrm{lt}} d_{\mathrm{crit}} M}, \quad (12)$$

$$C = \frac{g_1^2}{(\sigma_\infty^{\mathrm{ht}})^3}\frac{\theta_0 \dot{\varepsilon} kT}{D_{\mathrm{d}} G b^3}. \quad (13)$$

The saturation stress σ_{sat} is reached, when dislocation generation is balanced by dislocation annihilation. Similar to Eq. (4) and Eq. (6), a distinction of the saturation stress at two temperature regimes is introduced to consider both, thermally activated glide at low temperature as well as vacancy-assisted climb at high temperature. For detailed explanation of θ_0, $\sigma_\infty^{\mathrm{lt}}$ and $\sigma_\infty^{\mathrm{ht}}$, see [19, 20].

3. Small strain correction of the flow curve

By evaluating experimental data, the applied model leads to a satisfying agreement starting at a defined yield stress at a strain of 2 %, labelled as Rp2. A limitation of the described models (see 2.1 and 2.2) is that the steeper slope of the stress-strain curve at lower strain cannot be represented by the extended Kocks-Mecking model, which has been designed to represent

stage III hardening [21]. The experimental observations can be explained by inhomogeneities of the material, leading to varying plasticity behavior than described by the extended Kocks-Mecking model. However, for calculating internal stresses in further applications, the transition between the linear elastic range and the plastic range needs to be calculated properly. Therefore, an interpolation function is established and introduced in the schematic Fig. 1. In the first step, the applied model (see 2.1 and 2.2) is calibrated according to experimental results, in order to simulate the flow curves, starting at Rp2 (point 1). In the second step, the same set of calibration parameters is used to simulate the flow curve from Rp0.2 (point 2). This can be illustrated as a shift of the calculated stress strain curve in step one to Rp0.2 (point 2), indicated by the black arrow in Fig 1. Consequently, this simulated flow curve does not fit to the experimental results, until a correction function ("ß-function") lowers the anterior part to point 3 in step three. As a result, the corrected final flow curve is calculated, starting from Rp0.2 (point 3).

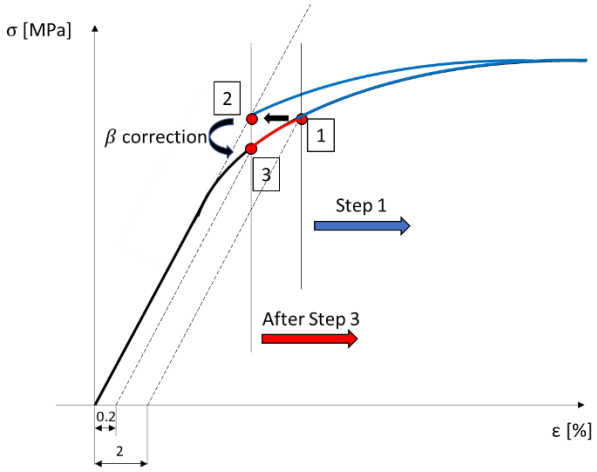

Figure 1. Schematic explanation of the correction function at small strains. Stress-strain curves are calculated from R_{p2} (point 1), shifted to $R_{p0.2}$ (point 2) and lowered to point 3.

The correction function is defined as

$$\sigma_{\beta-\text{function}} = \sigma_{\text{model}} \cdot \beta, \tag{14}$$

where σ_{model} are the simulated stresses starting from Rp2 in point 2 in Fig. 1, which are equal to the stresses from Rp0.2 in point 3. β is defined as

$$\beta = \sqrt{\frac{\rho \cdot \beta_1}{\rho_{\text{sat}}}} + \beta_2, \tag{15}$$

where β_1 and β_2 are calibration parameters and ρ_{sat} is the saturation dislocation density. The resulting corrected function σ_{cor} is derived from the following summation rule:

$$\left(\frac{1}{\sigma_{\mathrm{cor}}}\right)^{n} = \left(\frac{1}{\sigma_{\mathrm{model}}}\right)^{n} + \left(\frac{1}{\sigma_{\beta-\mathrm{function}}}\right)^{n}, \tag{16}$$

where n is a calibration parameter. In Fig. 2, $\sigma_{\beta-\mathrm{function}}$ is shown as dotted line. Additionally, the shifted, uncorrected yield strength from Rp2 (dashed line), as well as the corrected final yield stress σ_{cor} (solid line) are displayed.

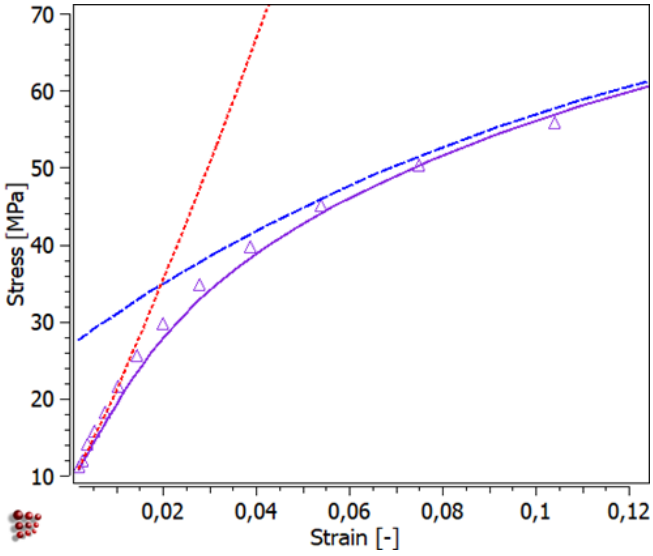

Figure 2. The blue dashed line represents the uncorrected flow curve from Rp2, which is shifted to a strain of $\varepsilon = 0.002\ [-]$; the red dotted line is the β-function and the purple solid line is the simulation of the corrected final flow curve starting from Rp0.2 (σ_{cor}). Symbols indicate experimental results of a deformation of pure Al at 30 °C at a strain rate of 0.1 s-1 [23].

Flow curves at low temperatures show high saturation dislocation densities ρ_{sat}, resulting in $\beta \approx \beta_2$. Using Eq. (16) leads to the final corrected stresses σ_{cor}. In case of low saturation stresses at high temperatures, β and $\sigma_{\beta-\mathrm{function}}$ become very high and according to Eq. (16), σ_{cor} are similar to the original, uncorrected stresses σ_{model}.

4. Influence of solutes on the initial yield stress σ_0 (Rp2)

The diffusion of solutes from the compression side to the tension side of a dislocation core leads to an additional barrier for dislocation movement and, consequently, to an additional strengthening effect [24]. Through the concentration change at the tension side, an effective concentration ceff is defined. The activation energies of the initial yield strengths (Rp2) $\Delta F_{\sigma 0}^{\mathrm{lt}}$ and $\Delta F_{\sigma 0}^{\mathrm{ht}}$ in Eq. (4) and Eq. (6) are fitted in dependence on ceff. The mechanism of the single-

atomic-hop motion is discussed in ref. [23] and is incorporated within the mechanical threshold framework, which is discussed in section 2.1. Improved diffusion at lower strain rates $\dot{\varepsilon}$ or higher temperatures leads to negative strain rate sensitivity (nSRS) within a certain strain rate and temperature range. Since ceff is temperature and strain rate dependent, the cross core diffusion effect and, as a consequence, the mechanical threshold stress (MTS) are dependent on temperature and strain rate as well. The combination of the MTS concept and the small strain correction function is validated on experimental data. This work compares pure Al4N (99.99 %) with two high purity binary Al-Mg alloys with 0.4 wt% and 0.8 wt% Mg in solid solution. It must be emphasized that small amounts of additional alloying elements in commercial alloys, such as Fe or Mn, strongly influence the resulting stress-strain curves, as investigated in [25]. The strain rate of the evaluated flow curves in this work is 0.1 s-1. Fig. 3 shows the uncorrected total yield stresses from Rp2 as a function of temperature and the nominal Mg concentration of the alloys. The higher the amount of Mg, the higher is the contribution of solid solution hardening. In the temperature range between approximately 100 °C and 300 °C, the temperature dependence of ceff becomes dominant, leading to an inflection point at the stress – temperature curve.

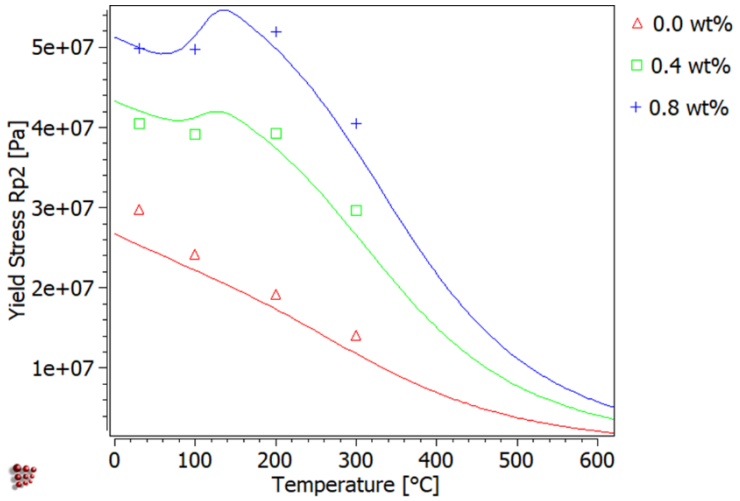

Figure 3. Comparison of simulated uncorrected yield stresses from Rp2 for different amount of Mg and experimental results (symbols) at a strain rate of 0.1 s^{-1}.

5. Final flow curve simulation

By calibrating θ_0, σ_∞^{lt} and σ_∞^{ht} (see [19]) with the experimental results, the coefficients A($\dot{\varepsilon}$,T), B($\dot{\varepsilon}$,T) and C($\dot{\varepsilon}$,T) are calculated by Eq. (11), Eq. (12) and Eq. (13). With the extended Kocks-Mecking model and the Taylor equation, the athermal stress contribution σ_p is calculated,

starting from Rp2. The uncorrected flow curve is given by the sum of thermal stress σ_0 in Eq. (7) and the athermal stress σ_p in Eq. (10). By fitting $\beta_1$and β_2 in Eq. (15), as well as the exponent n in Eq. (16), the correction function for small strains $\sigma_{\beta-\text{function}}$ is defined. Fig. 4 compares simulated final flow curves, starting from Rp0.2, for different amounts of Mg (0 wt% - 0.8 wt%) and different temperatures (30 °C, 100 °C, 200 °C, 300 °C).

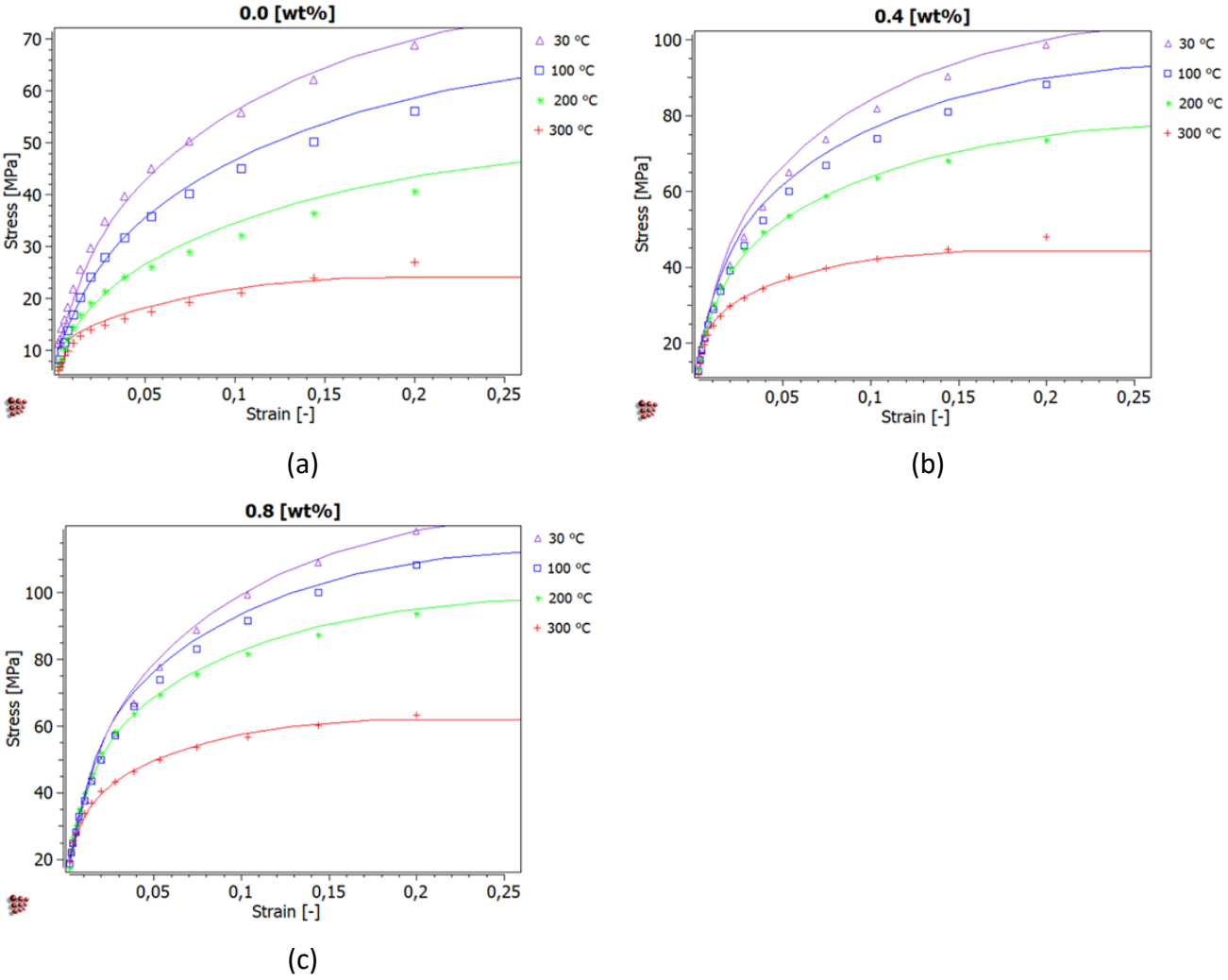

Figure 4. Comparison of simulation of the final flow curve from Rp0.2 and experimental results (symbols) for **(a)** 0.0 **(b)** 0.4 and **(c)** 0.8 wt. % Mg at a strain rate of 0.1 s-1

With the combination of the extended Kocks-Mecking model, the MTS framework and the introduced correction function, a good agreement between experiments and simulations, especially at small strains, is achieved. The investigation of the underlaying models for different strain rates and alloying elements is the scope for further simulations in the future.

6. Conclusions

The influence of solutes on the initial yield stress σ_0 (Rp2) is investigated in binary Al-Mg alloys at different temperatures. The results show a strong influence of the cross core diffusion effect in the temperature range between 100 °C and 300 °C. By adding the athermal stress contribution σ_{p}, the flow curve starting from Rp2 is calculated. Since stress-strain curves at lower strain cannot be represented satisfyingly with the applied models, a correction function is invented. The resulting corrected final flow curve, starting from Rp0.2, is in good agreement with experiments.

7. References

[1] L. P. Kubin and Y. Estrin, "Evolution of dislocation densities and the critical conditions for the Portevin-Le Chatelier effect," *Acta Met. mater.*, vol. 38, no. 5, pp. 697–708, 1990.

[2] E. Nes, "Modelling of work hardening and stress saturation in FCC metals," *Prog. Mater. Sci.*, vol. 41, no. 3, pp. 129–193, 1997.

[3] F. Roters, D. Raabe, and G. Gottstein, "Work hardening in heterogeneous alloys—a microstructural approach based on three internal state Variables," *Acta mater*, vol. 48, pp. 4181–4189, 2000.

[4] K. Marthinsen and E. Nes, "Modelling strain hardening and steady state deformation of Al – Mg alloys Modelling strain hardening and steady state deformation of Al – Mg alloys," *Mater. Sci. Technol.*, no. 17:4, pp. 376–388, 2001.

[5] F. Barlat, M. V Glazov, J. C. Brem, and D. J. Lege, "A simple model for dislocation behavior , strain and strain rate hardening evolution in deforming aluminum alloys," *Int. J. Plast.*, vol. 18, pp. 919–939, 2002.

[6] L. S. Tóth, A. Molinari, and Y. Estrin, "Strain Hardening at Large Strains as Predicted by Dislocation Based," *J. Eng. Mater. Technol.*, vol. 124, pp. 71–77, 2002.

[7] I. J. Beyerlein and C. N. Tome, "A dislocation-based constitutive law for pure Zr including temperature effects," *Int. J. Plast.*, vol. 24, pp. 867–895, 2008.

[8] R. A. Austin and D. L. Mcdowell, "A dislocation-based constitutive model for viscoplastic deformation of fcc metals at very high strain rates," *Int. J. Plast.*, vol. 27, no. 1, pp. 1–24, 2011.

[9] X. G. Fan and H. Yang, "Internal-state-variable based self-consistent constitutive modeling for hot working of two-phase titanium alloys coupling microstructure evolution," *Int. J. Plast.*, vol. 27, no. 11, pp. 1833–1852, 2011.

[10] C. Y. Gao and L. C. Zhang, “Constitutive modelling of plasticity of fcc metals under extremely high strain rates,” *Int. J. Plast.*, vol. 32–33, pp. 121–133, 2012.

[11] B. L. Hansen, I. J. Beyerlein, C. A. Bronkhorst, and E. K. Cerreta, “A dislocation-based multi-rate single crystal plasticity model,” *Int. J. Plast.*, vol. 44, pp. 129–146, 2013.

[12] D. Li, H. Zbib, X. Sun, and M. Khaleel, “Predicting plastic flow and irradiation hardening of iron single crystal with mechanism-based continuum dislocation dynamics,” *Int. J. Plast.*, vol. 52, pp. 3–17, 2014.

[13] U. F. Kocks, “Laws for work hardening and low temperature creep.pdf,” *J. Eng. Mater. Technol.*, vol. 98, no. 1, pp. 76–85, 1976.

[14] P. S. Follansbee and U. F. Kocks, “A constitutive description of the deformation of copper based on the use of the mechanical threshold stress as an internal state variable,” *Acta Met.*, vol. 36, no. I, pp. 81–93, 1988.

[15] H. J. Frost and M. F. Ashby, *Deformation-mechanism maps*. Oxford: Pergamon Press, 1982.

[16] G. Schoeck, “The Activation Energy of Dislocation Movement,” *Phys. Stat. Sol.*, vol. 8, pp. 499–507, 1965.

[17] A. S. Argon, “Mechanical properties of single- phase crystalline media: Deformation at low temperatures,” in *Physical Metallurgy III.*, Fourth, Re., Elsevier B.V., 1996, pp. 1877–1955.

[18] V. Schulze and O. Voehringer, “Influence of Alloying Elements on the Strain Rate and Temperature Dependence of the Flow Stress of Steels,” *Metall. Mater. Trans. A*, vol. 31, no. March, pp. 825–830, 2000.

[19] F. J. Kreyca, “State parameter based modelling of stress- strain curves in aluminium alloys,” Ph.D. thesis, TU Wien, 2017.

[20] J. Kreyca and E. Kozeschnik, “State parameter-based constitutive modelling of stress strain curves in Al-Mg solid solutions,” *Int. J. Plast.*, vol. 103, no. December 2017, pp. 67–80, 2018.

[21] U. Kocks and H. Mecking, “Physics and phenomenology of strainhardening: the FCC case,” *Prog. Mater. Sci.*, vol. 48, pp. 171–273, 2003.

[22] S. Brinckmann, R. Sivanesapillai, and A. Hartmaier, “On the formation of vacancies by edge dislocation dipole annihilation in fatigued copper,” *Int. J. Fatigue*, vol. 33, no. 10, pp. 1369–1375, 2011.

[23] P. Schumacher, “Plastisches Verformungsverhalten unterkühlter Aluminiumlegierungen im

System Al-Mg-Si," in *Band 7 von Forschungsberichte aus dem Lehrstuhl für Werkstofftechnik der Universität Rostock*, Shaker Verlag, 2018. doi:10.2370/9783844063851

[24] W. A. Curtin, D. L. Olmsted, and L. G. Hector, "A predictive mechanism for dynamic strain ageing in aluminium-magnesium alloys.," *Nat. Mater.*, vol. 5, no. November, pp. 875–880, 2006.

[25] Ø. Ryen and E. Nes, "Strengthening Mechanisms in Solid Solution Aluminum Alloys," *Metall. Mater. Trans. A*, vol. 37, 2006.